

**MICRO- AND MACROSCOPIC MODELLING
OF
BORON NEUTRON CAPTURE THERAPY**

thermal neutron facility design
phantom calculations
microdosimetry

Vroegindewey, Corine - Petten: Netherlands Energy Research Foundation
Ph.D. Thesis, Delft University of Technology.
ISBN 90-9010116-0
NUGI 743

Copyright ©1997 by C. Vroegindewey, ECN

All rights reserved. No part of this publication may be reproduced, stored
in a retrieval system, or transmitted in any form or by any means without
the prior written permission of the copyright owner.

**MICRO- AND MACROSCOPIC MODELLING
OF
BORON NEUTRON CAPTURE THERAPY**

thermal neutron facility design
phantom calculations
microdosimetry

PROEFSCHRIFT

ter verkrijging van de graad van doctor
aan de Technische Universiteit Delft,
op gezag van de Rector Magnificus Prof.dr.ir. J. Blaauwendraad
in het openbaar te verdedigen ten overstaan van een commissie,
door het College van Dekanen aangewezen,
op maandag 10 maart 1997 te 13:30 uur

door

Corine VROEGINDEWEIJ

geboren te Heukelum

Dit proefschrift is goedgekeurd door de promotoren:

Prof.dr.ir. A.J. Hermans

Prof.dr.ir. H. van Dam

Prof. Dr. D. Gabel

Samenstelling promotiecommissie:

Rector Magnificus, voorzitter

Prof.dr.ir. A.J. Hermans, Technische Universiteit Delft, promotor

Prof.dr.ir. H. van Dam, Technische Universiteit Delft, promotor

Prof. Dr. D. Gabel, Universität Bremen, promotor

Prof.dr. J.J. Broerse, Rijksuniversiteit Leiden

Prof.dr.ir. P.H.M. Lohman, Rijksuniversiteit Leiden

Prof. Dr. H. Mentzel, Université Louvain la Neuve

Dr. F.J. Wheeler, Idaho National Engineering Laboratory

The work described in this thesis was performed at the Netherlands Energy Research Foundation ECN, Petten.

Contents

General introduction	11
I Reactor calculations	15
1 Introduction to the reactor calculations	17
2 Design of the thermal neutron facility	21
2.1 Calculations to optimise the irradiation field	22
2.1.1 MCNP model	22
2.1.2 Response function	23
2.1.3 Optimisation of the graphite layer thickness	24
2.1.4 Optimisation of the position of the bismuth window	26
2.2 Construction of the thermal facility at the LFR	27
2.3 Verification of the calculations	30
2.4 Comparison with other thermal neutron sources	32
2.5 Conclusions about the thermal neutron facility	33
3 Generalised perturbation theory for reactor calculations	35
3.1 The Boltzmann transport equation	36
3.2 The adjoint transport equation	38
3.3 Perturbations of reactor geometry or composition	39
3.4 Response function	41
3.5 The DORT and SUSD computer-codes	43
3.6 Conclusions about the generalised perturbation theory	44

4	Conclusions about the reactor calculations	45
	References	49
	Nomenclature	53
II	Phantom calculations	55
5	Introduction to phantom irradiations	57
6	Calculations for a cylindrical phantom	61
6.1	Experimental situation	62
6.2	Description of the calculations	63
6.2.1	Beam characteristics	63
6.2.2	The DORT and MCNP model	63
6.3	Description of the methods of the measurements	65
6.4	Comparison of measured and calculated reaction rates	66
6.5	Comparison with ionisation chamber measurements	68
6.6	Comparison of calculated neutron spectra	71
6.7	Differences in computation time for the different codes and libraries	72
6.8	Sensitivity analysis	74
6.8.1	Effect of increasing the beam intensity above certain energy thresholds	74
6.8.2	Anisotropy of beam intensity	76
6.8.3	Boron in suspensions	78
7	Conclusions about the phantom calculations	81
	References	85
	Nomenclature	87
III	Microdosimetry	89
8	Introduction to the microdosimetry model	91

9	Structure of the microdosimetry model	95
9.1	Specific interactions of neutrons and photons in tissue	95
9.1.1	Capture reactions emitting charged particles	95
9.1.2	Photons	96
9.1.3	Proton Recoil	97
9.2	General description	97
10	The Monte Carlo model	101
10.1	The nuclear reactions	101
10.1.1	Geometry of the modelled cells	102
10.2	Biased Monte Carlo techniques	104
10.2.1	Location of interactions	104
10.2.2	Directions of the particles	105
10.3	Determination of energy deposition	105
10.4	Generation of stopping power tables	107
10.4.1	Comparison of available data sets for stopping power tables	107
10.4.2	The TRIM-88 code	108
10.4.3	Electric and nuclear stopping powers	108
10.4.4	Determination of the stopping power tables	108
10.5	Assumptions of the Monte Carlo program	109
11	Deterministic models	111
11.1	Dose distribution and number of tracks through the nucleus (D1) .	111
11.2	Energy imparted distributions (D2)	113
11.3	Determination of the effectiveness function (D3)	114
11.3.1	Single event model	116
11.3.2	Multiple event model	118
11.3.3	Weighted multiple event model	119
11.4	Calculation of the cell surviving fraction (D4)	120
11.5	Theoretical estimation of the RBE values (D5)	120
11.6	Determination of the boron concentration distributions (D6)	121
12	Analysis of a radiobiological experiment	123
12.1	Introduction and description of the experimental situation	123

12.1.1	Experimental situation	123
12.1.2	Neutron spectrum	124
12.1.3	Concentration distribution of the different atoms	124
12.2	Calculations made with the Monte Carlo program (MC)	125
12.3	Dose distribution and number of tracks (D1)	126
12.3.1	Number of particles through the nucleus	126
12.3.2	Mean track length in nucleus	129
12.3.3	Microscopic dose	132
12.3.4	Validation of the model with macroscopic dose	134
12.3.5	Calculated relative surviving fractions compared with measurements	135
12.4	Distributions of energy depositions (D2)	137
12.5	Determination of the effectiveness function (D3)	142
12.6	Surviving fractions (D4)	143
12.7	Calculations of the RBE values (D5)	147
12.7.1	Relative RBE values	147
12.7.2	Absolute RBE values	149
13	Sensitivity analysis for the radiobiological experiment	151
13.1	Introduction	151
13.2	Sensitivity analysis of the Monte Carlo calculations	152
13.3	Neutron energy spectrum	153
13.4	Influence of uncertainties in the photon dose	156
13.4.1	Uncertainties in the measured photon doses	156
13.4.2	Uncertainties in converting doses into surviving fractions	158
13.5	Determination of the effectiveness function	159
13.5.1	Other minimisation procedures	159
13.5.2	Weighting with uncertainties of measurements	161
13.5.3	Influence of the selection of a subset of concentrations or data points	163
13.6	Conclusions	164
14	Conclusions about the microdosimetry model	167
	References	173

Nomenclature	177
General conclusion and recommendations	179
Summary	185
Samenvatting	189
Acknowledgement	193
Curriculum Vitae	195

General introduction

The conventional treatment of cancer is comprised of three modalities: surgery, radiotherapy and chemotherapy (or a combination of these). Radiotherapy is very effective for a number of tumours, however, several tumours are resistant to standard radiotherapy. Several laboratories in Europe, USA, Asia and Australia are now working intensively on a radiotherapy, called Boron Neutron Capture Therapy (BNCT). With this bimodal therapy, each component has only minor effects on healthy cells if used separately. The first component is a stable isotope of boron (^{10}B) that when the right carrier is used can be concentrated in tumour cells. The second component is low-energy neutrons. BNCT is based on a nuclear reaction between these components. When a nucleus of ^{10}B captures a neutron, an unstable isotope, ^{11}B , is formed. The isotope ^{11}B instantly decays, yielding a lithium nucleus (^7Li) and an α -particle (a ^4He nucleus). These particles, which carry 2.79 MeV of energy, have a short range in tissue, of the order of about one cell diameter (around 10 μm) and cause closely spaced ionising events. These events can break the DNA-string thereby killing the malignant cell and stopping its proliferation.

The successful application of BNCT depends on several factors. Most important is the concentration of ^{10}B , which has to be high in the tumour and low in the healthy tissue, as well as the number and energy of the neutrons reaching the tumour. A limiting factor for these thermal neutrons is the damage they cause to healthy cells. Reactions will not only take place between boron and thermal neutrons, but also nitrogen and hydrogen atoms in healthy cells interact with neutrons and give reaction products. Although, the interaction probability (cross section) of these nuclei is small

compared with the boron reaction cross section, their concentration in cells is very high.

The $^{10}\text{B}(n,\alpha)$ capture reaction is a thermal reaction, which means that the interaction probability will be high for thermal neutrons and low for neutrons with higher energies; the reaction cross section is inversely proportional to the neutron velocity. As a consequence, in cases of superficial tumours a beam of thermal neutrons (energy less than 0.8 eV) is required to treat the tumour by BNCT. A problem arises when a tumour is situated deeper in the body. The number of thermal neutrons is rapidly attenuated as they diffuse through tissue. Therefore, it is difficult to get sufficient neutrons at the required depth in the body without delivering excessive radiation damage to surface tissues. To prevent this problem, beams of epithermal neutrons (energy between 0.8 eV and 0.1 MeV) are used to treat deep seated tumours. Epithermal neutrons lose energy as they penetrate the tissue and as they thermalised inside the body, are capable of reaching tumours at greater depths (in the order of centimetres). Adequate fluence rates of epithermal neutrons can presently only be provided with special facilities at nuclear reactors. The radiation field from a reactor core is a mixture of γ -rays, fast, epithermal, and thermal neutrons. To develop epithermal neutron beams special filters have to be used. In Petten an epithermal beam has been installed in the High Flux Reactor (HFR), with its prime goal to treat brain tumours.

The treatment procedure begins with the administration to the patient of a compound containing the boron atoms. The compound accumulates preferentially in malignant tissue compared with healthy tissue. The tumour is then irradiated with neutrons. The proposed clinical trials at Petten will be with glioblastoma multiforme, a type of brain cancer. The neutrons have to traverse a few centimetres of healthy tissue before reaching the tumour. The use of a thermal beam would be inefficient due to the high skin dose compared with the small number of thermal neutrons reaching the tumour at depth, and thus a small tumour dose. Therefore, epithermal neutron beams are developed. The epithermal neutrons will thermalise in the head, resulting in a tumour irradiation of principally thermal capture reactions.

In 1987 the Netherlands Energy Research Foundation (ECN) at Petten, embarked on the European collaboration in BNCT in order to broaden the field of application of the two research reactors at the Petten site. A number of projects have been set up to provide a better understanding of the principles of BNCT. One way to gain this understanding is based on radiobiological experiments. As such, a large part of this work has utilised thermal neutrons. Prior to the proposed work no thermal facility for radiobiological experiments was available outside the USA, Japan or Sweden. In the Netherlands, the first step was to design and develop a thermal neutron facility at one of the two available research reactors at Petten. The requirements for a thermal facility could not be met with the High Flux Reactor (HFR) without major (expensive) reconstruction work. Consequently, a thermal experimental facility at the Low Flux Reactor (LFR) in Petten was developed, adding a valuable supplement to the existing epithermal HFR-facility. The calculations in support of the development of this facility are described in the first part of this thesis.

In addition to the use of a thermal beam, radiobiological research was also performed using the epithermal beam at the HFR with the aid of so-called phantoms filled with water or tissue equivalent liquid to thermalise the neutrons. The process of thermalisation can be calculated using existing neutron transport codes. In the second step, calculations were performed for a phantom used frequently at Petten. In this phantom small vials with cell suspensions can be irradiated at different positions. By measuring the surviving fractions after irradiation in the epithermal beam, the effect of mixed field irradiations can be determined. In the third step of this project, a microdosimetric model has been developed and a detailed analysis of the experiments has been performed in order to provide the primary goal of this project, namely, a better understanding of the factors important to BNCT.

Although steps 1 and 2 of the project (described in parts I and II of this thesis) have proven to be useful and represent the state of the art in application, step 3 (described in part III of this report) represents unique research in this field. Classical radiotherapy relies on empirical factors (Relative Biological Effectiveness or RBE) that modify physical energy deposition in tissue to biological effect. The use of RBE is crude but effective in

conventional therapy where the radiation is of single form.

For BNCT, the RBE concept is inadequate as biological effects depend not only on the radiation particles but also on the energy distribution of the radiation and the microscopic distribution of the pharmaceutical compound. A mathematical approach is the only possible way to unravel the complex interactions present in BNCT. Experimental applications and the analytical work presented in this project may be considered as a significant start in this direction.

Part I

Reactor calculations

Chapter 1

Introduction to the reactor calculations

The Low Flux Reactor (LFR) of the Netherlands Energy Research Foundation (ECN) in Petten [Braak, 1987] is a small nuclear research reactor of the Argonaut type. The reactor that operates at a power up to 30 kW, consists basically of a ring-shaped core surrounded by an inner cylindrical graphite reflector and an outer graphite reflector. The core contains ten fuel elements arranged in two rows of 5 in an asymmetric configuration and cooled by light water. Figure 1.1 shows a horizontal cross section of the LFR.

An epithermal test facility for BNCT has been developed at a tangential horizontal beam channel on the northern side of the reactor. This facility has been used for the development of a neutron scintillation spectrometer [Crawford, 1993], for on-line γ -ray spectroscopy [Verbakel, 1995], and for dosimetry in phantoms [Konijnenberg, 1993]. On the irradiation trolley at the eastern side of the reactor, a facility using 1 MeV fission neutrons from a ^{235}U converter plate for reference radiobiological studies is available [Davids, 1969], [Huiskamp, 1983], [Sauwerwein, 1992]. On the western

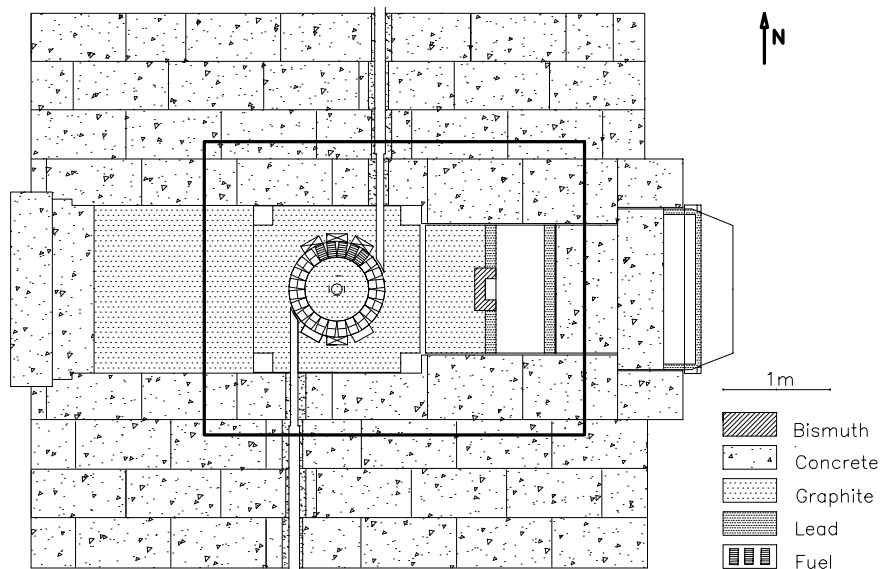


Figure 1.1: *Horizontal cross section of the reactor (at mid-height of the fuel). The thermal column is located on the west side of the reactor, the irradiation trolley on the east side.*

side of the graphite reflector a thermal column is located; in this column 15 horizontal channels are available. Finally, in the centre of the inner reflector of the reactor a vertical channel is available.

Due to the importance of a thermal test facility for the further development of BNCT, a decision was made to design a thermal facility at the LFR with a high intensity of thermal neutrons, whilst keeping the facility with low intensity of neutrons with higher energy and photons. Calculations and measurements have shown that the LFR in its standard configuration cannot produce an effective thermal beam for radiobiological experiments. Considering the possible locations, the irradiation trolley at the East side of the reactor was chosen as the most appropriate location for such a thermal beam facility. On the trolley, it is relatively easy to add materials, as opposed to other positions where major reconstructions of the reactor or the reactor hall would be necessary. A prerequisite for the facility on the irradiation

trolley is an easy replacement, since the irradiation trolley is also used for the biological irradiation facility for fast neutrons (> 1 MeV).

To obtain a thermal facility, the fast neutron and the γ -ray fluence rates behind the outer graphite reflector in front of the irradiation trolley must be reduced while maintaining an optimal thermal neutron fluence rate. This is achieved by adding moderating material and a gamma shield on the trolley. Based on the conclusions of an earlier feasibility study [Freudenreich, 1992], an optimisation study of the facility has been performed. The neutron and photon transport calculations were carried out using the Monte Carlo code MCNP [Briesmeister, 1993]. The optimisation of a biological response function was performed with respect to the dimensions of the additional moderator and of the position of the irradiation window within the shielding wall behind the moderator. After realising the facility, the calculated parameters were verified using neutron activation detectors (foils) [Paardekooper, 1994].

A modular extension of the outer graphite reflector has been chosen for the moderation of the neutrons. To study the influence of this choice, the effects on the neutron spectrum using different moderators have been considered within a global model of the reactor. To avoid a large amount of computational time, a technique was developed to obtain the effect on the irradiation position without explicitly recalculating the physical parameters for each new material. The technique, the so-called generalised perturbation theory, calculates the differences in a response function as a consequence of changes in the reactor lay out. This study is performed using the deterministic computer code DORT extended with extra routines for the perturbation theory [Vroegindeweyj, 1992a].

Chapter 2

Design of the thermal neutron facility

Based on an earlier performed study of a thermal facility at the LFR [Freudenreich, 1992] and on practical considerations, the thermal facility has been constructed from a graphite moderator with additional lead shielding [Vroegindewij, 1996a]. To maximise the thermal neutron fluence rate at the irradiation position, the lead shielding wall around the irradiation cubicle is replaced by a bismuth window. Bismuth has a lower absorption cross section than lead, leading to less capture photons, while being effective in shielding photons. In the optimisation two important parameters of the facility are considered: the thickness of the graphite moderator, and the position of the irradiation window in the gamma shield. All calculations and measurements reported refer to a reactor power of 30 kW.

2.1 Calculations to optimise the irradiation field

2.1.1 MCNP model

The calculations for the optimisation study have been performed with the Monte Carlo code MCNP-4A [Briesmeister, 1993]. In figure 1.1 the thick lines indicate the region that has been modelled in the computer code. Some regions inside this line have been not modelled in detail; for example beam-holes and irradiation channels have been neglected. In addition, to simplify the model, materials in some regions have been mixed. For example in the fuel region: fuel, graphite and water have been modelled as a homogeneous mixture. The calculations used fresh fuel only. A horizontal cross section of the MCNP model is presented in the figure 2.1.

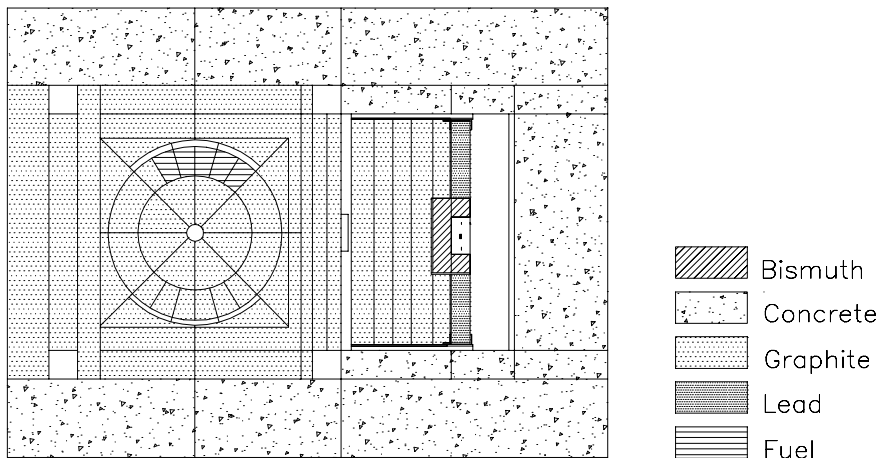


Figure 2.1: Horizontal cross section of the MCNP model

The coupled neutron-photon calculations with MCNP have been performed in the fixed source mode (for neutrons), while the spatial neutron source distribution has been taken from fluence rate measurements [Kraakman, 1982]. Photons from neutron captures have been generated according to the neutron field. Delayed photons (photons coming from the decay of fission products) are not taken into account in the coupled neutron-photon calculations of MCNP. An ENDF/B-V based cross section library [Briesmeister, 1993] is

used for the neutron and photon transport calculations.

The calculated neutron dose rates are based on the dose function for wet tissue given in ICRU-report 26 [ICRU, 1979]. The photon dose function has been taken from published data for water [Attics, 1986]. To account for the fact that different kinds of irradiation (for example neutrons with different energies or photons) cause different effects, the absorbed doses for the different types are multiplied by their specific RBE factor (Relative Biological Effectiveness), obtaining the equivalent dose. The RBE for photons is by definition equal to 1.

2.1.2 Response function

The thermal facility is optimised with respect to a biological response function for the two most important parameters of the facility: first by changing the thickness of the additional graphite moderator (see section 2.1.3) and second by determining the optimal position of the bismuth window in the lead wall (see section 2.1.4). For the optimisation, a $10 \times 10 \times 1 \text{ cm}^3$ tissue equivalent detector is defined inside the irradiation cubicle in order to simulate γ -rays from the capture of neutrons in biological targets as well. The calculated fluence and dose rates presented in the optimisation study are averaged over this detector volume.

The requirements for the radiobiological experiments impose two conditions:

1. the thermal neutron fluence rate should be sufficiently high to allow for realistic irradiation times;
2. the adverse dose rate from other beam components (epithermal neutrons, fast neutrons and γ -ray's) should be sufficiently low to minimise non-boron damage in the healthy tissue during irradiation.

From these conditions the following constraints result:

$$\begin{aligned} \text{thermal fluence rate:} & \quad \phi_{\text{th}} \geq 10^9 \text{ cm}^{-2}\text{s}^{-1}, \\ \text{dose rate from beam contamination:} & \quad \dot{D}_{\gamma} + \dot{D}_{\text{fast}} + \dot{D}_{\text{epi}} \leq 1.0 \text{ Gy/h}, \end{aligned}$$

where ϕ_{th} is the thermal fluence rate,
 \dot{D}_{γ} the γ -ray dose rate,
 \dot{D}_{fast} the fast neutron dose rate,
 \dot{D}_{epi} the epithermal neutron dose rate.

In the calculations, the following neutron energy groups have been employed:

thermal group:	energy lower than 0.5 eV
epithermal group:	energy between 0.5 eV and 1 MeV
fast group:	energy above 1 MeV.

The conditions lead to the definition of a response function R that should be maximised:

$$R(\text{RBE}) = \frac{\phi_{\text{th}}}{\dot{D}_{\gamma} + \text{RBE}_{\text{epi}} \cdot \dot{D}_{\text{epi}} + \text{RBE}_{\text{fast}} \cdot \dot{D}_{\text{fast}}}.$$

The reciprocal value of the response function represents the dose rate (in Gy/h) of γ -rays, epithermal and fast neutrons generated by a neutron field with unit thermal fluence rate ($1 \text{ cm}^{-2}\text{s}^{-1}$). The RBE values are not unambiguously determined, therefore in the following optimisation different values for the RBE have been used; however, for the sake of simplicity the RBE values for epithermal and fast neutrons have been assumed equal. In the optimisation, the dose rate from capture of thermal neutrons in nitrogen, the $^{14}\text{N}(\text{n,p})^{14}\text{C}$ reaction is neglected.

2.1.3 Optimisation of the graphite layer thickness

The optimal thickness of the graphite layer is obtained by calculating the response functions for five different thicknesses and by interpolation between these values. The maximum of the response function gives the optimal graphite thickness. In these calculations the vertical position of the bismuth window corresponds with the fuel centre-line. The window is shifted to the right of the lead wall (seen from the east side of the reactor towards the reactor core), because of the expected higher thermal fluence rate on

this side of the reactor. The centre of the window is situated 29 cm from the middle of the lead wall. The results of the calculations are given in tables 2.1 and 2.2.

Table 2.1: Thermal fluence rates and dose rates for different graphite thicknesses.

thickness [cm]	ϕ_{th} [$10^9 \text{ cm}^{-2} \text{ s}^{-1}$]	\dot{D}_{γ} [Gy h $^{-1}$]	\dot{D}_{fast} [Gy h $^{-1}$]	\dot{D}_{epi} [Gy h $^{-1}$]
29	3.8 ± 0.09	3.2 ± 0.4	2.0 ± 0.2	2.5 ± 0.2
39	2.3 ± 0.09	2.4 ± 0.5	1.0 ± 0.2	0.91 ± 0.10
48	1.6 ± 0.04	1.2 ± 0.2	0.25 ± 0.07	0.49 ± 0.13
54	1.3 ± 0.04	1.0 ± 0.2	0.27 ± 0.09	0.30 ± 0.06
59	0.99 ± 0.03	1.1 ± 0.2	0.16 ± 0.05	0.24 ± 0.04

Table 2.2: Response functions^a for different graphite thicknesses.

thickness	$R(\text{RBE}=1)$ [10^8]	$R(\text{RBE}=2)$ [10^8]	$R(\text{RBE}=3)$ [10^8]
29	4.9 ± 1.7	3.1 ± 1.2	2.3 ± 0.9
39	5.1 ± 1.7	3.6 ± 1.5	2.8 ± 1.2
48	7.9 ± 2.6	5.6 ± 2.5	4.3 ± 2.1
54	8.3 ± 2.5	6.1 ± 2.5	4.8 ± 2.3
59	6.9 ± 1.5	5.6 ± 1.7	4.6 ± 1.7

^a) Calculated values and the statistical uncertainties (one standard deviation)

As tables 2.1 and 2.2 indicate, the standard deviations connected to the outcome of the single calculations are rather large. However, for the purpose of the optimisation one is not interested in the absolute values of the

response function but only in the relative variation of the function with a changing graphite thickness. In the different MCNP calculations the same starting parameters are chosen for each simulated neutron. This means that the differences of the calculations are generated during the last part of the track of the individual particles as related to the different graphite thicknesses. Therefore, the results of the different MCNP calculations are strongly correlated. Due to this correlation, the differences found in the calculations are significant in spite of the large standard deviations (correlated sampling [Booth, 1985]). The optimal thickness of the graphite layer for this configuration amounts to about 54 cm.

2.1.4 Optimisation of the position of the bismuth window

The optimisation of the position of the bismuth filter has been performed for a graphite layer thickness of 54 cm. The vertical position of the window is still centred around the fuel centre-line, the horizontal position varies. The response functions are determined for ten different positions. In tables 2.3 and 2.4 the results of the calculations are given. In the first column the shift of the window to the right (seen from the east side of the reactor) is given with respect to the middle of the lead wall. The biological response function is calculated for three values of the RBE.

Tables 2.3 and 2.4 show that shifting the window from the right edge to the left, decreases the total dose rate slightly faster than the thermal fluence rate (keeping in mind that because of the correlated sampling the standard deviations can be assumed smaller when looking at the differences). Accounting for a conservative margin of the thermal fluence rate, the position is chosen equal to the centre position. The γ -ray dose rate for this position is equal to 0.9 ± 0.2 Gy/h. This value includes the component that originates from neutron capture γ -rays in the detector itself, which is considerable. The free beam γ -ray dose rate is about 0.5 Gy/h.

Table 2.3: Thermal fluence rates and dose rates^a for different horizontal positions of the bismuth window (positive numbers are positions to the right of the centre position)

position ^b [cm]	ϕ_{th} [$10^9 \text{ cm}^{-2}\text{s}^{-1}$]	\dot{D}_{γ} [Gy h ⁻¹]	\dot{D}_{fast} [Gy h ⁻¹]	\dot{D}_{epi} [Gy h ⁻¹]
-15	0.95 ± 0.03	0.6 ± 0.1	0.11 ± 0.04	0.11 ± 0.05
-10	1.07 ± 0.03	1.0 ± 0.2	0.07 ± 0.03	0.12 ± 0.04
-5	1.07 ± 0.03	1.0 ± 0.3	0.07 ± 0.02	0.16 ± 0.08
0	1.23 ± 0.04	0.9 ± 0.2	0.10 ± 0.03	0.19 ± 0.07
5	1.27 ± 0.04	0.9 ± 0.2	0.17 ± 0.05	0.13 ± 0.05
10	1.30 ± 0.04	1.6 ± 0.5	0.16 ± 0.04	0.21 ± 0.05
15	1.27 ± 0.04	0.9 ± 0.2	0.23 ± 0.06	0.25 ± 0.07
20	1.40 ± 0.04	1.2 ± 0.2	0.29 ± 0.07	0.25 ± 0.06
25	1.35 ± 0.04	1.1 ± 0.2	0.24 ± 0.06	0.27 ± 0.07
29	1.30 ± 0.04	1.0 ± 0.2	0.27 ± 0.06	0.30 ± 0.08

^a) Calculated values and the statistical uncertainties (one standard deviation)

^b) Numbers are distance in cm between centre of lead wall and centre of irradiation window

2.2 Construction of the thermal facility at the LFR

After the optimisation of the thickness of the graphite layer and the position of the bismuth window, a steel construction was added to the model. This construction is needed to give rigidity to the facility and to position the facility on the irradiation trolley. The thermal facility module has been constructed as a single module for easy installation and removal. Much effort has been put into the decrease of the γ -background: all structural elements on the trolley which can be reached by thermal neutrons are shielded by neutron absorbing materials with low energy capture γ -ray production, i.e. borated aluminium (boral) or borated plastics. Also the additional graphite layer was covered with boral plates on the outside, to prevent activation of the shielding materials (mainly concrete). Furthermore, the bismuth

Table 2.4: Response functions^a for different horizontal positions of the bismuth window (positive numbers are positions to the right of the centre position)

position ^b	$R(\text{RBE}=1)$ [10 ⁸]	$R(\text{RBE}=2)$ [10 ⁸]	$R(\text{RBE}=3)$ [10 ⁸]
-15	11.0 ± 2.0	8.5 ± 1.6	6.9 ± 1.3
-10	8.8 ± 1.8	7.4 ± 1.5	6.4 ± 1.3
-5	8.8 ± 1.8	7.4 ± 1.5	6.4 ± 1.3
0	10.3 ± 2.5	8.3 ± 1.0	6.9 ± 1.7
5	10.7 ± 3.1	8.6 ± 2.5	7.2 ± 2.3
10	6.6 ± 2.1	5.6 ± 1.7	4.8 ± 1.5
15	9.2 ± 2.1	6.8 ± 1.6	5.4 ± 1.3
20	8.0 ± 1.5	6.1 ± 1.1	5.0 ± 0.9
25	8.4 ± 1.6	6.4 ± 1.2	5.1 ± 1.0
29	8.3 ± 1.7	6.1 ± 1.3	4.8 ± 1.0

^a) Calculated values and the statistical uncertainties (one standard deviation)

^b) Numbers are distance in cm between centre of lead wall and centre of irradiation window

window was encapsulated in a 1.5 mm thick aluminium cladding to prevent polonium contamination which originates from the bismuth neutron capture reaction.

The as-built configuration of the thermal facility has been modelled with MCNP. For the new model, the thermal neutron fluence rate, the fast neutron dose rate, and the γ -ray dose rate distributions across the irradiation cubicle were calculated. At nine different positions, volume detectors were modelled: one in the middle of the cubicle detector, the other ones on a square around the middle. These positions are shown in figure 2.2. The detectors were placed at half depth of the cubicle (see figure 2.3). The calculated quantities at the positions of the nine detectors are given in table 2.5 (the left side of the matrix corresponds with the left side of the cubicle seen from the east side of the reactor towards the core).

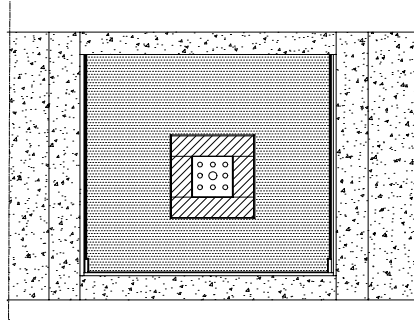


Figure 2.2: Vertical cross section of the MCNP-model. The detectors are modelled as small cylinders, shown as circles, in the figure.

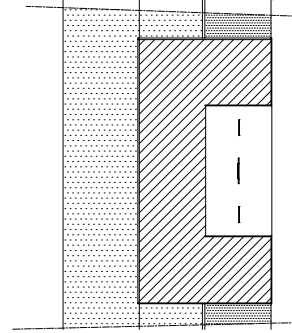


Figure 2.3: Cross section of the bismuth window. The lines in the bismuth window are the cross section through the small cylinders (detectors).

$\phi_{\text{th}} = 1.18 \pm 0.04$ $\dot{D}_{\text{fast}} = 0.10 \pm 0.02$ $\dot{D}_{\gamma} = 0.42 \pm 0.09$	$\phi_{\text{th}} = 1.20 \pm 0.04$ $\dot{D}_{\text{fast}} = 0.12 \pm 0.03$ $\dot{D}_{\gamma} = 0.56 \pm 0.14$	$\phi_{\text{th}} = 1.29 \pm 0.06$ $\dot{D}_{\text{fast}} = 0.10 \pm 0.02$ $\dot{D}_{\gamma} = 0.80 \pm 0.13$
$\phi_{\text{th}} = 1.13 \pm 0.05$ $\dot{D}_{\text{fast}} = 0.10 \pm 0.02$ $\dot{D}_{\gamma} = 0.50 \pm 0.10$	$\phi_{\text{th}} = 1.23 \pm 0.07$ $\dot{D}_{\text{fast}} = 0.16 \pm 0.03$ $\dot{D}_{\gamma} = 0.47 \pm 0.09$	$\phi_{\text{th}} = 1.33 \pm 0.04$ $\dot{D}_{\text{fast}} = 0.12 \pm 0.02$ $\dot{D}_{\gamma} = 0.56 \pm 0.10$
$\phi_{\text{th}} = 1.13 \pm 0.07$ $\dot{D}_{\text{fast}} = 0.10 \pm 0.02$ $\dot{D}_{\gamma} = 0.53 \pm 0.10$	$\phi_{\text{th}} = 1.06 \pm 0.04$ $\dot{D}_{\text{fast}} = 0.12 \pm 0.02$ $\dot{D}_{\gamma} = 0.68 \pm 0.13$	$\phi_{\text{th}} = 1.20 \pm 0.04$ $\dot{D}_{\text{fast}} = 0.16 \pm 0.03$ $\dot{D}_{\gamma} = 0.74 \pm 0.16$

Table 2.5: Thermal neutron fluence rate [$10^9 \text{ cm}^{-2} \text{ s}^{-1}$], fast neutron dose rate [Gy/h] and γ -ray dose rate [Gy/h] distribution over the irradiation cubicle.

The variation in the thermal fluence rates at the nine positions is relatively small. The thermal fluence rate falls off slightly from the right to the left

side of the cubicle (at most 15%). Also the fast neutron dose rate and the γ -ray dose rate vary over the irradiation cubicle. The mean fast neutron dose rate is equal to 0.12 Gy/h, and there is a tendency that the fast neutron dose rate decreases from the right lower edge to the left upper edge. The mean γ -ray dose rate is equal to 0.58 Gy/h. In the horizontal direction, the γ -ray dose rate decreases from the right to the left of the irradiation cubicle. In the vertical direction no significant trend is observed.

2.3 Verification of the calculations

In the constructed facility a series of neutron activation detectors (foils) [Schneider, 1973] was irradiated. These detectors are included in the computer model. The measured reaction rates [Paardekooper, 1994] for the reactions listed in table 2.8 are compared with the reaction rates as calculated by the MCNP-code. The positions are the same as in the calculations in the previous section. The composition and dimensions of the foils are given in table 2.6.

Table 2.6: Foil compositions and dimensions

foil	weight-%	diameter	thickness
Au	1% Au, 99% Al	12 mm	0.2 mm
Cu	100% Cu	12 mm	0.1 mm
Mn	88% Mn, 12% Ni	12 mm	0.1 mm
Ni	100% Ni	20 mm	1.0 mm

In the centre position (seen from reactor core), a foil set consisting of a AuAl, Cu, MnNi and Ni foil was positioned. Adjacent to this foil set, MnNi foils were placed at the centres of the squares around the middle of the window. The distance between the foils and the bismuth window is equal to 5 cm. In the MCNP model, the foils are surrounded by air, in reality the foils were placed on a polystyrene block (95% air) which was

fitted into the bismuth window. The AuAl, Cu and MnNi foils are activated mainly by thermal neutrons [Zijp, 1984]: for the AuAl foil about 5%-10% of the activation comes from epithermal neutron captures; for the other two foils, this contribution is only 1%. The Ni foil monitors the fast neutron fluence rate. Choosing the above mentioned foils and positions, comparison of the measured and calculated foil activations gives an indication of the accurateness of the calculated thermal fluence rate distribution over the irradiation cubicle and the calculated neutron spectrum in the centre of the irradiation cubicle (which are directly connected to the neutron dose rates).

Table 2.7: Measured (M) and calculated^a (C) Mn reaction rate [$10^{-14} s^{-1}$] at the nine positions

M = 1.13 ± 0.03 C = 1.36 ± 0.09 D ^b = 20%	M = 1.20 ± 0.04 C = 1.43 ± 0.08 D = 19%	M = 1.26 ± 0.04 C = 1.53 ± 0.08 D = 21%
M = 1.15 ± 0.03 C = 1.40 ± 0.11 D = 22%	M = 1.27 ± 0.04 C = 1.52 ± 0.10 D = 20%	M = 1.27 ± 0.04 C = 1.39 ± 0.08 D = 9%
M = 1.09 ± 0.03 C = 1.25 ± 0.11 D = 15%	M = 1.18 ± 0.04 C = 1.33 ± 0.14 D = 13%	M = 1.24 ± 0.04 C = 1.50 ± 0.10 D = 21%

^a) Calculated values and the statistical uncertainties (one standard deviation)

^b) D = rel. difference = $\frac{\text{calculated-measured}}{\text{measured}} \cdot 100\%$

The calculated and measured reaction rates for the $^{55}\text{Mn}(n,\gamma)$ reaction are given in table 2.7. Comparing the calculations with the measurements, it must be taken into account that there are different sources of uncertainties. The relatively low power of the reactor makes it complicated to determine the absolute power level by a thermal balance. Uncertainties in the cross section library and assumptions concerning the geometry of the reactor introduce additional uncertainties in the calculations. For all nine MnNi

Table 2.8: Reaction rates [s^{-1}] of the central foil set

reaction	measured	calculated	rel. diff.
$^{197}\text{Au}(n,\gamma)^{198}\text{Au}$	$(1.02 \pm 0.02) \cdot 10^{-13}$	$(1.12 \pm 0.05) \cdot 10^{-13}$	9%
$^{63}\text{Cu}(n,\gamma)^{64}\text{Cu}$	$(4.05 \pm 0.12) \cdot 10^{-15}$	$(5.38 \pm 0.41) \cdot 10^{-15}$	25%
$^{55}\text{Mn}(n,\gamma)^{56}\text{Mn}$	$(1.27 \pm 0.04) \cdot 10^{-14}$	$(1.52 \pm 0.08) \cdot 10^{-14}$	15%
$^{58}\text{Ni}(n,p)^{58}\text{Co}$	$(2.00 \pm 0.10) \cdot 10^{-19}$	$(2.03 \pm 0.28) \cdot 10^{-19}$	1%

foils, the calculated manganese reaction rates are higher than the measured manganese reaction rates, the maximum relative difference equals 18%. The results for the foil set, located in the middle of the cubicle are given in table 2.8. The calculated reaction rates are again higher than the measured ones, the maximum difference is equal to 25%. Noting the uncertainties in the calculations and measurements, these relative differences are very reasonable at least and all lie within 3 standard deviations.

2.4 Comparison with other thermal neutron sources

The thermal facility of the LFR has been compared with the thermal neutron beams of three other reactors used for BNCT: the 3 MW Brookhaven Medical Research Reactor (BMRR) [Corderre, 1992], the 5 MW Massachusetts Institute of Technology Research Reactor (MITR-II) [Solares, 1993] and the MUSASHI reactor [Aizawa, 1990]. The thermal beam of the MUSASHI reactor is used for clinical treatments, while the other two are used for radiobiological research. Table 2.9 shows the beam parameters in free-air at the target positions of the various reactors. From this comparison it appears that the thermal fluence rate of the LFR is comparable with the other ones and that the configuration chosen for the LFR efficiently makes use of the available neutrons. Additionally, the comparison of the ratio between the thermal neutron fluence rate and the total dose rate from contaminant

components for the different beams shows that the thermal facility at the LFR is very appropriate as radiobiological test facility.

Table 2.9: Comparison of the LFR thermal neutron beam with other thermal neutron sources.

reactor	LFR	BMRR	MITR-II	MUSASHI
reactor power P	30 kW	1 MW	4.5 MW	100 kW
ϕ_0 [$10^9 \text{ cm}^{-2} \text{ s}^{-1}$] ^a	1.1 ± 0.2	9.8	1.3 ± 0.3	1.1
$\dot{D}_{\text{fast}} + \dot{D}_{\text{epi}}$ [Gy/h]	0.3 ± 0.1	16.2	0.8 ± 0.1	0.1^b
\dot{D}_{γ} [Gy/h]	$0.6^c \pm 0.1$	6.6	7.3 ± 0.4	0.4
$R(\text{RBE} = 1)$	$1.2 \cdot 10^9$	$0.43 \cdot 10^9$	$0.16 \cdot 10^9$	$2.2 \cdot 10^9$
ϕ_0/P [$\text{cm}^{-2} \text{ s}^{-1} \text{ MW}^{-1}$]	$37 \cdot 10^9$	$9.8 \cdot 10^9$	$0.29 \cdot 10^9$	$11 \cdot 10^9$

^a) 2200 m/s fluence rate ^b) estimation based on fluence rates

^c) γ -ray contribution of the sample changer is not taken into account

2.5 Conclusions about the thermal neutron facility

To realise the requirements for a biological test facility, i.e. a thermal fluence rate of at least $1.0 \cdot 10^9 \text{ cm}^{-2} \text{ s}^{-1}$ and a total dose rate from contaminant components lower than 1 Gy/h, a number of Monte Carlo calculations were performed resulting in a configuration whose performance slightly exceeded the requirements. A careful experimental verification of the calculations showed that the parameters obtained with the final model leads to an accurate prediction of the measured results.

Comparing available thermal facilities elsewhere for BNCT, the new facility at the LFR gives a good ratio between the thermal fluence rate and the sum of the fast and photon dose rates. Since the construction of the facility in April 1994, it is used for different radiobiological experiments and for calibration of neutron detectors [Raaijmakers, 1996].

Chapter 3

Generalised perturbation theory for reactor calculations

The effect of the material choice on the quality of the thermal facility can be determined by a large number of forward calculations. A faster way of determination can be obtained by using the techniques of perturbation theory, relating changes in input quantities to changes in output quantities (responses) without calculating the perturbed dependent variable. In this chapter, the perturbation theory is elaborated for a response function defined as the ratio between two linear functions of the fluence rate. Perturbation theory for this type of response functions is called generalised perturbation theory. The derived techniques are implemented in existing computer codes.

3.1 The Boltzmann transport equation

The behaviour of a nuclear reactor can be described by the distribution in time and space of neutrons in the reactor. This distribution can be expressed by counting the creation, scattering, absorption and leakage of neutrons in the reactor. The Boltzmann transport equation [Duderstadt, 1976] is one of the possible ways to describe the neutron transport:

$$\frac{1}{v} \frac{\partial \phi}{\partial t} + \boldsymbol{\Omega} \cdot \nabla \phi + \Sigma_t(\mathbf{r}, E) \phi(\mathbf{r}, E, \boldsymbol{\Omega}, t) - \quad (3.1)$$

$$\int \int \Sigma_s(\mathbf{r}, E' \rightarrow E, \boldsymbol{\Omega}' \rightarrow \boldsymbol{\Omega}) \phi(\mathbf{r}, E', \boldsymbol{\Omega}', t) dE' d\boldsymbol{\Omega}' =$$

$$\frac{1}{4\pi} \chi(\mathbf{r}, E) \int \int \nu(\mathbf{r}, E') \Sigma_f(\mathbf{r}, E') \phi(\mathbf{r}, E', \boldsymbol{\Omega}', t) dE' d\boldsymbol{\Omega}' + S(\mathbf{r}, E, \boldsymbol{\Omega}, t),$$

where,

E	= neutron energy	[J]
\mathbf{r}	= position	[cm]
t	= time	[s]
v	= neutron velocity	[cm s ⁻¹]
S	= extraneous neutron source	[cm ⁻³ s ⁻¹]
ν	= mean number of neutrons produced per fission	
Σ_a	= macroscopic absorption cross section	[cm ⁻¹]
Σ_f	= macroscopic fission cross section	[cm ⁻¹]
Σ_s	= macroscopic scattering cross section	[cm ⁻¹]
Σ_t	= macroscopic total cross section	[cm ⁻¹]
χ	= normalised fission spectrum	
ϕ	= forward neutron fluence rate	[cm ⁻² s ⁻¹]
$\boldsymbol{\Omega}$	= unit direction vector	
∇	= gradient	

If the production rate of neutrons in the reactor equals the loss due to absorption or leakage, a time-independent neutron fluence rate is present in

the reactor. The static or steady-state transport equation can be written as

$$\mathbf{L}\phi(\mathbf{r}, E, \boldsymbol{\Omega}) = \mathbf{P}\phi(\mathbf{r}, E, \boldsymbol{\Omega}) + S(\mathbf{r}, E, \boldsymbol{\Omega}), \quad (3.2)$$

where the loss term $\mathbf{L}\phi$ is equal to

$$\begin{aligned} \mathbf{L}\phi(\mathbf{r}, E, \boldsymbol{\Omega}) = & \boldsymbol{\Omega} \cdot \nabla \phi(\mathbf{r}, E, \boldsymbol{\Omega}) + \Sigma_t(\mathbf{r}, E)\phi(\mathbf{r}, E, \boldsymbol{\Omega}) - \\ & \int \int \Sigma_s(\mathbf{r}, E' \rightarrow E, \boldsymbol{\Omega}' \rightarrow \boldsymbol{\Omega})\phi(\mathbf{r}, E', \boldsymbol{\Omega}')dE'd\boldsymbol{\Omega}', \end{aligned} \quad (3.3)$$

and the production term $\mathbf{P}\phi$ equals

$$\mathbf{P}\phi(\mathbf{r}, E, \boldsymbol{\Omega}) = \frac{1}{4\pi}\chi(\mathbf{r}, E) \int \int \nu(\mathbf{r}, E')\Sigma_f(\mathbf{r}, E')\phi(\mathbf{r}, E', \boldsymbol{\Omega}')dE'd\boldsymbol{\Omega}'. \quad (3.4)$$

A reactor in which a time independent neutron fluence rate can be sustained in absence of neutron sources other than fission, is called critical. If the production term is somewhat smaller than the loss term (subcritical), the neutron population must decrease in time. For a real reactor, it is possible to get a steady state condition by some physical changes in the core or its surroundings. Mathematically, the transport equation can be forced into a steady state condition by converting it into an eigenvalue problem:

$$(\mathbf{L} - \lambda\mathbf{P})\phi = 0, \quad (3.5)$$

in which λ is an eigenvalue of this system. For every reactor geometry and for every reactor composition, there is only one unique value of λ which will enforce equality between source and loss rate terms. Although λ is a mathematical way of forcing the equation into a steady state condition, it has a physical meaning. If $\lambda < 1$, the source term will have to be decreased to make the steady state possible, the reactor is supercritical. Inversely, a reactor is called subcritical if $\lambda > 1$, the source term has then to be increased before a steady state neutron population can be achieved. In reactor physics the inverse of λ is called the effective multiplication factor k_{eff} .

3.2 The adjoint transport equation

The generalised perturbation theory is like other perturbation techniques based on forward and adjoint equations. Analogous to the Boltzmann equation an adjoint transport equation can be described.

The operator \mathbf{L}^* , adjoint to operator \mathbf{L} , is defined so that any function ψ^* fulfilling continuity and boundary conditions, which may be different from those on ϕ , will satisfy the relation:

$$\langle \psi^*, \mathbf{L}\phi \rangle = \langle \phi, \mathbf{L}^*\psi^* \rangle. \quad (3.6)$$

The notation \langle , \rangle is defined as an integration over position, energy and solid angle:

$$\langle p , q \rangle = \int_{\mathbf{r}} \int_E \int_{\Omega} p \cdot q \, d\mathbf{r} \, dE \, d\Omega. \quad (3.7)$$

Also for the operator \mathbf{P} an adjoint operator \mathbf{P}^* can be defined satisfying the relation:

$$\langle \psi^*, \mathbf{P}\phi \rangle = \langle \phi, \mathbf{P}^*\psi^* \rangle. \quad (3.8)$$

In accordance with the definition of the adjoint transport operators \mathbf{L}^* and \mathbf{P}^* , the adjoint transport equation is:

$$-\Omega \cdot \nabla \psi^*(\mathbf{r}, E, \Omega) + \Sigma_t(\mathbf{r}, E) \psi^*(\mathbf{r}, E, \Omega) - \quad (3.9)$$

$$\int \int \Sigma_s(\mathbf{r}, E \rightarrow E', \Omega \rightarrow \Omega') \psi^*(\mathbf{r}, E', \Omega') dE' d\Omega' =$$

$$\frac{1}{4\pi} \nu(\mathbf{r}, E) \Sigma_f(\mathbf{r}, E) \int \int \chi(\mathbf{r}, E') \psi^*(\mathbf{r}, E', \Omega') dE' d\Omega' + S^*(\mathbf{r}, E, \Omega).$$

The term ψ^* is called the adjoint function. The dimensions of the adjoint function depends on the dimension of the adjoint source.

3.3 Perturbations of reactor geometry or composition

Changes in the reactor geometry or material composition can be seen as changes in the macroscopic cross section which will perturb the operators \mathbf{L} and \mathbf{P} :

$$\begin{aligned}\mathbf{L} &\rightarrow \mathbf{L} + \Delta\mathbf{L}, \\ \mathbf{P} &\rightarrow \mathbf{P} + \Delta\mathbf{P}.\end{aligned}\tag{3.10}$$

Changes in the loss and production term will subsequently perturb the eigenvalue λ and the fluence rate ϕ :

$$\begin{aligned}\lambda &\rightarrow \lambda + \Delta\lambda, \\ \phi &\rightarrow \phi + \Delta\phi.\end{aligned}\tag{3.11}$$

The perturbed transport equation can be written as:

$$[(\mathbf{L} + \Delta\mathbf{L}) - (\lambda + \Delta\lambda)(\mathbf{P} + \Delta\mathbf{P})](\phi + \Delta\phi) = 0.\tag{3.12}$$

Expanding this equation and leaving out all terms of second order and higher, gives

$$\mathbf{L}\phi + \mathbf{L}\Delta\phi + \Delta\mathbf{L}\phi - \lambda\mathbf{P}\phi - \lambda\Delta\mathbf{P}\phi - \lambda\mathbf{P}\Delta\phi - \Delta\lambda\mathbf{P}\phi = 0.\tag{3.13}$$

With the knowledge that $(\mathbf{L} - \lambda\mathbf{P})\phi = 0$, equation 3.13 reduces to

$$(\Delta\mathbf{L} - \lambda\Delta\mathbf{P})\phi - \Delta\lambda\mathbf{P}\phi + (\mathbf{L} - \lambda\mathbf{P})\Delta\phi = 0.\tag{3.14}$$

Now consider the adjoint equation for the eigenvalue problem (the eigenvalue of the adjoint problem is equal to the eigenvalue of the forward problem)

$$(\mathbf{L}^* - \lambda\mathbf{P}^*)\psi^* = 0,\tag{3.15}$$

and the fixed source adjoint equation:

$$(\mathbf{L}^* - \lambda\mathbf{P}^*)\Gamma^* = S^*,\tag{3.16}$$

The operator $(\mathbf{L}^* - \lambda \mathbf{P}^*)$ in equation 3.16 is singular. Solutions of equation 3.16 exist only if the adjoint source S^* is perpendicular to a function y that obeys the condition

$$(\mathbf{L} - \lambda \mathbf{P})y = 0. \quad (3.17)$$

This equation is the transport equation for eigenvalue problems (equation 3.5), which can be solved resulting in the forward fluence rate ϕ . A singular system has either no solutions or an infinitely number of solutions. If the adjoint source S^* is chosen perpendicular to the forward fluence rate ϕ , equation 3.16 has the following solutions:

$$\Gamma^* = \Gamma_p^* + a\psi^*, \quad (3.18)$$

where Γ_p^* is a particular solution of equation 3.16, a an arbitrary constant and ψ^* the adjoint function which satisfies equation 3.15.

After multiplying equation 3.14 by Γ^* and equation 3.16 by $\Delta\phi$ and subtracting the two new equations, the following relation remains

$$\begin{aligned} \Gamma^* \Delta \mathbf{L} \phi - \lambda \Gamma^* \Delta \mathbf{P} \phi - \Delta \lambda \Gamma^* \mathbf{P} \phi + \Gamma^* \mathbf{L} \Delta \phi - \\ \lambda \Gamma^* \mathbf{P} \Delta \phi - \Delta \phi \mathbf{L}^* \Gamma^* - \lambda \Delta \phi \mathbf{P}^* \Gamma^* = -S^* \Delta \phi. \end{aligned} \quad (3.19)$$

After integration of equation 3.19 over space, energy and solid angle, the fourth term and the sixth term as well as the fifth term and the seventh term cancel by definition of the adjoint operators (equation 3.6 and equation 3.8), leaving:

$$\langle \Gamma^* (\Delta \mathbf{L} - \lambda \Delta \mathbf{P}) \phi \rangle - \Delta \lambda \langle \Gamma^* \mathbf{P} \phi \rangle = - \langle S^* \Delta \phi \rangle. \quad (3.20)$$

The notation $\langle \rangle$ for a function is also defined as an integration over position, energy and solid angle:

$$\langle f \rangle = \int_{\mathbf{r}} \int_E \int_{\Omega} f \, d\mathbf{r} \, dE \, d\Omega. \quad (3.21)$$

The difference in λ due to the differences in the cross sections can only be determined by lengthy forward calculations. If the arbitrary constant a in equation 3.18 is chosen so that

$$\langle \Gamma^* \mathbf{P} \phi \rangle = 0, \quad (3.22)$$

equation 3.20 becomes only dependent on the (known) differences in cross sections and the differences in fluence rate:

$$\langle \Gamma^*(\Delta\mathbf{L} - \lambda\Delta\mathbf{P})\phi \rangle = - \langle S^*\Delta\phi \rangle. \quad (3.23)$$

Equation 3.22 fixes the value of a which ensures a unique value for Γ^* .

3.4 Response function

In section 2.1.2, an example was presented of a direct calculation of a specific response function. This chapter gives a general treatment of a first order calculation of any response function using the techniques of the generalised perturbation theory.

The deduction in the previous section is valid independent of the type of response function. By limiting the possible response functions, however, it is possible to calculate to a first order accuracy the perturbations in the response function without knowing the perturbation in the fluence rate $\Delta\phi$.

The response function R is defined as an arbitrary functional quotient

$$R = \frac{\langle H_1\phi \rangle}{\langle H_2\phi \rangle}, \quad (3.24)$$

where H_1 and H_2 are linear self-adjoint operators. The operators are defined such that they are non-zero only in a detector position. Perturbation theory for these types of responses is called generalised perturbation theory. The response function defined in section 2.1.2, is a good example.

A change in macroscopic cross sections, appearing in the transport equation and also possibly in the definition of the operators H_1 and H_2 , will cause a change in the fluence rate and thereby a change in the response function. The change in the response function R can be calculated to first-order accuracy by the total variation

$$\Delta R \simeq \frac{\partial R}{\partial \Sigma} \Delta \Sigma + \frac{\partial R}{\partial \phi} \Delta \phi. \quad (3.25)$$

The first term is called the "direct effect" of the cross section change, the second term the "indirect effect". The direct effect can be written as

$$\frac{\partial R}{\partial \Sigma} \Delta \Sigma = \frac{\langle \frac{\partial}{\partial \Sigma}(H_1 \phi) \Delta \Sigma \rangle \langle H_2 \phi \rangle - \langle \frac{\partial}{\partial \Sigma}(H_2 \phi) \Delta \Sigma \rangle \langle H_1 \phi \rangle}{\langle H_2 \phi \rangle^2}, \quad (3.26)$$

or, simplifying,

$$\begin{aligned} \frac{\partial R}{\partial \Sigma} \Delta \Sigma &= R \left[\frac{\langle \frac{\partial}{\partial \Sigma}(H_1 \phi) \Delta \Sigma \rangle}{\langle H_1 \phi \rangle} - \frac{\langle \frac{\partial}{\partial \Sigma}(H_2 \phi) \Delta \Sigma \rangle}{\langle H_2 \phi \rangle} \right] \\ &= R \left[\left(\frac{\frac{\partial}{\partial \Sigma}(H_1 \phi)}{\langle H_1 \phi \rangle} - \frac{\frac{\partial}{\partial \Sigma}(H_2 \phi)}{\langle H_2 \phi \rangle} \right) \Delta \Sigma \right], \end{aligned} \quad (3.27)$$

where $H_1 \phi(\Sigma + \Delta \Sigma)$ is per definition equal to

$$H_1 \phi(\Sigma + \Delta \Sigma) = H_1 \phi(\Sigma) - \frac{\partial H_1 \phi}{\partial \Sigma} \Delta \Sigma. \quad (3.28)$$

This term can be calculated easily for each $\Delta \Sigma$. Analogously, the variation with respect to the fluence rates equals

$$\begin{aligned} \frac{\partial R}{\partial \phi} \Delta \phi &= R \left[\frac{\langle \frac{\partial}{\partial \phi}(H_1 \phi) \Delta \phi \rangle}{\langle H_1 \phi \rangle} - \frac{\langle \frac{\partial}{\partial \phi}(H_2 \phi) \Delta \phi \rangle}{\langle H_2 \phi \rangle} \right] \\ &= R \left[\left(\frac{\frac{\partial}{\partial \phi}(H_1 \phi)}{\langle H_1 \phi \rangle} - \frac{\frac{\partial}{\partial \phi}(H_2 \phi)}{\langle H_2 \phi \rangle} \right) \Delta \phi \right]. \end{aligned} \quad (3.29)$$

If the adjoint source S^* is chosen as

$$S^* = \frac{\frac{\partial}{\partial \phi}(H_1 \phi)}{\langle H_1 \phi \rangle} - \frac{\frac{\partial}{\partial \phi}(H_2 \phi)}{\langle H_2 \phi \rangle}, \quad (3.30)$$

then S^* is perpendicular to the forward fluence rate ϕ and equation 3.16 is solvable. The indirect effect of the cross section change (see equation 3.23) can be written as

$$\frac{\partial R}{\partial \phi} \Delta \phi = -R \langle \Gamma^* (\Delta \mathbf{L} - \lambda \Delta \mathbf{P}) \phi \rangle. \quad (3.31)$$

The total change in the response function R , accurate through all first order terms, can be expressed by the following perturbation expression

$$\frac{\Delta R}{R} \simeq \frac{\langle \frac{\partial}{\partial \Sigma} (H_1 \phi) \Delta \Sigma \rangle}{\langle H_1 \phi \rangle} - \frac{\langle \frac{\partial}{\partial \Sigma} (H_2 \phi) \Delta \Sigma \rangle}{\langle H_2 \phi \rangle} - \quad (3.32)$$

$$\langle \Gamma^* (\Delta \mathbf{L} - \lambda \Delta \mathbf{P}) \phi \rangle . \quad (3.33)$$

3.5 The DORT and SUSD computer-codes

Instead of considering each perturbation in the material composition of the thermal facility with a new forward transport problem, the effect on the response function can be obtained by solving a set of three transport problems once which can be used for all possible perturbations in the material composition. The three transport problems which must be solved are:

- the forward eigenvalue problem (equation 3.5),
- the adjoint equation for eigenvalue problems (equation 3.15),
- and the fixed source adjoint equation (equation 3.16).

The computer-code DORT [Rhoades, 1986], a two-dimensional discrete ordinates transport code, determines the fluence rate of particles throughout one- or two-dimensional geometric systems due to particles in the system from extraneous sources or generated internally as a result of interaction with the system. This code, in its original form, is capable to solve the forward or adjoint transport equation using the method of discrete ordinates. To solve the fixed source adjoint equation, extensive alterations to the code have been applied [Vroegindewij, 1992b]. For user comfort, three different problems were solved in one computer run, calculating the forward fluence rate ϕ and the adjoint functions ψ^* and Γ^* .

Knowing the fluence rate and adjoint functions the change in the response function can be obtained by equation 3.33. The integrals over energy, space and solid angle of the product of the fluence rates and changes in cross sections are calculated as described in equation 3.32 and are almost similar to the integral equations which are solved in normal sensitivity and uncertainty analysis of cross sections. The computer code SUSD (Sens-

itivity and Uncertainty with Secondary Distributions) [Furuta, 1982] has already been used to analyse this type of integral equations and with some extensions this program can be used for generalised perturbation theory [Vroegindeweij, 1996b].

3.6 Conclusions about the generalised perturbation theory

A quick investigation of the effects of another material choice is possible with the techniques of generalised perturbation theory. The techniques are derived to use them for these types of problems. Necessary changes are added to the two-dimensional discrete ordinates transport code DORT and the sensitivity uncertainty analysis code SUSD.

Using a response function which is equal to the ratio of the desired (thermal) neutron intensity and the unwanted (fast) neutron intensity, both at the irradiation position, the effect of another material composition can be obtained in a very short computation time.

Within the framework of this thesis, no further optimisation studies have been performed. However, the methods described in this chapter and implemented in the above mentioned computer codes finish the tools for further optimisation of the thermal BNCT facility at the Low Flux Reactor.

Chapter 4

Conclusions about the reactor calculations

For the research activities of BNCT, there is great interest in a thermal neutron facility to perform radiobiological experiments. As no facility was available in Petten, a development study for a thermal facility at the LFR reactor in Petten was started. Reasons for the development study besides the beam requirements are the easy replacement of the facility and low budget. The facility has been placed on the irradiation trolley (see figure 1.1). Therefore reconstruction of the reactor or the reactor hall is prohibitive. Based on the restrictions of the development study, the thermal facility consists of an additional graphite reflector and a lead shielding wall. Around the irradiation position only, the lead is replaced by bismuth, leading to a smaller reduction of the thermal fluence rate and a lower γ -ray background at the irradiation position.

The design of the facility was based on the results of an optimisation study with respect to a biological response function. The neutron and photon transport calculations have been performed with the Monte Carlo

code MCNP. This study has been performed to determine the optimal thickness of the graphite moderator and the position of the bismuth window in the shielding wall. The response function has been defined as the ratio between the thermal fluence rate and the dose rate from the other neutrons and the photons, both considered at the irradiation position in the bismuth window. The response from biological targets has been included to model a target consisting of biologically equivalent materials. The fact that different kinds of irradiation cause different effects was considered by multiplying the neutron dose rate with the RBE value. Three different values of the RBE have been considered to compensate uncertainties in the determinations of the RBE's. The photon RBE is by definition equal to 1.

The thermal fluence rate decreases with an increasing graphite thickness, but also the dose rate of the contaminant beam components decreases. The optimal graphite thickness is independent of the values of the RBE. In all three cases the optimal thickness is about 54 cm, resulting in a thermal fluence rate that is approximately 30% higher than the lower limit of $1 \cdot 10^9 \text{ cm}^{-2}\text{s}^{-1}$, and a physical dose component of 1.6 Gy/h including the photon dose from the modelled biological target. A separate run has shown that approximately 40% of the photon dose originates from the biological target. The total physical dose, the sum over the photon dose and the neutron dose, without the contribution of the biological target is 1.2 Gy/h at the irradiation position. The optimisation of the position of the bismuth window in the lead shield gives less clear result. The thermal fluence and the dose components decrease slowly moving from the right edge to the left (looking from the east side of the reactor towards the reactor core). The window is placed in the middle of the lead shield. At this position a thermal fluence rate of $1.23 \cdot 10^9 \text{ cm}^{-2}\text{s}^{-1}$ is calculated with a physical dose component of 1.2 Gy/h. Using the same ratio of 40% between the beam photon dose and the photon dose from the biological target, this position complies with both constraints for the facility: the thermal fluence rate is more than 20% higher than the lower limit, while the dose rate from beam contamination is 20% lower than its upper limit.

In the optimisation study the steel construction for rigidity and positioning of the facility on the trolley has not been taken into account. In a new

model, however, based on the results of the optimisation study, it has been determined that the influence of the construction materials on the fluence and dose rates is negligible; differences are smaller than 5%. In nine different volume detectors, the thermal fluence rate and the fast and photon dose rates have been determined to obtain the variation of these components over the irradiation window. This variation is small for all components and decreases with a maximum of 15% going from the right to the left side of the window (seen from the east side of the reactor towards the reactor core), which is plausible because the right side of the window is a bit closer to the reactor core than the left side. The variation in the vertical direction is much smaller and not significant.

After realisation of the facility, the calculated parameters have been verified using neutron activation detectors (foils). At nine positions, MnNi foils have been irradiated and at the centre of the window, Cu, AuAl and Ni foils have also been placed. The calculated manganese reaction rates are on average 15% higher than the measured reaction rates. Looking at the relative course of the reaction rates, the agreement between measurement and calculations is even better. Also, the measured and calculated values of the foil set in the centre of the window are comparable. Nevertheless, again here, the calculations are slightly higher than the measurements. The differences between measurements and calculations are acceptable for such a deep penetration problem, keeping in mind the uncertainties in the cross section libraries, assumptions in the model of the LFR and the complication of the power calibration at (low) reactor power.

Comparing the characteristics of the LFR thermal facility with three other reactors that also have thermal facilities for BNCT, the beam at the LFR can clearly withstand this comparison very well. Although the LFR has a low power, the thermal fluence rate is comparable with the other ones while the ratio between the thermal fluence rate and the γ -ray and fast neutron dose rates are better than MITR-II and BMRR. Only the MUSASHI reactor has a better ratio, but this reactor is used for clinical treatment of melanomas, resulting in more severe constraints than facilities for radiobiological research.

For further development of the facility, the influence of the restriction

of choosing an additional moderator of graphite has to be considered. This can be done with many forward calculations using different compositions and materials, which is a very time consuming method. To reduce considerably the amount of time, techniques of generalised perturbation theory have been developed. These techniques have been implemented in the transport code DORT and the sensitivity code SUSD to handle such problems.

References

Aizawa, O. (1990), 'Research on neutron beam design for BNCT at the MUSASHI reactor,' in *Neutron beam design, development, and performance for neutron capture therapy*, Editors: O.K. Harling, J.A. Bernard, R.G. Zamenhof, 109-124, Plenum Press, New York.

Attics, F.H. (1986), 'Introduction to radiological physics and radiation dosimetry', Wiley.

Booth, F.E. (1985), 'A sample problem for variance reduction in MCNP,' *Los Alamos Report LA-10363-MS*, UC-32.

Braak, J.P. (1987), 'De Lage Flux Reactor te Petten,' *ECN report ECN-87-172*, Petten, The Netherlands.

Briesmeister, J.E., ed. (1993), 'MCNP, A general Monte Carlo code for neutron and photon transport, version 4A', *Los Alamos Report LA-12625*.

Coderre, J.A., Darrel, D.J., Micca, P.L., Nawrocky, M.M., Slatkin, D.N. (1992), 'Control of intracerebral gliosarcomas in rats by boron neutron capture therapy with *p*-boronophenylalanine,' *Radiat.Res.*, Vol 129, 290-296.

Crawford, J.F., Stecher-Rasmussen, F. (1993), 'A scintillation spectrometer for direct comparison of neutron energy spectra at high and low rates,' in: *Advances in Neutron Capture Therapy*, Editors: A.H. Soloway, R.F. Barth, D.E. Carpenter, 207-211, Plenum Press, New York.

Davids, J.A.G., Mos, A.P.J., Oude, A. de (1969), 'Fast neutron facility for biological exposures in an Argonaut reactor: design, tissue dosimetry and neutron spectrometry,' *Phys.Med.Biol.* Vol 14, 573-584.

- Duderstadt, J.J. and Hamilton, L.J. (1976), 'Nuclear Reactor Analysis,' J. Wiley, New York.
- Freudenreich, W.E., Stecher-Rasmussen, F., Haas, J.B.M. de (1992), 'Development study of a biological thermal facility for the Petten BNCT project at the LFR,' *ECN report: ECN-I-92-022*, Petten, the Netherlands.
- Furuta, K., Oka, Y., and Kondo, S. (1986), 'SUSD: A computer code for cross section sensitivity and uncertainty analysis including secondary neutron energy and angular distributions,' *UTNL-R-0185*.
- Huiskamp, R., Davids, J., Vos, O. (1983), 'Short and long term effects of whole body irradiation with fission neutrons or X-rays on the thymus in CBA mice,' *Radiat. Res.* Vol 95, 370-381.
- ICRU report No. 26 (1979), 'Neutron Dosimetry for biology and medicine.'
- Konijnenberg, M.W., Mijnheer, B.J., Raaijmakers, C.P.J., Stecher-Rasmussen, F., Watkins, P.R.D. (1993), 'Measurements and calculations for Boron Neutron Capture Therapy treatment planning,' in *Advances in Neutron Capture Therapy*, Editors: A.H. Soloway, R.F. Barth, D.E. Carpenter, 159-164, Plenum Press, New York.
- Kraakman, R.W.A., Voorbraak, W.P. (1982), 'Power calibration and fluence rate measurements,' unpublished laboratory note FYS/RASA-83/03, ECN, Petten, the Netherlands.
- Paardekoper, A. and Voorbraak, W.P. (1994), private communication, Netherlands Energy Research Foundation (ECN), Petten, The Netherlands.
- Raaijmakers, C.P.J., Watkins, P.R.D., Nottelman, E.L., Verhagen, H.W., Janssen, J.T.M., Zoetelief, J., Mijnheer, B.J. (1996), 'Neutron sensitivity of dosimetry applied to BNCT,' *Med. Phys.* Vol. 23, 1581-1589
- Rhoades, W.A., Childs, R.L. (1986), 'An Undated Version of the DOT 4 one and two Dimensional Neutron/Photon Transport Code,' *Report: LA-7396-M, Revision 2*, Los Alamos.
- Sauwerwein, W., Szypniewski, H., Pöller, F., Huiskamp, R. (1992), 'Dose modification by neutron capture in cell culture using a 1 MeV mean energy fission neutron beam,' in *Progress in Neutron Capture Therapy for Cancer*, Editors: B.J. Allen, D.E. Moore, B.V. Harrington, 399-401, Plenum Press, New York.
- Schneider, W. (1973), 'Neutronenmesstechnik und ihre Anwendung an Kernreaktoren,' Walter de Gruyter, Berlin.

Solares, G.R., Zamenhof, R.G., Wazer, D.E., DiPetrillo, T.A., Saris, S.C., Cano, G., Madoc-Jones, H., Harling, O. (1993), 'Effects of fractionation of Boron Neutron Capture Therapy in a mouse glioma model,' in *Advances in Neutron Capture Therapy*, Editors: A.H. Soloway, R.F. Barth, D.E. Carpenter, 525-528, Plenum Press, New York.

Verbakel, W.F.A.R. (1995), 'A γ -ray telescope for on-line measurements of low boron concentration in a head phantom for BNCT,' *ECN report: ECN-I-95-051*, Petten, the Netherlands.

Vroegindeweij, C. (1992a) 'Generalized Perturbation Theory, A tool to design a suitable reactor facility for Boron Neutron Capture Therapy,' *ECN report: ECN-I-92-034*, Petten, the Netherlands.

Vroegindeweij, C. (1992b), 'Het twee-dimensionale transport programma DORT,' *ECN report NFA-LWR-92-07*, Petten, the Netherlands.

Vroegindeweij, C., Stecher-Rasmussen, F., Haas, J.B.M. de (1994), 'A thermal neutron facility for biological BNCT-studies at the LFR,' *ECN report: ECN-I-94-009*, Petten, the Netherlands.

Vroegindeweij, C., Stecher-Rasmussen, F., Haas, J.B.M. de (1996a), 'A thermal neutron facility for biological BNCT-studies at the LFR,' *Annals of Nuclear Energy*, Vol 23, 1229-1238.

Vroegindeweij, C. (1996b), 'Extensions to the computer code SUSL,' ECN report, in progress, ECN, Petten, the Netherlands.

Zijp, W.L., Nolthenius, H.J., and Verhaag, G.C.H.M (1984), 'Cross-section library DOSCROS84, in a 640 group structure of the SAND-II type,' *ECN report: ECN-160*, Petten, The Netherlands.

Nomenclature

List of symbols

a	normalisation factor	
\dot{D}_{epi}	dose rate for epithermal neutrons	Gy h ⁻¹
\dot{D}_{fast}	dose rate for fast neutrons	Gy h ⁻¹
\dot{D}_{γ}	dose rate for γ -rays	Gy h ⁻¹
E	energy	eV
\mathbf{r}	position	cm
R	response function	
P	reactor power	MW
t	time	s
v	speed	cm s ⁻¹
S	extraneous source	cm ⁻³ s ⁻¹
S^*	adjoint extraneous source	
Γ^*	adjoint function	
λ	eigenvalue	
ν	mean number of neutrons produced per fission	
Σ	macroscopic cross section	cm ⁻¹
Σ_a	macroscopic absorption cross section	cm ⁻¹
Σ_f	macroscopic fission cross section	cm ⁻¹
Σ_s	macroscopic scattering cross section	cm ⁻¹
Σ_t	macroscopic total cross section	cm ⁻¹
χ	(normalised) fission spectrum	
ϕ	forward neutron fluence rate	cm ⁻² s ⁻¹
ϕ_0	2200 m/s neutron fluence rate	cm ⁻² s ⁻¹
ϕ_{th}	thermal neutron fluence rate	cm ⁻² s ⁻¹
ϕ_{epi}	epithermal neutron fluence rate	cm ⁻² s ⁻¹
ϕ_{fast}	fast neutron fluence rate	cm ⁻² s ⁻¹

ψ^*	adjoint function
Ω	unit direction vector

Operators

H_1	linear self-adjoint operator on ϕ
H_2	linear self-adjoint operator on ϕ
L	loss term
L^*	adjoint operator
P	production term
P^*	adjoint operator
∇	gradient
$\langle p, q \rangle$	$= \int_{\mathbf{r}} \int_E \int_{\Omega} p \cdot q \, d\mathbf{r} \, dE \, d\Omega$
$\langle f \rangle$	$= \int_{\mathbf{r}} \int_E \int_{\Omega} f \, d\mathbf{r} \, dE \, d\Omega$

List of abbreviations

BNCT	Boron Neutron Capture Therapy
BMRR	Brookhaven Medical Research Reactor
DORT	two-dimensional Discrete ORdinates Transport code
ENDF/B-V	Evaluated Nuclear Data File/B-V
ICRU	International Commission on Radiation Units and measurements
LFR	Low Flux Reactor
MCNP	Monte Carlo N-Particles transport code
MITR-II	Massachusetts Institute of Technology Research Reactor-II
RBE	Relative Biological Effectiveness

Part II

Phantom calculations

Chapter 5

Introduction to phantom irradiations

The primary objective of the Petten BNCT project is to treat patients with brain tumours. To generate a sufficient intensity of thermal neutrons at depth in the brain of a patient the head will be irradiated with epithermal neutrons. By thermalisation of the epithermal neutrons in the hydrogenous brain tissue a cloud of thermal neutrons is generated over a certain volume of the brain. If the tumour tissue contains boron then these thermal neutrons will lead to the capture reaction in ^{10}B , emitting α - and Li-particles. The resulting field of radiation, including radiation from other neutron induced reactions in the head of the patient and photons from the incident beam, will destroy the tumour tissue. To date, a sufficient and adequate fluence rate of epithermal neutrons for BNCT applications can presently only be acquired from nuclear reactors.

At the High Flux Reactor (HFR) at Petten [Moss, 1992], owned by the Commission of the European Communities, an epithermal beam has been developed, suitable for BNCT. A horizontal cross section of the BNCT

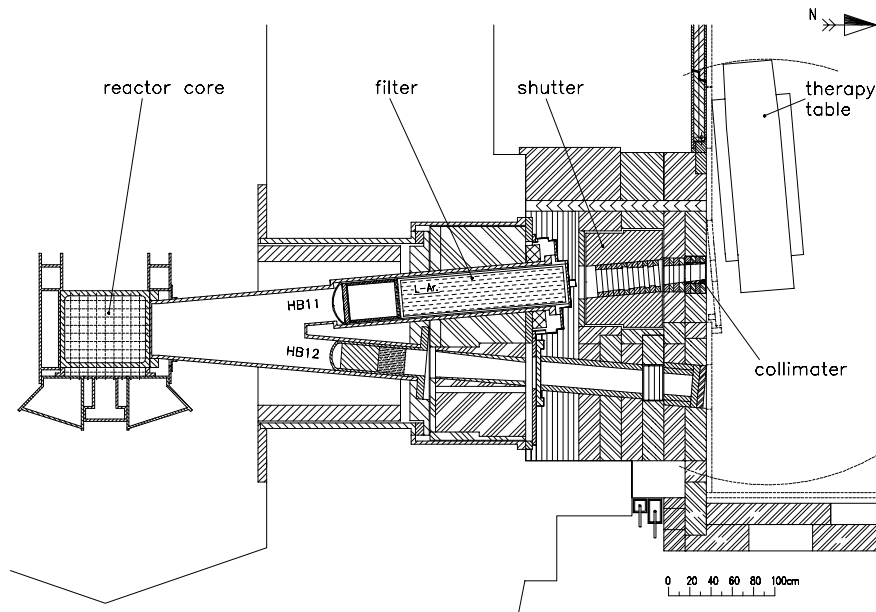


Figure 5.1: Overview of the HFR and the HB11 beam tube

facility is shown in figure 5.1. Primarily the HFR is utilised for the testing of materials under irradiation. The reactor operates at 45 MW and is cooled and moderated by light water. The standard core configuration consists of 33 fuel assemblies, 6 control rods and 17 free positions for placing experimental facilities in a regular square construction surrounded on three side by beryllium reflector elements. The reactor is also equipped with 12 horizontal beam tubes, suitable for nuclear physics and solid state physics research. In one of these horizontal tubes, the HB11 tube at the North side of the reactor, a combination of materials has been placed to filter and moderate the neutron and photon radiation emerging from the reactor, without reducing the epithermal neutron intensity too severely. This filter configuration consists of a 1 mm thick cadmium shield (reducing the thermal fluence rate) followed by 150 mm aluminium, 10 mm titanium, 50 mm sulphur (all three reducing the fast neutron fluence rate) and 1500 mm liquid argon (to reduce the photon beam)[Watkins, 1992].

Despite the efforts to reduce the unwanted components of the beam, a

filtered beam is still a radiation source containing neutrons of all energies and photons. The radiobiological effects associated with the irradiation of healthy and tumour tissue with such a mixed field has to be determined. As part of the radiobiological research, studies with cell-cultures have been performed. In July 1991, a first large experiment on the effects of mixed field irradiations was performed at the HB11 facility, using cell cultures of the V79 Chinese hamster cells. In this experiment single cell suspensions were placed in small vials at radially and axially distributed positions in a cylindrical phantom, filled with water to moderate the epithermal and fast neutrons.

This experiment is analysed in chapter 12 using the microdosimetry model. For the analysis, information about the neutron energy spectrum at the various irradiation positions in the phantom is needed. In the section here, calculations of the neutron spectra and photon dose rates are presented. The calculations are performed by means of the two dimensional deterministic transport code DORT [Rhoades, 1986] and verified with measured reaction rates, using activation foils, and dose rates obtained from measurements with ionisation chambers. Because the verification with measurements is only possible for energy integrated reaction and dose rates, the spectra on the irradiation positions are compared with calculations performed with another computer code, viz. the three dimensional Monte Carlo program MCNP [Briesmeister, 1993].

Chapter 6

Calculations for a cylindrical phantom

A cylindrical phantom made at the University of Bremen was used in radiobiological experiments which were performed to investigate the effect of mixed field irradiations on cell cultures. Small vials with cell suspensions were placed in the phantom and irradiated at the High Flux Reactor (HFR) in Petten [Huiskamp, 1992]. The fraction of cells surviving the irradiation was measured, giving an indication for the radiation sensitivity of the cell suspension. Important quantities for the analysis of the experiments are the neutron spectra, and neutron and photon dose rates at the irradiation positions. The calculation of these quantities at the different irradiation positions in the phantoms, is described in this chapter. The calculations have been performed with the two dimensional transport code DORT [Rhoades, 1986] and the Monte Carlo code MCNP [Briesmeister, 1993], and are verified with measurements. The effect of uncertainties in the input parameters of the calculations are investigated in a sensitivity study.

6.1 Experimental situation

The Bremen phantom (see figure 6.1) is a cylinder made from perspex and filled with water. The phantom has a diameter of 16 cm and a length of 23 cm, with a wall thickness of 0.8 cm. In the phantom, a perspex sample holder is placed to position the small vials with cell suspensions. In some cases a certain amount of ^{10}B is added to the suspensions in the vials to investigate the effect of the $^{10}\text{B}(n,\alpha)^7\text{Li}$ reaction on the cell survival during irradiation. The concentration of boron varies from 0 to 45 ppm. The phantom was irradiated at the neutron facility for BNCT, the HB11 facility, at the High Flux Reactor (HFR) in Petten. Although different collimator sizes are possible, all irradiations were performed using the 8 cm collimator.

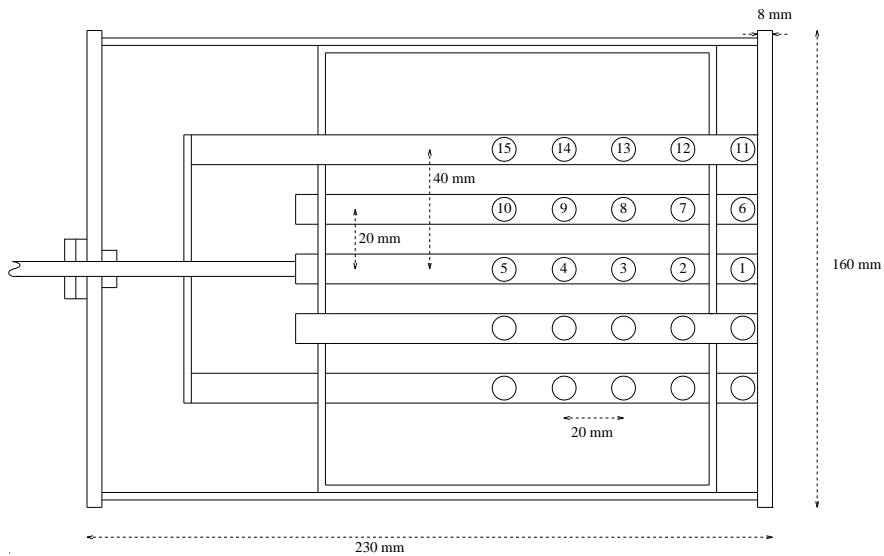


Figure 6.1: Schematic view of the Bremen phantom. In the circles, small vials with cell suspensions can be fixed for irradiation. The numbers label the positions with different neutron spectra. The neutron beam enters the phantom from the right side.

By placing the vials at different radial and axial positions inside the phantom, the influence of changing spectral characteristics can be considered. In the phantom 45 positions are present to place vials, but due to symmetry, 15 different spectral characteristics need only be considered. These positions are numbered in the figure 6.1.

6.2 Description of the calculations

6.2.1 Beam characteristics

The calculations are based on the neutron beam characteristics of the HB11 facility as calculated with the computer code MCNP by Watkins [Watkins, 1995]. From earlier comparisons between the calculated neutron energy spectrum and the free beam spectral measurements, it is generally supposed that the fast part of the neutron beam is underestimated in the calculated neutron beam. Also some questions must be solved about the beam divergence. Some adaptations to the spectrum have already been made but more calculations to solve these discrepancies will be performed by others in the future. Therefore the calculations in this study are based on the best known spectrum. The effect of uncertainties in the spectrum will be considered in a sensitivity study. The photon spectrum of the HB11 beam is presently unknown and in the phantom calculations only the photon dose induced by neutron capture is determined while an estimation is made for the incident photon dose, based on measured photon doses.

6.2.2 The DORT and MCNP model

The correctness of the calculated spectral characteristics of these deep penetration problems is important in the analysis of the radiobiological experiments. As only energy integrated quantities such as reaction rates can be measured, two different computer codes are used to determine the spectral characteristics: the deterministic code DORT and the Monte Carlo code MCNP. The codes calculate the neutron spectrum in entirely different approaches, hence a good agreement between the calculations gives enough confidence to use the spectra in the analysis of the experiments. Variations

in the total fluence rate of the beam can occur for example due to changes in the configuration of the reactor core, burn-up of the fuel elements and the exchange of experiments around the core. Therefore, all calculated quantities are relative and are normalised to measurements.

DORT is a two dimensional code, the phantom is modelled in a R-Z geometry using an appropriate mesh (distances between mesh points are between 2 and 4 mm). The neutron beam is modelled as a boundary source with a beam divergence of 8 degrees, using a quadrature set based on the S_8 expansion. In the S_8 expansion, 48 discrete directions are used, equally distributed in space. However, the neutron beam, modelled as a fixed source, has a strong direction dependence, hence a normal S_8 expansion is really not sufficient for this problem. Nevertheless, to model the forward peaking neutron beam with a divergence of 8 degrees, a so-called upwards biased quadrature set, based on the S_8 expansion is used. In this set the same directions as in the S_8 expansion are modelled as well as 52 extra directions equally distributed within a cone of 20 degrees. The distance between the beam aperture and the phantom is 6 cm. Deterministic codes, however, poorly model the neutron transport in materials with low scatter densities, therefore the boundary source is set on top of the phantom to avoid neutron transport through air. Furthermore, as compensation, the beam diameter is increased according to a more extended penumbra.

The calculations were performed using the EIJ2-XMAS library (based on the JEF2.2 evaluated data file) [van der Stad, 1995] or the BUGLE-80 library [Roussin, 1980]. The EIJ2-XMAS library has 172 neutron energy groups, and 78 neutron upscatter groups. In the calculations, 21 upscatter groups are used, which is adequate for this problem. The library contains only cross sections for neutron transport. The data for photon transport or to calculate KERMA's are not provided. For the calculation of the photon and neutron KERMA's, the BUGLE-80 library is used. This library is collapsed from the VITAMIN C library based on ENDF/B IV, containing 47 neutron energy groups of which two thermal groups are below 0.4 eV and 20 photon groups. In the BUGLE-80 library only a limited number of nuclides is available. As the calculated neutron beam spectrum has a different energy structure than those used in the cross section libraries, the

beam spectrum is converted into the library structures [Freudenreich, 1996]. In figure 6.2 the original beam spectrum (calculated with MCNP) and the spectra in the energy structure of the cross section libraries are shown.

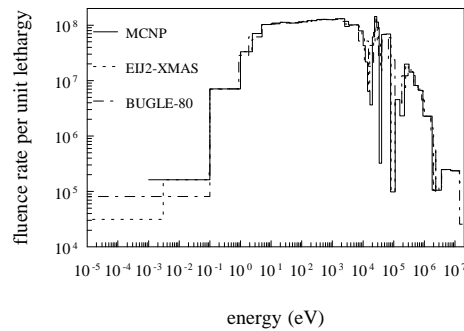


Figure 6.2: Original beam spectrum [Watkins, 1995] calculated with the MCNP code and the neutron beam spectra used in the phantom calculations in an energy structure specified for the EIJ2-XMAS library and the BUGLE-80 library.

In the MCNP calculations, the incident neutron beam is also given as a fixed boundary source. The distance between source and phantom in the model is 6 cm. The calculations are based on the continuous energy cross section library EJ2-MCNPlib [Hogenbirk, 1995], based on the JEF2.2 evaluated data file. For easy comparison of the two codes, the neutron spectra were calculated in the BUGLE-80 and EIJ2-XMAS energy structures.

6.3 Description of the methods of the measurements

The dosimetry was performed using activation foils [Paardekooper, 1992] and ionisation chambers [Raaijmakers, 1995]. Three kind of foils are used: a MnNi foil monitoring the $^{55}\text{Mn}(n,\gamma)^{56}\text{Mn}$ capture reaction, a Cu foil measuring the $^{63}\text{Cu}(n,\gamma)^{64}\text{Cu}$ reaction and a AuAl foil to measure the $^{197}\text{Au}(n,\gamma)^{198}\text{Au}$ capture reaction. The sensitive energy ranges for all three dosimeters are between 0.01 eV and 0.1 keV. Due to the low fast fluence rate in the phantom it is not possible to use foils sensitive to higher ener-

gies. The foils were irradiated at the different positions in the cylindrical phantom, the experimental uncertainty is approximately 3%.

Ionisation chambers were used to determine the neutron and the photon dose rates. These chambers measure the total of the neutron dose (coming from recoiling protons), the photon dose and the response caused by thermal neutron interactions with the detector. Calibration measurements are performed to determine the sensitivity of the detector for the different sources. Due to the complexity to determine these correction factors in mixed beams, the measured doses have relatively large uncertainties. An extra uncertainty is added to the measurements due to geometrical limitations. The cylindrical phantom is closed on all sides, while ionisation chambers need a direct connection to the measuring equipment. Nevertheless, to obtain an estimation of the dose rates from proton recoil and from photons, measurements in the same beam with two cubic phantoms filled with water (sides resp. 15 and 30 cm) were used [Raaijmakers, 1995]. By examination of these results, a reasonable estimation of the dose rates in the phantom can be made. Uncertainties in the measurements of the neutron doses are 25% while the photon measurements have an uncertainty of 15%.

6.4 Comparison of measured and calculated reaction rates

A first verification of the calculations was performed by comparing calculated and measured reaction rates. At each of the 15 irradiation positions in the phantom, a set of three activation foils were irradiated. Each set contained a MnNi, Cu and AuAl foil, monitoring the reactions mentioned in section 6.3. The normalisation of the calculated reaction rates was performed using the mean ratio between the unnormalised calculated reaction rates of the $^{55}\text{Mn}(n,\gamma)$ capture reaction and the measured ones for positions 1 to 10. These positions are in the middle of the beam and therefore relatively insensitive to any anisotropy of the neutron beam, while the other points, on the edge of the beam, may have a greater dependency on the uncertainties in the beam anisotropy.

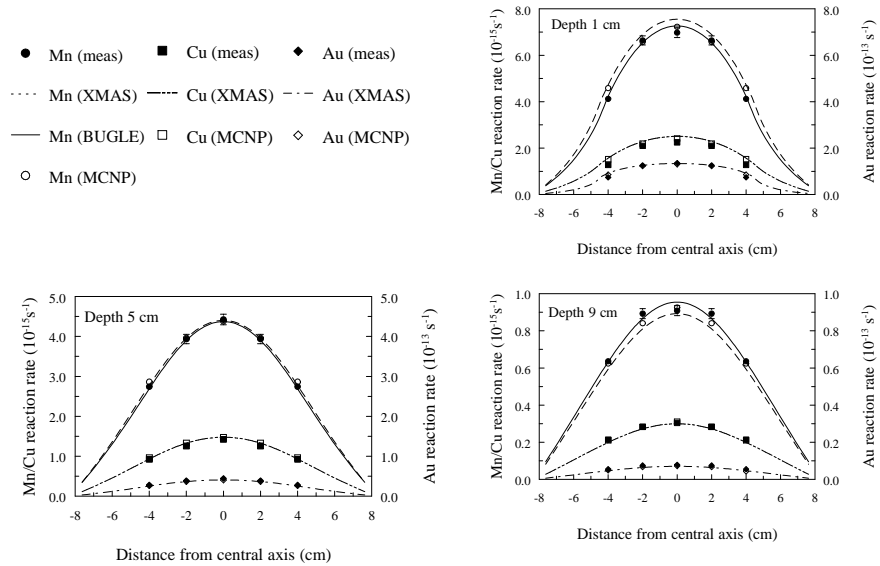


Figure 6.3: Comparisons between measurements and calculations of the Mn, Cu and Au reaction rates at four different depths in the phantom. DORT calculations are based on the EIJ2-XMAS or BUGLE-80 library. The MCNP calculations are based on the EJ2-MCNPlib library.

The DORT calculations were performed with the BUGLE-80 library as well as the EIJ2-XMAS library. Using the BUGLE-80 library, only the manganese capture reaction can be considered because of a lack of cross section data for the two other foil materials. The EIJ2-XMAS Library contains all the necessary information to calculate all three reaction rates. The results from measurements and calculations are shown in figure 6.3 for three different depths in the phantom. All calculations give a reasonable agreement with the measured reaction rates. The relative differences between calculations and measurements, defined as the difference between measured and calculated reaction rate divided by the measured reaction rate, are

- for the DORT calculation using the BUGLE-80 library between -5% and 4%,
- for the DORT calculation using the EIJ2-XMAS library between -8% and 10%, and

- for the MCNP calculation using the EJ2-MCNPlib library between -5% and 6%.

Apparently, the better treatment of the upscatter data in the EIJ2-XMAS library as well as the larger number of thermal groups compared with the BUGLE-80 library, did not lead to a better agreement between measurements and calculations. Also the continuous cross section library EJ2-MCNPlib, used in the MCNP calculations, has a comparable agreement with the DORT calculations based on the BUGLE-80 library.

6.5 Comparison with ionisation chamber measurements

To consider the neutrons with high energy and the photons, the calculated dose rates are compared with measured dose rates. The measurements were performed in cubic phantoms filled with water and then converted to the situation of the cylindrical phantom [Raaijmakers, 1995]. The incident photon spectral characteristics are unknown, and therefore the dose distribution in the phantom from this beam component cannot be calculated. Based on measurements, it is assumed that positions 1 to 10 receive an incident photon dose rate of 1.0 Gy/h, while the other positions get a dose rate of 0.5 Gy/h (beam edge).

In tables 6.1 and 6.2 the measured and calculated dose rates are listed. The calculated proton recoil dose is much too low for all positions. The earlier-mentioned expectation that the calculated fast and epithermal fluence rate of the neutron beam is too low has been confirmed. Neutrons with a high energy have a larger penetration depth than low energy neutrons. Hence, an underestimation of these high energy neutrons causes a too few neutrons at depth. The underestimation increases with depth. In tables 6.1 and 6.2 this tendency is evident by the increasing difference in calculated and measured proton recoil dose. For the photon dose rate calculations, the assumption that the incident photon dose rate is constant for all irradiation positions and equal to 1 Gy/h for positions directly in the beam and 0.5 Gy/h for the positions at the edge of the beam, is very reasonable. Differences between calculations and measurements are relatively small compared to the uncertainties in the measurements.

Table 6.1: Comparison of measured and calculated dose rates for proton recoil reactions (Gy/h), the calculations are based on the BUGLE-80 library

position	measured ^a	calculated	difference ^b
1	1.22	0.65	-47%
2	0.56	0.25	-55%
3	0.27	0.10	-60%
4	0.15	0.052	-65%
5	0.13	0.028	-79%
6	1.12	0.65	-42%
7	0.52	0.25	-52%
8	0.25	0.11	-58%
9	0.14	0.049	-65%
10	0.12	0.027	-78%
11	0.64	0.58	-10%
12	0.30	0.18	-40%
13	0.14	0.065	-53%
14	0.080	0.030	-62%
15	0.070	0.016	-77%

^a) uncertainty in proton recoil measurements is approx. 25% (one standard deviation)

^b) rel. difference = $\frac{\text{calculated}-\text{measured}}{\text{measured}} \cdot 100\%$

Table 6.2: Comparison of measured and calculated dose rates for the photons [Gy/h], the calculations are based on the BUGLE-80 library

position	measured ^a	calculated ^b	incident dose ^c	difference ^d
1	2.0	1.3	1.00	15%
2	2.2	1.5	1.00	16%
3	1.9	1.1	1.00	11%
4	1.6	0.76	1.00	8%
5	1.4	0.46	1.00	8%
6	1.9	1.2	1.00	14%
7	2.0	1.3	1.00	17%
8	1.8	1.1	1.00	11%
9	1.6	0.70	1.00	9%
10	1.3	0.43	1.00	12%
11	1.3	0.86	0.50	5%
12	1.4	1.0	0.50	9%
13	1.2	0.81	0.50	5%
14	1.1	0.55	0.50	1%
15	0.87	0.36	0.50	-1%

^a) uncertainty in photon measurements is approx. 15% (one standard deviation)

^b) generated by the (n,γ) reactions in the phantom

^c) estimate of the free beam γ-ray component

^d) rel. difference = $\frac{\text{calculated}-\text{measured}}{\text{measured}} \cdot 100\%$

6.6 Comparison of calculated neutron spectra

The neutron spectra calculated with the DORT code were compared with the calculated spectra from the MCNP code. The MCNP calculations are based on continuous cross sections, hence the spectra can be obtained in all possible energy structures. For an easy comparison of the calculations, the neutron fluence rates are calculated in the energy structure of the BUGLE-80 library as well as the EIJ2-XMAS library energy structure. The spectra are calculated for all positions but only the spectra at position 1 and 15 are shown in this comparison and in the sensitivity study. The spectrum at position 1 contains most fast neutrons (hard spectrum) of all positions while position 15, at the greatest distance from the neutron source, has the lowest number of fast neutrons (soft spectrum).

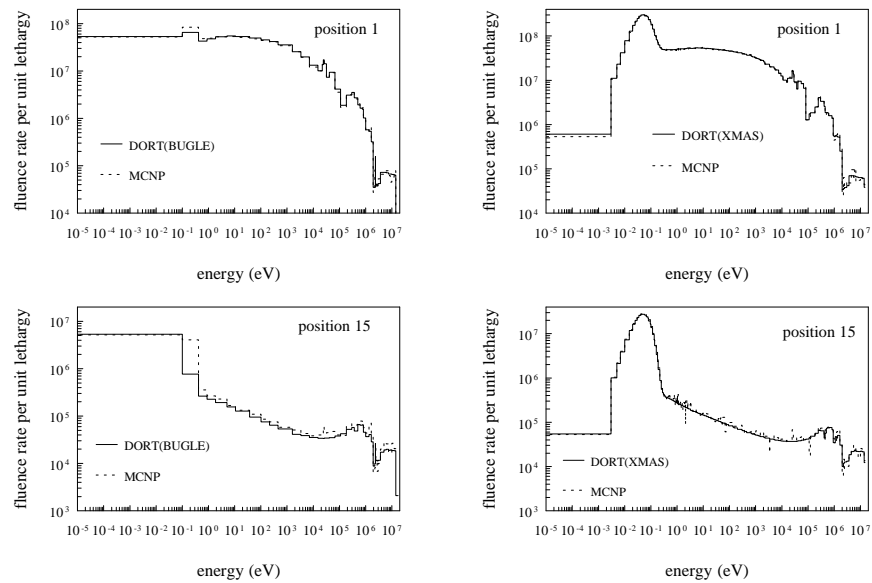


Figure 6.4: Calculated neutron spectra with DORT (based on the BUGLE-80 or EIJ2-XMAS) and MCNP (EIJ2MCNPlib) using the energy structure of BUGLE-80 (left) and EIJ2-XMAS libraries (right)

In figure 6.4, the spectra are shown. In spite of the high number of particles simulated by the MCNP code (100 million), a large uncertainty (larger

than 20%) still exists in the fast neutron spectrum. This uncertainty is large because only a small fraction of the simulated neutrons with a high energy, and still having a high energy, reach the irradiation positions. The differences in the calculated spectra are small.

6.7 Differences in computation time for the different codes and libraries

The results of the MCNP code and the DORT code using the EIJ2-XMAS library or the BUGLE-80 library are comparable. But the computation time needed to get these results can change considerably. In this section, a comparison has been made between the computation time needed for the different calculations to get reasonable results. The results are shown in tables 6.3 and 6.4.

Table 6.3: Comparison of the computation time needed for different number of energy groups using the DORT code with the EIJ2-XMAS library (all calculations are performed on a DEC-Alpha 3500, 150 MHz)

number of energy groups	41	45	172	172
number of therm. groups	4	8	78	78
number of upscatter groups	3	5	0	21
number of outer iterations	27	71	4	235
cpu (minutes)	82.8	232.9	140	4576
relative difference from measurements				
min	-10%	-6%	-110%	-8%
max	5%	4%	52%	10%

The DORT calculations based on the BUGLE-80 library needed the lowest, and acceptable, computation time: after four iterations or 29.3 minutes on a DEC-Alpha 3500 (150 MHz), the calculation converged. The EIJ2-XMAS

Table 6.4: Comparison of computation time needed by the different codes or cross section libraries.

code library	DORT BUGLE-80 ^a	MCNP ^b MCNPlib
number of energy groups	47	-
number of therm. groups	5	-
number of upscatter groups	0	-
number of outer iterations	4	-
cpu (min)	29.3	11340
relative difference from measurements		
min	-5%	-5%
max	4%	6%

^a) The BUGLE-80 library has no upscatter groups. This is compensated in the absorption and scattering cross sections

^b) The EJ2-MCNPlib is a continuous energy cross section library

library using the original energy structure and taking into account the upscatter groups, needed more than 3 days of computation time to converge. Omitting the upscatter groups gave a considerable reduction in computation time but the results obtained were inaccurate (as expected). Evidently, the computation time is mainly needed to converge the results in the energy groups with upscatter. Upscatter information is only important for energy groups below 3 eV. A reduction of the number of energy groups above this energy level, leads only to a small reduction of computation time. Much more effective is a reduction of the energy groups below this limit. If the EIJ2-XMAS library is collapsed into a similar energy structure as the BUGLE-80 library, resulting in 41 energy groups and 3 upscatter groups, the computation time is still a factor 3 higher than for the BUGLE-80 library. The most important reason for using the EIJ2- XMAS library in this problem was the advantage of the better thermal energy structure of the EIJ2-XMAS library. By collapsing this group to a Small number of

thermal energy groups, this advantage disappeared.

The MCNP calculations are based on a continuous energy cross section library. Advantage of a continuous energy cross section library above a group cross section library is that resonances in the cross section are better treated. This can be an advantage for the calculation of the reaction rates described in section 6.4. But as has been shown, the results of the DORT calculations are comparable to the results of MCNP. It can be concluded that for this type of problem, the influence of the resonances is negligible and that a continuous energy cross section library is not necessary to obtain good results. The MCNP code can also use a group cross section library which would lead to a considerable reduction of computation time.

6.8 Sensitivity analysis

Due to the uncertainties in the calculated neutron beam parameters, the influence on the phantom calculations of variations in two important properties of the beam free in air are considered in a sensitivity study. These parameters are the fast neutron fluence rate and the anisotropy of the beam intensity. In addition, the influence of the boron atoms in the vials on the neutron spectra at the irradiation positions is considered. Also due to the statistical uncertainties in Monte Carlo calculations which makes comparison of small changes in spectra difficult as well as the (relatively) long computation time needed for MCNP runs, all calculations in the sensitivity analysis were performed with the DORT code. The BUGLE-80 library is preferred above the EIJ2-XMAS library because of the time consuming process of upscatter.

6.8.1 Effect of increasing the beam intensity above certain energy thresholds

Based on earlier comparisons between the free beam spectral measurements and the calculated neutron energy spectrum, the suggestion was raised that the high energy (fast) part of the calculated beam spectrum is too low. Therefore, the proportionality between the fast fluence rate and the thermal

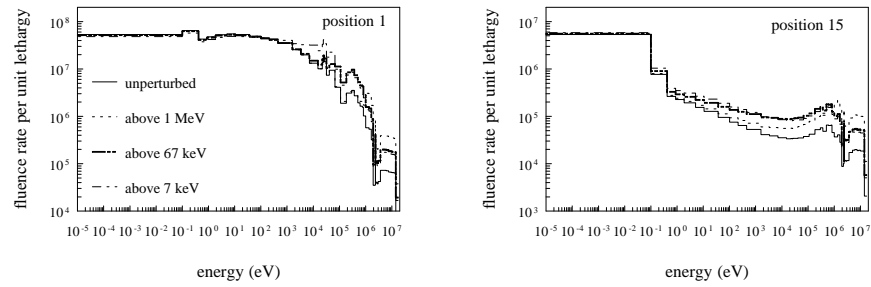


Figure 6.5: Effect of perturbations in neutron beam intensity on neutron energy spectra inside the phantom (DORT calculations based on the BUGLE-80 library).

fluence rate was changed by increasing the intensity of the beam above three arbitrary chosen energy boundaries. The factors by which the fast spectrum was multiplied was chosen in such a way that the mean relative differences between measured and calculated reaction rates are small (within 5%). In the first perturbation the spectrum above 1 MeV is multiplied with a factor 5.4. In the second perturbation, the spectrum above the 67 keV is increased by a factor 2.9. The third and last perturbation was made to all energy groups above 7 keV, this time with a factor 3.1. Again all calculations were normalised on the measured $^{55}\text{Mn}(n,\gamma)^{56}\text{Mn}$ reaction rates for the first 10 positions.

In figure 6.5 the perturbed and unperturbed spectra are shown at two positions in the phantom, viz. position 1 and 15. Using a higher fast incident neutron beam intensity, the fast part of the spectra changes up to a factor 5 while the thermal part differs only a few percent. Due to these small changes in the thermal part the manganese response changes only a little (see figure 6.6). The effect on the proton recoil, originating from fast and epithermal neutrons, is large. All perturbed spectra give a better result than the unperturbed spectra. The best fit is obtained from the first perturbation: an increase of intensity above 1 MeV. The other two show a faster decrease of the recoil dose going into the phantom than the measurements, but are still better than the unperturbed calculated doses. Therefore, it is apparent that the intensity of the calculated fast neutron fluence rate of the free beam is too low, as indicated clearly by the increase of the fluence rates above 1

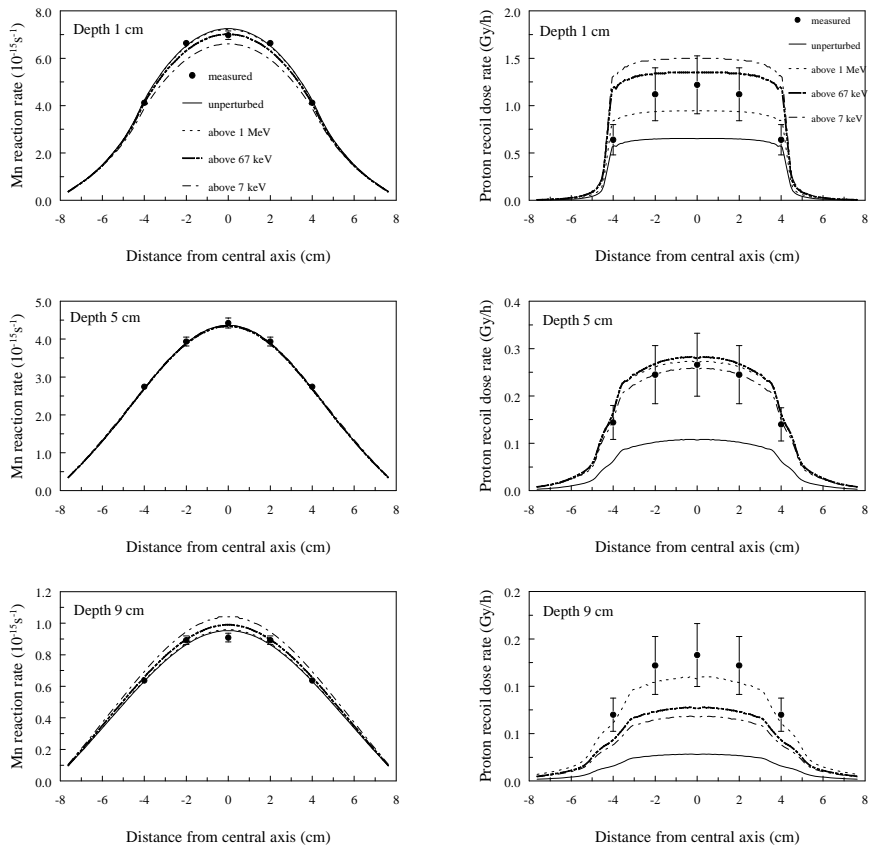


Figure 6.6: Effect of perturbations in the spectrum of the neutron beam on various profiles inside the phantom (DORT calculations based on the BUGLE-80 library)

MeV. However, because of the arbitrary energy limits of the perturbation and the constant factor used to increase intensity no conclusion about the correct shape of the beam spectrum can be drawn.

6.8.2 Anisotropy of beam intensity

Besides the uncertainties in the high energetic part of the neutron beam, large uncertainties also exist about the angular distribution of the beam. In

the previous calculations, a beam divergence of 8 degrees was used. To consider the influence of this parameter, two other angular distributions were considered: a distribution of 18 degrees and one of 30 degrees. The angular source distribution and positions of the incident beam have been taken equal for all energy groups. In reality, the angular source distribution changes with the neutron energy but for this study a uniform distribution over all energy groups is considered sufficient. In figure 6.8, the new calculations are compared with the unperturbed (i.e. 8 degrees) calculation and the measured data. Again, the calculations are normalised to the manganese foils.

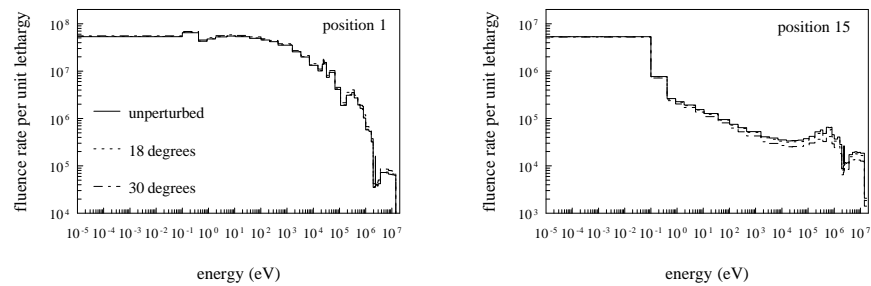


Figure 6.7: Local spectra for angular perturbed neutron beam (DORT calculations based on the BUGLE-80 library).

The effect on the neutron spectra of increasing the beam angle is rather small when normalised, as is the case here. Only in the high energy part small deviations are seen. In figure 6.7, the spectra are shown for two extreme irradiation positions. The differences in the thermal fluence rate are small. Also, the changes are small in the calculated manganese reaction rates (see figure 6.8). The effect on the thermal neutron fluence rate of an increasing beam angle can therefore be neglected. The proton recoil dose rate, however, and therefore the fast part of the spectrum is somewhat more dependent on the beam divergence but is negligible compared with the uncertainties in the fast neutron beam. Only for very large distortions in the beam divergence, a clear difference exists in the shape of the spectra. This is totally different for absolute calculations. In this case, the total fluence rates on the irradiation positions are changing considerably with small changes

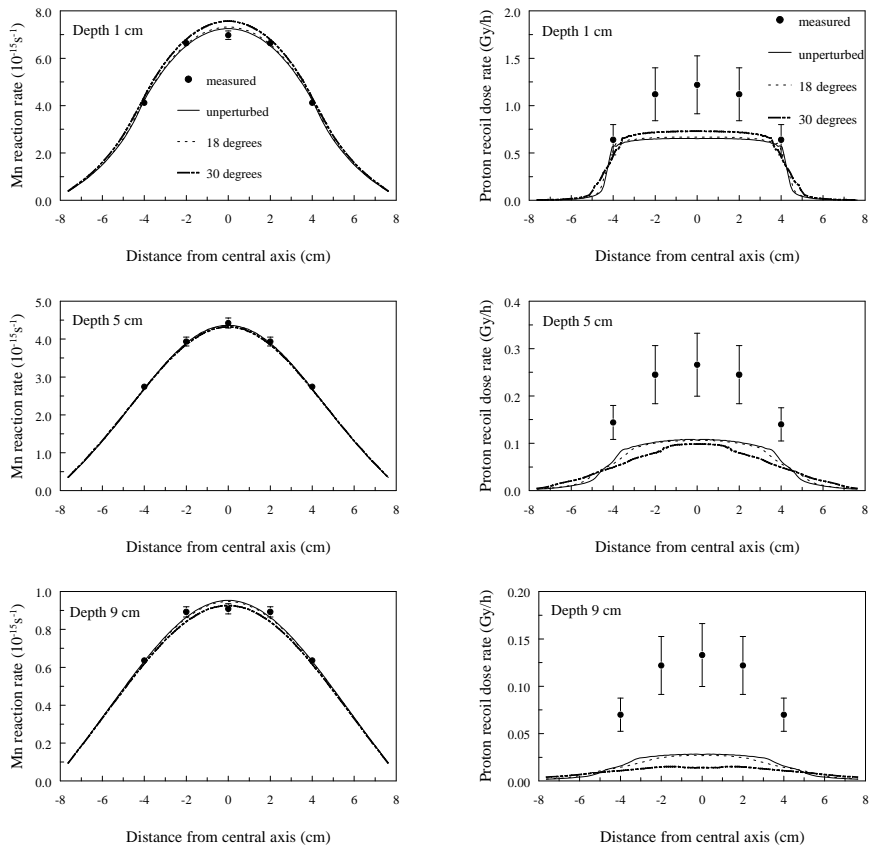


Figure 6.8: Effect of perturbations in the anisotropy of the neutron beam on various profiles inside the phantom (DORT calculations based on the BUGLE-80 library).

in the divergence. The conclusion can be drawn that the modelling of the anisotropy of the beam can be maintained at about 8 degrees.

6.8.3 Boron in suspensions

In all calculations, the whole phantom is filled with water only. However, during cell irradiations, a certain amount of ^{10}B can be added to the small vials containing the cell suspensions. The effect of these boron additions

as a drain of thermal neutrons were considered by calculating the neutron spectra in case of a boron amount of 45 ppm in the vials. The effect of the boron atoms on the calculated manganese reaction rates and proton recoil dose rates is less than 1%. For such low amounts the boron atoms in the vials can be neglected.

Chapter 7

Conclusions about the phantom calculations

An important part of the pre-clinical studies within the BNCT project is the determination of the effects of mixed field irradiations. One frequently used method is based on monitoring the biological effect of the mixed field irradiations on cell-cultures. Such a study has been performed at the HB11 beam [Huiskamp, 1992]. In the analysis of the biological effect the spectral characteristics are important. These characteristics have been determined here using the deterministic computer code DORT together with the BUGLE-80 library calculating neutron spectra, photon and proton recoil dose rates and manganese reaction rates, or using the EIJ2-XMAS library calculating neutron spectra and different reaction rates. The calculations have been normalised to the mean ratio between calculated $^{55}\text{Mn}(n,\gamma)^{56}\text{Mn}$ reaction rates and the measured ones for the irradiation positions in the beam (within 2 cm from beam centre line), excluding the positions with relatively large influence of the uncertainties in the anisotropy of the beam intensity.

The validation of the calculations has been based on measurements, using neutron activation monitors [Paardekooper, 1992] and ionisation chambers [Raaijmakers, 1995]. The activation foils were irradiated in the cylindrical phantom to monitor the thermal part of the neutron spectrum. Three types were irradiated, resulting in the reaction rates of the following reactions: the $^{55}\text{Mn}(n,\gamma)^{56}\text{Mn}$, $^{63}\text{Cu}(n,\gamma)^{64}\text{Cu}$, and $^{197}\text{Au}(n,\gamma)^{198}\text{Au}$ capture reactions. The BUGLE-80 cross section library contains only a limited number of nuclides, and therefore only the manganese reaction rate could be calculated. The measured manganese reaction rates and the calculated ones have a good conformity using the BUGLE-80 library or the EIJ2-XMAS library. For all irradiation positions, the difference is below 5% (using BUGLE-80) and 10% (using EIJ2-XMAS), which is a very good agreement between the calculations and the measurements.

Ionisation chambers were used for the verification of the fast neutron spectrum and the photon dose rates. Due to geometrical restrictions, these measurements were performed in a cubic phantom, also filled with water, and the results converted for the situation considered here. This conversion and the complexity of the measurements result in large uncertainties of the measurements (15% for the photons and 25% for the proton recoil measurements). In spite of these large uncertainties, the measurements give a reasonable indication of the dose rates at the irradiation positions. The calculated proton recoil dose rate has a mean difference of 50%. This discrepancy is most likely caused by an underestimation of the fast fluence rate of the incident neutron beam. The incident photon beam spectrum is unknown, only the (energy integrated) dose rate is measured in a free beam measurement. This free beam dose rate is considered as the incident photon dose rate, assuming that the dose rate does not decrease over the irradiation positions. At 4 cm radial distance from the beam centre line, the dose rate is taken to be half the measured dose rate on the beam centre line, to take into account that these positions are not in the direct beam. Using this assumption, the differences between measurements and calculations are very reasonable. The calculated dose rates are slightly too high, but the maximum difference is 17% and is approximately equal to the standard deviation of the measurements.

The above used quantities are all energy integrated. To gain more confidence into the shape of the calculated neutron spectra, the calculated spectra were compared with spectra calculated using another computer code, namely the Monte Carlo code MCNP. The disadvantage of this code are the statistical uncertainties. Even when using an extreme number of simulated particles (i.e. 100 million), the uncertainties for the high energetic part of the spectra are still above 20%. The DORT calculated spectra are very much comparable with the MCNP spectra, giving enough confidence in these spectra to use them as input for the microdosimetry model.

An advantage of using the EIJ2-XMAS library is the finer thermal energy structure used to describe the thermal spectrum, which is much more advanced than in the BUGLE-80 library, and the presence of data for all the types of foils used. The lack of photon data or KERMA factors means that the EIJ2-XMAS library can only be used for problems in which only the neutron fluence rates are important. This is clearly not true for BNCT, in which the damage from unwanted neutrons and photons is an equally important parameter to determine. Using the two-dimensional transport code DORT, another draw-back for the EIJ2-XMAS library appears. While the BUGLE-80 library takes into account the upscatter of neutrons by changing the scatter and absorption cross section, the EIJ2-XMAS library stores this information explicitly. In doing this, the upscatter information is included using several upscatter groups. Although DORT is capable to treat upscatter groups, the algorithm becomes too time-consuming. Even if the library is reduced to the same number of energy groups as the BUGLE library, the calculation time is still a factor of 3 higher. Statistical uncertainties, even with an extreme amount of sampled particles (viz. 100 million), make the results of the MCNP code useless for this problem. Therefore, in the analysis of the biological experiments, presented later in chapter 12, the neutron spectra calculated with the deterministic code DORT, using the BUGLE-80 library are used.

All calculations are based on a calculated neutron source spectrum. Earlier comparisons of measurements and calculations have shown a discrepancy and have led to an adjustment of the fast part of the spectrum. In the performed comparison of the proton recoil dose rate, it seems that the fast

part is still underestimated. To investigate the effect of an underestimated fast neutron beam intensity a sensitivity study was performed. For three arbitrary energy levels the fast part of the spectrum was increased by a constant factor. This factor was chosen such that the mean difference for the proton recoil dose rate over the irradiation positions is below 5%. For all three cases, much better agreements between measurements and calculations were obtained than with the unperturbed spectra. However for the change in spectra above 7 keV or 67 keV, the calculated values decreased too fast with depth compared with the measured ones. For an increase of the spectrum above 1 MeV, the results are almost similar to the measurements: all are within 1 standard deviation of the measurements. Due to the arbitrarily chosen energy levels above which the neutron spectra are changed, the correct shape of the incident neutron beam cannot be obtained by the study.

Another parameter with a large uncertainty is the anisotropy of the neutron beam. This anisotropy is energy dependent. For reasons of simplicity, it is generally assumed to be constant. In case of relative calculations, the influence of the beam divergence is rather small, as shown in the sensitivity study. From the geometry of the beam facility, the beam divergence is expected to be around 8 degrees. Only when introducing a significantly large increase of this divergence, the neutron spectra change for high energies. The effect on the thermal fluence rates is very small. Comparing with the uncertainties in the shape of the incident beam, uncertainties in the anisotropy are negligible. Note that for absolute calculations (no normalisation on measurements), the result is totally different. In this case, the results change considerably, with small changes in the beam divergence.

References

Briesmeister, J.F. (1993), 'MCNP, A general Monte Carlo code for neutron and photon transport, version 4A,' *Los Alamos Report LA-12625*.

Freudenreich, W.E.F. (1996), private communication, Netherlands Energy Research Foundation (ECN), Petten, The Netherlands.

Hogenbirk, A. (1995), 'EJ2-MCNPlib, Contents of the JEF-2.2 based neutron cross-section library for MCNP4,' *ECN report ECN-I-95-017*, Petten, The Netherlands.

Huiskamp, R., Begg, A.C., Gregoire, V.G.A., Verrijk, R., Gabel, D., Siefert, A., and Moss, R.L. (1992), 'Radiobiology studies at Petten: Status on cell culture, mice and dog experiments,' in *Progress in Neutron Capture Therapy for Cancer*, Editors B.J. Allen *et al*, Plenum Press, New York.

Moss, R.L. (1992), 'Current overview on the approach of clinical trials at Petten,' in *Boron Neutron Capture Therapy*, Editors: D. Gabel and R. Moss, Plenum Press, New York.

De Leege, P.F.A., and Bos, A.J.J. (1996), private communication, IRI, Technical University Delft, The Netherlands.

Paardekooper, A., Kraakman, R., and Voorbraak, W.P. (1992), 'Cell irradiations in air and cylindrical phantom at HB11,' *ECN report NFA-Metro-92-13*, Petten, the Netherlands.

Raaijmakers, C.P.J. (1995), private communication, Dutch Cancer Institute, Amsterdam, The Netherlands.

Roussin, R.W. (1980), 'BUGLE-80, Coupled 47 neutron, 20 gamma ray, P3, cross section library for LWR shielding calculations by the ANS 6.1.2 working

group on multigroup cross sections,' *Oak ridge report DLC75*, Oak Ridge National Laboratory.

Rhoades, W.A., and Childs, R.L. (1986), 'An Updated Version of the DOT 4 one and two Dimensional Neutron/Photon Transport Code,' *Report: LA-7396-M, Revision 2*, Los Alamos.

Van de Stad, R.C.L., De Leege P.F.A., and J. Oppe (1996), 'EIJ2-XMAS, contents of the JEF2.2 based neutron cross section library in the XMAS group structure,' *ECN report: ECN-CX-95-087*, Petten, the Netherlands.

Watkins, P.R.D., Konijnenberg, M., Constantine, G., Rief, H., Ricchena, R., De Haas, J.B.M, and Freudenreich, W.E. (1992), 'Review of Physics calculations performed for the BNCT facility at the HFR Petten,' *Boron Neutron Capture Therapy*, Editors: D. Gabel and R. Moss, Plenum Press, New York.

Watkins, P.R.D. (1995), private communication, Joint Research Centre, Petten, The Netherlands.

Nomenclature

List of abbreviations

DORT	two-Dimensional discrete ORdinates Transport code
EIJ2-XMAS	ECN/IRI JEF2 library in the XMAS group structure
EJ2-MCNPlib	ECN JEF2 library for MCNP calculations
JEF2.2	Joint Evaluated File version 2.2
HB11	Horizontal Beam channel number 11
HFR	High Flux Reactor
KERMA	Kinetic Energy Released in MAtter
MCNP	Monte Carlo Neutron and Photon transport code system

Part III

Microdosimetry

Chapter 8

Introduction to the microdosimetry model

Many biological effects of radiation are dependent upon the spatial distribution of microscopic energy deposition. In Boron Neutron Capture Therapy (BNCT) [Barth, 1990],[Slatkin, 1991], the spatial distribution is rather complex. It varies only slightly over the irradiated volume for the photon component, because of its penetration depth and the homogeneous distribution of the hydrogen, and also, only slightly for the nitrogen component, because of the homogeneous distribution of nitrogen. However, the variation is very significant for the important ^{10}B and proton recoil components. Variations in the ^{10}B component are mainly attributed to microscopic concentration distributions that may be remarkably different from cell to cell, tissue to tissue and from boron compound to boron compound. The variation for proton recoil is caused mainly by variation in the spectral characteristics of the used beam and by the significant change in spectral characteristics versus depth and lateral penetration in tissue.

Several theoretical models have been developed to calculate the energy de-

position or derived quantities on a cellular level [Gabel, 1987], [Kitao, 1975], [Kobayashi, 1982], [Wheeler, 1990], [Charlton, 1991], [Solares, 1992], [Verrijk, 1994]. Monte Carlo techniques are preferred because of the easy inclusion of physical mechanisms. The published models have a wide variety of physical mechanisms included in their models, and are appropriate for the capture reactions resulting in high-LET irradiation (mostly the boron and nitrogen capture reaction). With these models radiation parameters can be calculated for selected concentration distributions of key nuclides, cellular diameters, neutron beam characteristics and irradiation times. Most of the models also take into account radiation emerging from neighbouring cells by modelling an array of 3x3x3 cells with the central cell as the target cell. Some models even simulate natural variability in cellular dimensions by dynamically chosen cell and nucleus diameters. The calculated quantities differ from model to model but the most extended models calculate microscopic doses, (specific) energy imparted distributions, assuming that earlier hits have no influence on the effect of the considered hit (single event model) and the number of hits in the nucleus of a cell, considering this as the radiosensitive part of a cell. As mentioned earlier, the published models are limited to high-LET radiation from capture reactions. One group has published lineal energy distributions (energy imparted per unit length) for the boron reaction based on measurements [Amols, 1992], [Wuu, 1992].

Clinical trials for BNCT will be performed with epithermal neutron beams [Moss, 1992]. Although much effort is put into reducing the incident γ -rays, fast and thermal neutrons, the epithermal neutron beams used for brain tumour treatment are still a mixture of all neutron energies and γ -rays. An epithermal neutron beam will thermalise in the head of a patient, resulting in a tumour irradiation from principally thermal capture reactions. Before the beam is thermalised, the neutrons will interact with the hydrogen nuclei, present in high concentrations in tissue, leading to the recoiling protons. The dose from this interaction can be as high as 60% of the total biological effective dose delivered at the skin of the patient and will decrease with depth into the head. Much work has been done to experimentally determine Relative Biological Effect (RBE) values of the various beam components to be used in BNCT, but without consensus so far [Davis, 1970], [Gabel, 1987], [Fukuda, 1987], [Hiratsuka, 1991]. Several groups have tried to solve this

problem by using microdosimetry calculations. In these studies the spatial distribution of energy deposition of the boron and nitrogen capture reactions have been considered, while neglecting the significant variation of the spatial distribution of the proton recoil component. The RBE for recoil protons will vary significantly with a change in spectral characteristic, because of the strong exchange of the neutron energy to the tissue [Hall, 1975], [Alpen, 1992]. Microscopic calculation of the proton recoil contribution may solve the lack of consensus regarding the RBE for this reaction.

Due to the large influence of the proton recoil dose to the total biological effect in tissue, it was decided to develop a new microdosimetry model that includes the proton recoil and the high-LET irradiation from the capture reactions. In addition to the various special features in the published models this new model includes the track length distribution through the nucleus and the lineal energy distribution in the nucleus.

Little is known about the conversion of microdosimetry results for BNCT into the therapeutic effects. Wheeler et al. [Wheeler, 1990] have used the results to introduce compound factors in normal brain tissue and in brain tumours. Verrijck et al. [Verrijck, 1994] used so-called track individual efficacy factors for translation to a biological effect, Gabel [Gabel, 1984] and Bond et al. [Bond, 1985] have suggested that the microdosimetric spectra can be related to cell survival using a 'hit-size-effectiveness' function that gives the probability of a cell being killed as a function of the energy imparted. Based on the last suggestion, the effectiveness function is used for the translation of the calculated microscopic data into several radiobiological quantities. This function is presently not available in the literature. Instead of measuring this function directly, a method to derive these functions was developed in the present work. This method is based on measured cell surviving fractions and the calculated spectra from the microdosimetry model.

The effectiveness function, describing the relation between the energy deposition in the nucleus and the probability that a cell is killed, will differ for different types of cells but the deduction will be the same for all cell types. As an example, the effectiveness function for a single cell culture, viz. the Chinese hamster cells (V79 cells), is deduced. Therefore, results from an

extensive radiobiological experiment at the HFR are used as input for the model. In this experiment [Huiskamp, 1995] the single cell suspensions are irradiated in small vials, which are placed in the so called Bremen phantom (see section 6.1). The spectral characteristics at the irradiation positions were calculated in part II.

Once the effectiveness function is derived for a certain cell type, this function can be used to obtain the RBE, microscopic boron concentration distributions, and cell surviving fractions. The theory to obtain these radiobiological quantities is explained based on the experiments with the V79 cells at the HFR.

Chapter 9

Structure of the microdosimetry model

To enable prediction of radiobiological quantities, all important nuclear reactions induced by neutrons and photons in the irradiated objects have to be considered. In this chapter, the different interactions are discussed as well as a global definition of the different parts in the model together with their relationships. In the following chapters, the different parts are considered in more detail.

9.1 Specific interactions of neutrons and photons in tissue

9.1.1 Capture reactions emitting charged particles

An important part of the energy deposition in tissue is generated by capture reactions in tissue resulting in the emission of charged particles. Important

for the tumour tissue, containing a considerable amount of boron atoms (several tens of ppm) is the ^{10}B capture reaction, but also in healthy tissue, a certain number of boron atoms is present. By the capture reaction, the nucleus ^{11}B is produced in an excited state, which is followed by emission of an α -particle and a ^7Li nucleus. This decay can follow two different modes [Ajzenberg-Selove, 1975]: in 93.7% of the events, an α -particle having an energy of 1.47 MeV with a range of $7.9\ \mu\text{m}$ in tissue (particle ranges derived from TRIM-88 [Biersack, 1970]), and a ^7Li ion having an energy of 0.84 MeV with a range of $4.2\ \mu\text{m}$ in tissue are emitted, as well as a photon having an energy of 0.48 MeV from the lithium nucleus. The other 6.3% of the events result in a 1.78 MeV α -particle with a range of $9.6\ \mu\text{m}$ and a 1.01 MeV ^7Li ion with a range of $4.7\ \mu\text{m}$. This capture reaction has a large probability for neutrons with low energies, the thermal cross section is 3837 barn (2200 m/s cross section).

Nitrogen, present in large amounts in the tumour and in healthy tissue, absorbs neutrons as well, resulting in the capture reaction: $^{14}\text{N}(\text{n},\text{p})^{14}\text{C}$. The protons and the carbon ions are emitted with an initial energy of 0.59 MeV and 40 keV with a track length of $10.9\ \mu\text{m}$ and $0.3\ \mu\text{m}$ respectively. This reaction is also a thermal reaction and has a 2200 m/s cross section of 1.81 barn. The nitrogen concentration for tissue is approximately 2 wt.%.

9.1.2 Photons

Thermal neutrons can also easily be captured in hydrogen through the reaction $^1\text{H}(\text{n},\gamma)^2\text{H}$ with a thermal cross section of 0.332 barn. A 2.22 MeV photon is emitted with each capture. Although the cross section is relatively small compared with the cross section of the above mentioned capture reactions, this capture reaction occurs very frequently because of the high concentration of hydrogen in tissue (about 10 wt.%). Such photons (low LET radiation) possess long track lengths, which, as well as the homogeneous distribution of the hydrogen atoms, indicate that this photon contribution may be treated macroscopically as a homogeneous background dose. In addition, the dose from photons originating in the reactor can be treated as a macroscopic background.

9.1.3 Proton Recoil

The scattering of neutrons on hydrogen contributes to the energy deposition in tissue through the slowing down of the resulting recoiling protons. A moving proton, a charged particle, can lose energy in two different ways. The major part of the energy loss occurs in collisions with bound electrons. Another part of the loss is based on the electrostatic repulsion from the nucleus which deflects the protons, the so-called Rutherford scattering. The energy loss due to nuclear interaction is concentrated in a few events, while the electronic interaction is much more uniformly distributed along the path length. Furthermore, the energy loss for electron collisions is considerably larger than the energy loss caused by Rutherford scattering. In the microdosimetry model, therefore, Rutherford scattering is neglected.

For the (thermal) capture reactions the influence of the energy of the incident neutrons on the energy of the emitted particles is negligible. The energy of the recoiling proton, however, depends significantly on the energy of the incident neutron. Assuming that the neutron mass is equal to the mass of a proton and that the fluence rate is uniform, the initial proton direction will be isotropic, and the recoiling proton energy is equal to

$$E'_p = \frac{1}{2} E_n (1 - \cos\tau), \quad (9.1)$$

where E'_p is the proton energy after the collision, E_n the neutron energy before the collision and τ the scatter angle in the centre-of-mass system. This formula is not valid for energies within the thermal range (below 0.5 eV). Although the fluence is not uniform in the macroscopic world, this can be assumed in problems where only a volume is considered with dimensions in the order of microns.

9.2 General description

In the present microdosimetry model, it is supposed that the DNA string (or a part of this string) situated in the nucleus of a cell is the sensitive part of the cell. Adding enough energy to the molecule to break the DNA string

results in a cell which can no longer divide. The sensitive part of the DNA string is only a part of the volume of the nucleus, nevertheless the energy deposition in the nucleus is assumed to be representative for the damage to the DNA string and is calculated in the microdosimetry model. If later it appears that another part of the cell, for example the cell membrane, is (partly) important for the survival probabilities of a cell or that the energy deposition to the nucleus is a too inaccurate approach, the model can be simply changed, by changing the target volume in the deduced theory. The model is a combination of several parts, each with its own function, but with a strong correlation to the other parts. The connections between the different blocks are visualised in figure 9.1. Calculations will normally start with the calculation of microscopic quantities with the Monte Carlo program (block MC1), simulating the transport of the emitted particles in a cell suspension, tissue or capillary model. This program calculates relative values for each reaction separately. Most important are the relative microscopic dose distribution, the interaction changes within the target volume, the track length through the nucleus and the distributions of energy imparted. In the case of the proton recoil interaction, the microdosimetric quantities are dependent on the energy of the incident neutrons. The results are calculated per energy group. In the second block (block MC2), the results are integrated over the energy range, weighted by the product of the scattering cross section and the fluence rate. The subdivision of the results per energy group and the total energy integrated results are introduced to make it easier to consider different spectral characteristics with a minimum of computation time. Results of the Monte Carlo programs will be used in all six deterministic blocks.

The relative values from the Monte Carlo calculations are normalised in a standard spreadsheet (block D1), using the spectral characteristics, irradiation time and concentration and distribution of the nuclide in question in order to calculate the number of interactions in each compartment. The obtained quantities are used to predict relative differences in the radiobiological effectiveness of the total irradiation. A criterion to measure the effect of a certain kind of irradiation or the influence of a different concentration distribution of the atoms in question, is based on the distribution of energy depositions (block D2). Using a computer program written in Turbo Pascal 7.0, the distribution of energy depositions per compartment

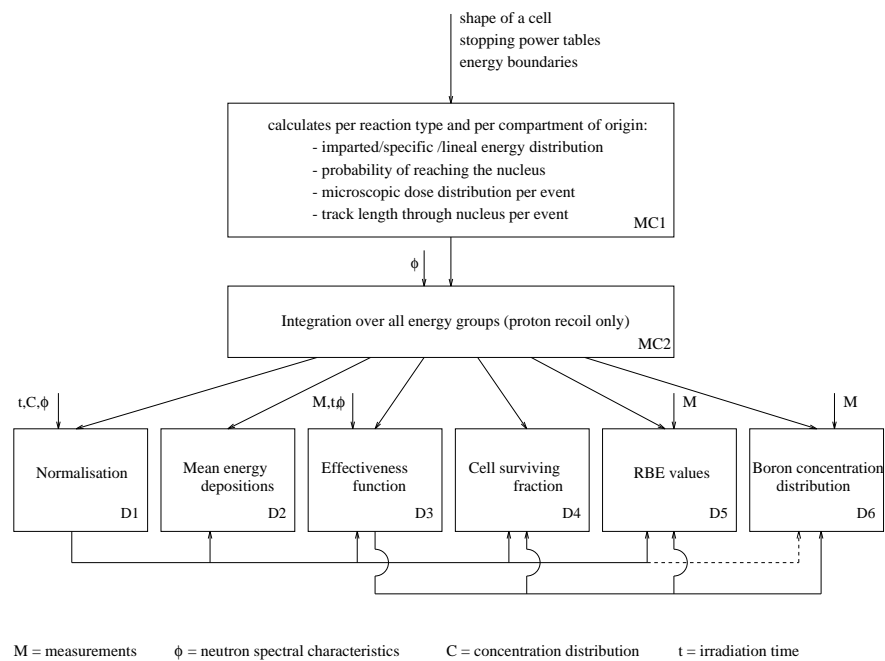


Figure 9.1: Schematic overview of the microdosimetry model

are rescaled to the total distribution of energy deposition. The mean values of these total distributions give the mean energy deposited in the nucleus per particle reaching the nucleus. A higher mean value indicates a more effective type of irradiation or distribution, considering that a higher value means that per event a higher amount of energy is deposited, leading to a higher radiobiological effect.

The first two blocks deal with relative comparison of biological effects. In the third block, D3, the effectiveness function is derived which describes the relation between the energy deposited in the cell nucleus and the probability that this cell is killed. The problem is to define such a function. A large number of extensive measurements under complex circumstances are needed to solve the problem. In the third block, D3, a theoretical method is developed to determine this function based on measurements, using a minimisation technique solved with the least squares approximation. The

theory is implemented in a Fortran program making use of the minimisation routines in the NAG library [NAG, 1993]. Having obtained this effectiveness function, an assorted range of radiobiological effects can be calculated. In the remaining blocks, methods are developed to calculate several biological quantities.

Most experiments to determine the effect of irradiations are based on measurements of the ratio of the number of cells capable of cell division after irradiation and the total number of irradiated cells. This ratio is called the cell surviving fraction. In block D4, these fractions are calculated based on the number of particles reaching the target nucleus (block D1), the total distribution of energy deposition (block D2), and the effectiveness function (block D3).

Another application of the effectiveness function is the calculation of RBE-values. It is common to predict radiobiological effects based on macroscopically calculated dose rates using the RBE-values to include microscopic effects. These values are normally based on measurements. Using the above defined effectiveness function, the RBE-values can be calculated. This method, derived in block D5, is also based on a minimisation problem and is solved by a newly developed Fortran program using the NAG libraries.

The effectiveness function can also be useful in the study of the concentration distribution of boron atoms on a microscopic scale. For most compounds, this distribution is more or less unknown. While it is hard to measure, calculations can give an important indication of the real positions of the atoms. A new minimisation problem is defined in block D6 to calculate this distribution.

Chapter 10

The Monte Carlo model

Simulations of the interaction of neutrons with nuclei and the transport of the emitted particles in a cell suspension, tissue or capillary model are performed in a computer program, written in Turbo Pascal 7.0. The program is based on Monte Carlo techniques and forms the basis of the micro dosimetry model. Results will be used for the deterministic part of the calculations, leading to values for various radiobiological quantities.

10.1 The nuclear reactions

The program calculates the energy deposition for each reaction separately. For the boron capture reaction, it is included that in 93.7% of the events a photon will be released, reducing the energy of the two emitted particles. No special adaptations are needed to calculate the microdosimetric quantities from the nitrogen capture reaction.

In contrast to the capture reactions in the boron and nitrogen nuclei, the energy of the recoiling protons depends on the energy of the incident neut-

ron and on the momentum of the collision. The energy of the neutrons is derived from spectral characteristics calculated with computer codes like DORT and MCNP, their results subdivided into several energy groups. This energy group structure is added to the Monte Carlo program. The program determines randomly the energy of the neutrons within the energy groups, assuming that the neutron energy has a $1/E$ distribution within each energy group. The energy of the recoiling proton is determined with the formula given in the previous chapter (equation 9.1). Based on the proton energy, the accompanying proton track length is calculated using the slowing down of protons in matter (stored in the so-called stopping power tables, section 10.4). The interaction probability for neutrons with thermal energy is very high. However, the energy deposition from these interactions are negligible. In the model, a threshold for the recoiling protons can be set. Protons with an energy below this threshold are neglected. This threshold can be defined by the user. The microdosimetric results are stored separately for each energy group, and are integrated over the energy range in a separate program, which weighs the results of each energy group with the product of the neutron group fluence rates and the energy-dependent scattering groups cross section. This division is made to be able to calculate the influence of different spectral characteristics (with a similar energy group structure) within a minimum of computation time.

10.1.1 Geometry of the modelled cells

In the program, two different shapes of cells are considered: tumour or healthy tissue cells are modelled as ellipsoids, and capillaries as cylinders (see figure 10.1). The cells are divided into different compartments: nucleus, cytoplasm and intercellular space. The capillaries also contain a fourth compartment, viz. the lumen. The dimensions of the individual compartments and the position of the compartment in relation to the other compartments can be considered in two different modes: as constants or as dynamic variables. In the dynamic mode, the variation is based on a random distribution within user-defined limits.

The cell in which the energy deposition is examined is called the target module. In case of the suspension or capillaries the effect of neighbouring

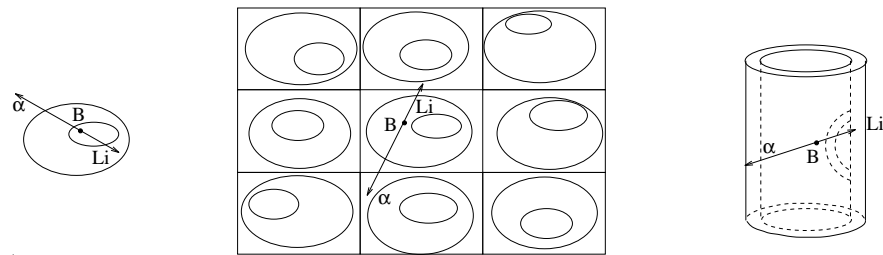


Figure 10.1: Cross section of respectively, cell suspension, tissue and capillary model

cells is negligible because the distance between the cells exceeds the track length of the emitted particles. For these models, only one cell is considered and this is the target cell. The tissue model takes into account the effect of events in the neighbouring cells. The tissue model is a three dimensional array, consisting of one central module and its immediate 26 neighbours. The 27 modules are represented as an array of 3x3x3 modules with the central one defined as the target module (the target module in the tissue model includes the intercellular space, in contrast to the other models). In figure 10.1, a cross section of the models is shown. The limited range of the particles, released by the capture reactions, makes the contribution from capture reactions in modules further away than the adjacent modules negligible. The recoiling protons from interactions further away than the direct neighbouring cells can contribute considerably to the energy deposition in the nucleus. These contributions are considered by choosing the origin of these particles randomly over the volume outside the array of 3x3x3 modules, and the origin of the particles are chosen randomly too, making the ratio between the number of particles per compartment equal to the ratio of the volumes of these compartments.

10.2 Biased Monte Carlo techniques

10.2.1 Location of interactions

Two different kinds of locations can occur: the nuclei for the neutron capture reactions are located in one or more compartments in the model, or the nuclei are situated on the cell membrane. If the nuclei are in one of the compartments, the location of the interactions between the nuclei and the neutrons are assumed to be randomly distributed within that compartment. Also the interactions on the cell membrane are assumed to be randomly distributed over the surface of the membrane. Both kinds of locations of neutron reactions can be handled by the program in separate runs.

In a straightforward approach to determine the locations of interactions, these locations would be randomly defined. This suffices for the capture reactions because of their limited track length. The track length of a recoiling proton (in the model limited to 1000 μm) can be considerably larger. Simulating interactions in a region with a radius of 1000 μm around the target module, would cost too much computation time. To solve this problem biased Monte Carlo techniques are added to the program.

Particles from interactions that are further away from the target module than the track length of the emitted particles will not contribute to the energy deposition in the target module. For each event the track length will be determined. A location is chosen at a distance to the target module less or equal to the track length of that particle. The reduction of the volume in which the interaction can take place, changes considerably for the proton recoil and will be remarkably different for each simulated event. For the simulation of the boron capture reaction, only a small reduction occurs (track length is in 6.3% of the cases smaller than in the other cases), and for the nitrogen reaction, there is no reduction at all. The mean energy deposition from the interaction is influenced by the reduction of the volume in which interactions can occur. Therefore, the results are weighted by the ratio of the newly defined volume and the total volume where events can occur.

10.2.2 Directions of the particles

Reduction of the total volume to a volume in which the particles can reach the nucleus as described in the previous section, will give a considerable reduction of computation time, but is not enough to decrease the computation time to a reasonable length. The isotropic distribution of the directions of the emitted particles makes the probability that the particles will reach the target cell very small. By treating only the particles travelling through the target cell, a large reduction in computation time can be obtained.

Special biased Monte Carlo techniques are developed to force more particles through the target module. Around the target module, the smallest possible sphere enclosing the target module is defined. A new compartment is introduced equal to this sphere minus the target module. Particles from reactions outside this sphere have a low chance to reach the target module, while particles inside the volume have their origin in or close by the target volume and have therefore a large probability to deposit energy in the target module. Based on this large difference in probability of reaching the target module, the determination of the directions of the released particles inside the sphere is treated differently than the ones with an origin outside the sphere. If the event occurs in the target module biased techniques are redundant. A random vector can be generated to obtain a direction. If the reactions take place outside the sphere, the particles are forced through the cell. A random direction is chosen within a cone determined by the origin of the particle and the sphere around the target module. These energy depositions in the target module must be weighted with the relative solid angle of the cone, to obtain the correct results.

10.3 Determination of energy deposition

Knowing the location of the interactions and the direction of the released particles, the energy deposition from the particles in the target module can be calculated. The energy loss of the ionising particles is not constant along their tracks. To account for the changing energy loss, a particle track is partitioned into a certain number of subdivisions and for each partition

the accompanying energy deposition per particle is calculated and stored in the stopping power tables (the generation of these tables is explained in section 10.4).

The Monte Carlo program calculates the dose (unit Gy) and the mean track length of the particles (unit μm) in all compartments of the target modules. These quantities are normalised to 1 event per compartment of origin. In block D1 of the microdosimetry model, the results are scaled to absolute values. This method saves computation time if the effect of different concentration distributions, irradiation times or spectral characteristics (in case of the capture reactions) is considered. The probability that particles from events in one compartment reaches one of the other compartments is also determined. With these probabilities, all obtained within block D1, the numbers of particles crossing the different compartments of a cell can be obtained within block D1.

Three different distributions of energy deposition in the nucleus are calculated. Since the number of particles that have no contribution to the energy deposition in the nucleus can be very high (especially for the proton recoil reaction), the distributions are calculated for particles reaching the target nucleus. Using functions calculated over all events, numerical problems can occur due to mathematical manipulation of very small or very large numbers. The distributions are calculated for the following quantities:

- the energy imparted ϵ (unit keV);
- the specific energy z (unit Gy);
- the lineal energy y (unit keV/ μm).

The distributions are also stored per compartment of origin, to be able to examine the effect of different concentration distributions easily.

10.4 Generation of stopping power tables

10.4.1 Comparison of available data sets for stopping power tables

Stopping power calculations available from literature are used as an input for the microdosimetry model. A comparison between the stopping power of α -particles in water is performed for three different models: Northcliffe and Schilling (N&S) [Northcliffe, 1970], Ziegler (TRIM-88) [Biersack, 1970] and the ICRU-49 report [ICRU, 1983]. To compare the results, the lineal energy deposition (stopping power) against the energy is drawn in figure 10.2.

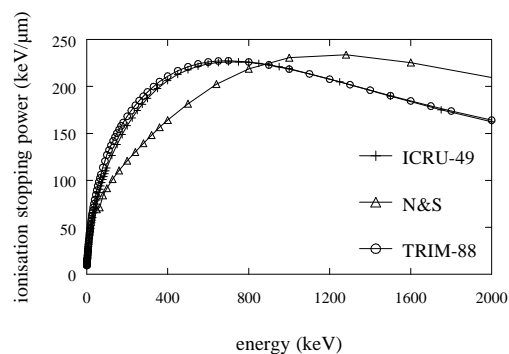


Figure 10.2: *Electric stopping powers of the α -particles in water*

The Northcliffe and Schilling data are significantly different from the other data; the treatment of electron binding for particles is not correct in this model [Wheeler, 1990]. The differences between the ICRU-49 data and the TRIM-88 model are small. The ICRU-49 report deals only with protons and α -particles. Hence, data for other particles have to be taken from earlier reports or other models. The TRIM-code can be used for a material composition up to a maximum of four different elements. Therefore, the TRIM-code is preferred to the ICRU-report.

10.4.2 The TRIM-88 code

The literature gives a large amount of experimentally determined stopping powers and ion range distributions. They are not, however, sufficiently accurate to be extrapolated to unknown systems. To establish this extrapolation based on existing experimental data and unified theoretical concepts, the TRIM-88 code was developed by Ziegler et al. [Biersack, 1970]. In this computer code the total stopping power of ions divides into two parts: the energy transferred by ions to electrons (electric stopping) and the energy transferred to nuclei (nuclear or Rutherford stopping). To determine the accuracy of the theoretical model, Ziegler et al. have statistically analysed the correctness of the total calculated stopping power on available experimental data (about 13,000 data points). They found an average error of 7.4%. For ions used in this report (relative light ions) an accuracy of 5% or better is found.

10.4.3 Electric and nuclear stopping powers

A proton traversing tissue can lose energy in two different ways: by Rutherford scattering and by ionisation stopping. In the microdosimetry model, it is assumed that the energy loss due to Rutherford scattering is negligible in relation to the energy loss due to ionisation. The energy losses for both mechanisms calculated with the TRIM-88 code are shown in figure 10.3. The effect of the above-mentioned assumption on the calculations is negligible (section 9.1.3).

10.4.4 Determination of the stopping power tables

The tables from the TRIM-code have to be converted to a suitable format to be able to import them into the microdosimetry model. The requirement for the two capture reactions, the $^{10}\text{B}(n,\alpha)^7\text{Li}$ and the $^{14}\text{N}(n,p)^{14}\text{C}$ reaction, is a table of residual range divided in equal subdivisions of $0.1\ \mu\text{m}$ and the accompanying electric stopping power. The values of the table obtained by TRIM-88 are discretised with the assumption that the stopping power changes linearly between two data points. To maintain the total energy

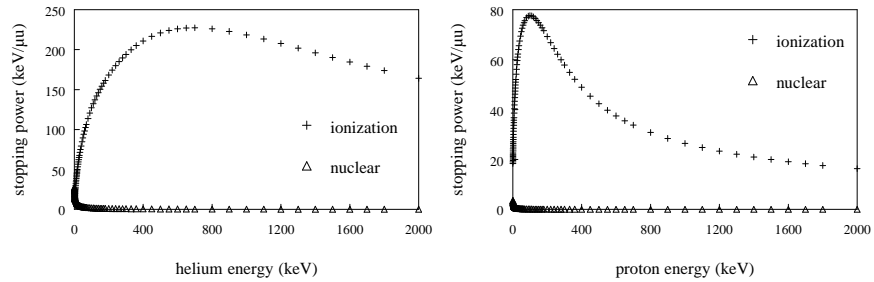


Figure 10.3: *Electric and nuclear stopping powers of the protons and the α -particles in water*

released by the reactions, the sum of the electric and nuclear stopping power in the tables multiplied with the lengths of the subdivisions ($0.1 \mu\text{m}$) must be equal to the total energy of the released particles. For the stopping power of the recoiling protons, the equal subdivisions of $0.1 \mu\text{m}$ are not sufficient: for protons with a high energy the length of the subdivisions is altered up to $1 \mu\text{m}$, decreasing to a length of $0.01 \mu\text{m}$ for protons with energies lower than 10 eV .

10.5 Assumptions of the Monte Carlo program

At different places in the model, assumptions have to be made. Five different kinds of assumptions can be distinguished. The first assumption limits the shape of the cells, viz,

- cells and nuclei can be modelled as ellipsoids.

For the distribution of the location of the reactions it is assumed that:

- the nuclei are homogeneously distributed within a compartment of a cell or close to the cell membrane.

Three assumptions are made about the tracks of the particles:

- the directions of the particle tracks are isotropically distributed,
- the emitted particles move in straight lines, and
- in cases where two particles are released by the same

capture reaction, these particles are emitted back-to-back.

For the generation of the stopping power tables, it is assumed that

- no difference exists between the stopping of particles in the different compartments of the modules; and that
- the nuclear stopping powers are negligible.

The last assumption made in the Monte Carlo program concerns the energy deposition. It is assumed that

- the energy deposition within a compartment of the cell is homogeneously distributed.

Chapter 11

Deterministic models

Using the results of the Monte Carlo model, different quantities necessary for the understanding of the radiobiological effects can be obtained. In this chapter, the deterministic blocks leading to the different microscopic quantities are described.

11.1 Dose distribution and number of tracks through the nucleus (D1)

The Monte Carlo model calculates mean microscopic quantities per event and per compartment of origin. In a spreadsheet, these results are scaled to the experimental situation. This scaling could also be done in the Monte Carlo program itself, implementing information of the neutron spectrum at the irradiation positions, the microscopic concentration distribution of the isotopes, and the irradiation time. But it is deliberately chosen to use a separate spreadsheet to obtain the absolute values, in order to reduce computation time as much as possible.

The normalisation is based on the numbers of interactions in the different compartments. Assuming that the nuclides are homogeneously distributed in the compartments, the number of interactions I_c in a compartment with a volume V_c [μm^3] and a certain isotopic concentration C_c [ppm] is equal to:

$$I_c = 10^{-42} \frac{N_a \rho}{M} C_c V_c \sum_g \sigma_g \phi_g t, \quad (11.1)$$

where,

N_a	= Avogadro's constant	$6.022 \cdot 10^{23} \text{mol}^{-1}$
M	= molecular weight of isotope	amu
t	= irradiation time	s
ρ	= density	g cm^{-3}
σ_g	= absorption microscopic cross section for energy group g for the capture reactions or the scattering cross section for group g in case of the proton recoil	barn
ϕ_g	= fluence rate for energy group g	$\text{cm}^{-2} \text{s}^{-1}$

The number of particles reaching a compartment i of the target cell, N_i , can be calculated based on the numbers of interactions:

$$N_i = \sum_c P_{i,c} I_c, \quad (11.2)$$

where $P_{i,c}$ is the probability calculated by the Monte Carlo program that a particle from an event in compartment c will reach compartment i . Similarly, the mean absorbed dose in compartment i , D_i , and the mean track length through compartment i , L_i can be obtained respectively by:

$$D_i = \sum_c D_{i,c} I_c, \quad (11.3)$$

and

$$L_i = \sum_c L_{i,c} I_c, \quad (11.4)$$

where $D_{i,c}$ is the mean dose per event deposited in compartment i , from interactions in compartment c and $L_{i,c}$ is the mean track length in compartment i from particles with a starting point in compartment c , both calculated in the Monte Carlo program. These quantities can be used to obtain a first estimation of the relative change in the radiobiological effects due to changes in the experimental situation (for example the boron compound, irradiation time or neutron spectrum).

In the situation where most of the energy imparted comes from one type of reaction (in case of BNCT mostly the boron capture reaction), the number of particles from this reaction hitting the nucleus is roughly proportional to the logarithm of the surviving fraction. In this estimation only the number of hits is a criterion of the effect, and no information about the changing energy deposition per hit is included. This is valid if the energy deposition per hit is quite constant. In a second approximation, the sum of the track lengths in the nucleus of all particles released by the most important reaction is more or less linear to the logarithm of the surviving fraction. In this estimation, it is included that the particles can have different track length in the nucleus, but the changing energy loss along the tracks of the particles is not considered. The total dose of the main reaction deposited in the nucleus is a third indication of the cell surviving fraction. In this case the changing track length as well as the changing energy loss along the tracks are taken into account.

11.2 Energy imparted distributions (D2)

Not only the total energy deposition in the cell nucleus is an important parameter in the analysis of radiobiological effects, but also the distribution of the energy depositions over the nucleus. The Monte Carlo program calculates three different distributions of energy depositions: the distribution of the energy imparted; the specific energy; and the lineal energy. The distributions are calculated for each compartment separately, and a computer program is written in Turbo Pascal to calculate the total distribution in the nucleus depending on the actual distribution of the nuclides. For example, the total distribution of specific energy $f(z)$ is calculated by weighting the

distributions per compartment $f_c(z)$ by the number of particles reaching the nucleus released from interactions in that compartment N_c :

$$f(z) = \frac{\sum_c N_c f_c(z)}{\sum_c N_c}, \quad (11.5)$$

The total distribution for the other two distributions is calculated in a similar way.

For the boron and nitrogen reaction, the distributions are independent of the neutron spectrum, because the released energy per event is independent of the spectrum. The distributions for the proton recoil reaction, however, depend on the neutron spectrum because the energy released by the recoiling proton depends on the energy of the incident neutron. In the Monte Carlo calculations the results are stored per energy group and afterwards integrated over the total energy range. Changes in spectral characteristics can easily be considered by first running the program which normalises the distributions per compartment with the given spectral characteristics, and subsequently calculating the total distribution of the energy deposition using equation 11.5.

The mean values of these distributions represent the mean energy released in the nucleus per particle reaching the cell nucleus. These values can be used to get an indication of the effectiveness of the reaction: a higher value means that per particle a high energy deposition occurs, including a higher probability of cell kill. This can, for example, be useful in the study of new boron compounds. In a relatively easy way the different effectivenesses of different boron compounds can be obtained. Multiplication of the mean values with the number of particles reaching the cell nucleus, then gives the total energy deposition in the cell nucleus.

11.3 Determination of the effectiveness function (D3)

The calculation of the number of hits, the mean track length in the cell nucleus, the microscopic dose distribution or the mean specific or lineal

energy imparted in the cell nucleus form a first approach of the cell surviving fractions. In all cases, a linear relation between the physical quantities and the logarithm of the surviving fraction is assumed, and only relative changes can be determined. To obtain absolute cell surviving fraction or other important radiobiological quantities based on a more realistic relation between the calculated quantities and the biological ones, other techniques must be introduced.

The effect of a particle hit depends on the energy deposited in the nucleus, a higher amount gives a larger probability of cell kill. To kill a cell at least a certain amount of energy has to be deposited in the DNA string. If all deposited energy in the nucleus will be given to the sensitive part of the DNA string, the effectiveness function is equal to a step function: below a certain threshold, the energy imparted is too low to break the DNA string, above this threshold, more energy is given to the DNA string than necessary. In reality only a part of the nucleus is filled with the DNA string, and therefore only a part of the particles hitting the nucleus will deposit energy to the DNA string. The probability of energy transfer to the DNA string is a normal distribution, smoothing the step function into an S-curve. This so-called effectiveness function is monotonically increasing, as could be expected from the biological experience that a higher energy deposition leads to a higher effect. Although the literature [Gabel, 1984],[Bond, 1985] shows that such relations can be useful to calculate biological responses, to date only rough estimations of the effectiveness functions are published [Wheeler, 1990].

Different cell types have different radiosensitivities, and as a consequence the effectiveness function will differ for the different cell types and consequently each function has to be deduced separately. A theoretical method based on measurements of cell surviving fractions to obtain the effectiveness functions is developed. The method is described for the specific energy deposition but is similar for the distribution of the lineal energy or the energy imparted. Considering the energy deposition on cellular scale, including the spatial distributions of the nuclides, it makes no difference which particle deposits the energy in the cell nucleus. Accordingly the effectiveness function will not change for the different reactions. As it is

unknown what the effect of earlier hits is on the probability of cell kill, three different models are considered. The so-called 'single event' model supposes that every hit of a nucleus interacts independently of earlier hits, in other words a cell has no memory of earlier hits. In contrast, in the 'multiple event' model, cells remember all hits and the energy depositions of all hits are additive. Both models are an oversimplification of reality. In the single event model, it is not taken into account that some hits will damage the cells but not kill the cells, leading to a changed probability of cell kill for the next event. Many small energy depositions, all too small to damage the cell, can in the multiple events model add to a significant contribution to the total energy deposition. Also in the multiple event model, one particle hit with a certain energy deposition may cause a different effect than another due to the different positions of energy depositions. After all, the radiosensitivity might not be constant over the whole nucleus. Therefore a third model must be considered, which accounts for these factors, using weighting parameters in the multiple event model, the model is therefore called the 'weighted multiple event' model.

11.3.1 Single event model

The number of reactions in the cell nucleus from interactions in a compartment has Poisson distribution. The probability that i particles reach the nucleus is:

$$P_i = \frac{N^i}{i!} e^{-N}. \quad (11.6)$$

where N is the average number of particles reaching the nucleus. Suppose that an individual event causes a cell kill with probability p . Then, for a region that experiences exactly i events, the survival probability for that cell is:

$$(1 - p)^i \quad (11.7)$$

The fraction of surviving cells, S_i , experiencing i tracks through the cell nucleus from the average of N tracks, is equal to

$$S_i = \frac{(N(1 - p))^i e^{-N}}{i!}. \quad (11.8)$$

The surviving fraction SF_s in case of the single event model is given by:

$$SF_s = \sum_{i=0}^{\infty} S_i = e^{-Np}. \quad (11.9)$$

The probability of a biological response from an event can be expressed by the probability of a certain specific energy deposition in the nucleus (the information is stored in the distribution of the specific energy) multiplied by the probability of response to that energy deposition, stored in the effectiveness function. Defining $EF(z)$ as the effectiveness function for the specific energy deposition in the nucleus z , then the surviving fraction for a single event model is obtained by:

$$SF_s = \sum_i \frac{N^i}{i!} e^{-N} (1 - \int f_1(z) EF(z) dz)^i \approx e^{-N \int f_1(z) EF(z) dz}, \quad (11.10)$$

where $f_1(z)$ is the distribution of specific energy (calculated in the Monte Carlo program). The shape of the effectiveness function is, based on radiobiological considerations, equal to a so-called S-curve. The general equation for an S-curve is equal to:

$$EF(z) = \frac{1}{1 + e^{-b(z-a)}}, \quad (11.11)$$

where a and b are two arbitrary (positive) constants. Equation 11.10 is used to describe the cell survival fraction resulting from high-LET irradiation. The low-LET photon irradiation is treated separately:

$$SF_\gamma = e^{\alpha D\gamma + \beta D^2\gamma}, \quad (11.12)$$

where α and β are (negative) constants, experimentally determined by standard photon experiments. The total surviving fraction, including all reactions, is equal to

$$SF_s = SF_\gamma \prod_r e^{-\int \{\sum_r N_r f_{1,r}(z)\} EF(z) dz}, \quad (11.13)$$

where r labels the different reactions, viz. the boron and nitrogen capture and the proton recoil. The distribution of specific energy, $f_{1,r}(z)$ and the

number of tracks through the cell nucleus N_r are obtained from the Monte Carlo program and the deterministic blocks D1 and D2.

If for different spectral characteristics and different concentrations of (at least one of) the atoms, the surviving fractions are known, then the effectiveness function $EF(z)$ as defined in equation 11.11 can be determined by a least squares fit of the parameters a and b :

$$\min_{a,b} \left| \sum_x \sum_C \left(\int_z \left\{ \sum_r N_r(x, C) f_{1,r}(z, x, C) \right\} EF(z) dz + \ln(SF(x, C)) - \ln(SF_\gamma(x)) \right)^2 \right|, \quad (11.14)$$

where x indicates the irradiation positions with different spectral characteristics and C the different concentration distributions of the atoms. Introduction from different spectral characteristics and from different concentration distributions is necessary to obtain enough independent equations to solve the minimisation problem.

11.3.2 Multiple event model

The multiple event distributions are based on the single event distributions. If the single event spectra for the specific energy, $f_1(z)$, are obtained by the program and if it is assumed that the number of energy deposition events, i , is distributed at random and that its distribution function, P_i , is represented by a Poisson distribution (see equation 11.6), then the multiple event spectra, $f_M(z)$, can be calculated by

$$f_M(z) = \sum_i P_i f_i(z), \quad (11.15)$$

where the probability density of z for precisely i energy deposition events, $f_i(z)$, can be derived by an iterative convolution of $f_1(z)$:

$$f_i(z) = \int_0^z f_{i-1}(s) f_1(z-s) ds. \quad (11.16)$$

Similar to the single event model, the surviving fraction based on multiple event spectra is equal to

$$SF_M = SF_\gamma \left(1 - \int_0^z f_M(z) EF_M(z) dz \right), \quad (11.17)$$

where EF_M is the effectiveness function for the multiple events model. The effectiveness function can be obtained from the minimisation problem defined by

$$\min_{a,b} \left| \sum_{x,C} \left(1 - \int_z f_M(z, x, C) EF_M(z) dz \right) - SF(x, C)/SF_\gamma(x) \right|^2. \quad (11.18)$$

11.3.3 Weighted multiple event model

Instead of simply adding all energy depositions in the nucleus, as in the multiple event model, a weight factor can be used to account for the effects of earlier hits. The total distribution of energy deposition, parallel to section 11.3.2, becomes

$$f_w(z) = \sum_i P_i f_i(z), \quad (11.19)$$

where the probability density of z for precisely i energy deposition events, $f_i(z)$, can be derived by an iterative convolution of $f_1(z)$:

$$f_i(z) = \int_0^z f_{i-1}(s) w_1(z-s) f_1(z-s) ds \quad (11.20)$$

The surviving fraction in the weighted multiple event model is

$$SF_w = 1 - \int f_w(z) EF_w(z) dz, \quad (11.21)$$

where EF_w is the effectiveness function for the weighted multiple events model. Different assumptions can be made about the weighting function. For example, if a linear correlation is assumed between the specific energy and the weighting function w_1 ,

$$w_1(z) = c z, \quad (11.22)$$

then the weighting function and the effectiveness function can be obtained by

$$\min_{a,b,c} \left| \sum_{x,C} \left(\int_z f_w(z, x, C) \text{EF}_w(z) dz + \text{SF}(x, C) - \text{SF}_\gamma(x) \right) \right|^2. \quad (11.23)$$

Similar to this, other relations between the weighting function and the specific energy can be used.

11.4 Calculation of the cell surviving fraction (D4)

In section 11.3, the effectiveness functions of a certain cell type for the different models were determined based on measured surviving fractions and results of the Monte Carlo model. Having obtained the effectiveness functions, the same formulas can be used to calculate the surviving fractions for given experimental conditions.

11.5 Theoretical estimation of the RBE values (D5)

In the first four deterministic blocks, microscopic quantities are used to calculate surviving fractions. Although microscopic quantities (quantities calculated on cellular level) are more useful in the study of radiobiological effects than macroscopic quantities (on tissue level), in experiments and radiotherapy, macroscopic doses are used. Using macroscopic quantities, the dose must be discriminated by reaction. Also effects caused by different microscopic concentration distributions must be taken into account. One frequently used method to include these effects is that the different macroscopic dose rates are weighted with their specific RBE values. The surviving fractions can then be calculated by:

$$\text{SF} = e^{\alpha D + \beta D^2} \quad (11.24)$$

where

$$D = D_{\text{photon equivalent}} =$$

$$\text{RBE}_B D_B + \text{RBE}_N D_N + \text{RBE}_R D_R + D_\gamma \quad (11.25)$$

The RBE of photons is per definition equal to 1. Although in theory this method works, a large problem exists for the determination of the RBE's. A lack of consensus exists between different sets of measurements. Using microscopic considerations, the RBE values can be calculated. A relation between the RBE's for the single event model of different irradiation types can be:

$$\text{INT}_r = \frac{\text{number of hits}}{\text{macroscopic dose}} \int f_1(z) \text{EF}_s(z) dz, \quad (11.26)$$

where r indicates the different reactions. Using measured survival fractions, the absolute RBE's can be determined based on the following least squares equation:

$$\min_a \left| \sum_x \sum_C \ln(\text{SF}(x, C)) - \alpha D - \beta D^2 \right|, \quad (11.27)$$

where $a = \text{RBE}_B$ and

$$D = a(D_B + \frac{\text{INT}_N}{\text{INT}_B} D_N + \frac{\text{INT}_R}{\text{INT}_B} D_R) + D_\gamma. \quad (11.28)$$

The RBE for the boron reaction is directly calculated by the minimisation problem, while the other RBE factors can be obtained based on the ratio with the RBE for boron as is calculated in equation 11.26

11.6 Determination of the boron concentration distributions (D6)

The calculations of the surviving fraction, the effectiveness function or the RBE factors are based on the knowledge of the concentration distribution of the radiation emitting nuclides. In this investigation, the concentration distributions of the nuclides are supposed to be known. In reality, the distribution (in general) of the boron is heterogeneous, making the determination of radiobiological effect after irradiation very difficult. The concentration

distributions can be calculated with the microdosimetry model using the effectiveness functions, the distributions of energy deposition, and the measured surviving fractions. A new minimisation problem is defined based on the single event model:

$$\min_{C_c} \left| \sum_x \left(\int_z \sum_r \sum_c (N_r(x, C_c) f_r(z, x, C_c)) \text{EF}(z) dz + \ln(\text{SF}(x, C_c)) - \ln(\text{SF}_\gamma(x)) \right) \right|^2, \quad (11.29)$$

where C_c is the boron concentration in compartment c .

Chapter 12

Analysis of a radiobiological experiment

12.1 Introduction and description of the experimental situation

12.1.1 Experimental situation

To analyse the effects of the mixed field irradiation from BNCT, numerous radiobiological experiments have been performed at the BNCT irradiation facility of the HFR, using as a biological probe Chinese hamster cells (V79 cells) [Huiskamp, 1992]. This comprehensive set of data is analysed by the microdosimetry model described in the previous chapters. Where possible, the results from the different blocks of the computer model are validated against measurements.

Different irradiation times are used in the experiments: viz. 15, 30, 45, 60 or 90 minutes. For the minimisation problems (see chapter 11) only the

data for 30 minutes are used, while the other irradiation times are used as independent data to check the results.

12.1.2 Neutron spectrum

The cell suspensions are irradiated in the cylindrical phantom as described in chapter 6. Based on the conclusions of part II, the characteristics calculated with the DORT code and the BUGLE-80 library are used as input for the microdosimetry model. Influences of the underestimation of the fast part of the neutron spectrum are considered within a sensitivity analysis, performed in the next chapter.

12.1.3 Concentration distribution of the different atoms

In this experiment, four different macroscopic boron concentrations are used, viz. 0, 15, 30 and 45 ppm. The boron atoms are contained in the compound boric acid. In general, it is assumed that this compound is homogeneously distributed throughout the whole suspension, and this assumption is used when the calculations are compared with the measurements. To investigate the effects of the microscopic distribution two other microscopic boron concentration distributions are considered, leading to the following three microscopic concentrations (between brackets is the name used in tables and figures):

- a homogeneous distribution (homog),
- homogeneously distributed through the intercellular space and cytoplasm (cyto+int),
- boron atoms are homogeneously distributed in the intercellular space (int).

The macroscopic concentrations in all three cases are equal.

The V79 cells consist of 1.7 wt.% of nitrogen atoms [Gabel, 1984]. In a cell suspension the nitrogen concentration in the intercellular space is difficult to determine. The cells are cultivated on a growth medium that contains a certain amount of nitrogen atoms. Before the cell suspensions are poured into the small vials, the cells are "washed" removing most of

the nitrogen from the growth medium. A small concentration of nitrogen atoms, however, will remain in the intercellular space. To see the effect of the nitrogen atoms in the intercellular space, three different distributions are considered:

- the concentration outside the cells is equal to the concentration inside the cells (homog), or
- only a small number of nitrogen atoms are outside the cells (cell+int),
- no nitrogen atoms are outside the cells (cell).

The nitrogen concentrations in the intercellular space for these three cases are respectively, 1.7 wt.%, 0.05 wt.% and 0 wt.%.

The hydrogen atoms are assumed to be homogeneously distributed throughout the whole cell suspension, only one distribution is considered. The hydrogen concentration is 11 wt.%. During irradiations with BNCT, most neutrons have a thermal energy, resulting in a large number of recoiling protons with an energy below 1 eV. The binding energy of atoms is higher than 1 eV, hence these protons cannot cause any damage to the cell. Therefore, protons with an energy below this threshold are neglected in the calculations. The effect of using a threshold is compared with calculations using no threshold. Also calculations have been performed neglecting all protons with an energy lower than 5 eV.

12.2 Calculations made with the Monte Carlo program (MC)

The V79 cells are modelled as ellipsoids with mean diameters of 7.6 μm for the nucleus and 13.0 μm for the cytoplasm. The dynamic variations of the nucleus and cytoplasm diameters are limited to a maximum of 10%, and the nucleus can be at a random position in the cell. The volume of a cell is 1150 μm^3 , including the nucleus which has a volume of 230 μm^3 . The calculations are performed using the cell suspension model (section 10.1.1). The energy depositions from the capture reactions and the recoiling protons are calculated in separate runs.

To avoid influence on the results of statistical uncertainties, a huge number of events are simulated in the Monte Carlo model: for the boron and nitrogen reaction 1,000,000 events and for the proton recoil for each energy group 100,000 events. Results of the Monte Carlo program are not directly useful for comparison with measurements but are used as input in the deterministic blocks of the program.

12.3 Dose distribution and number of tracks (D1)

12.3.1 Number of particles through the nucleus

The total number of events in compartment c can be calculated from the physical parameters as described in equation 11.1. Knowing this number and the probability that a particle reaches the nucleus, which probability is calculated by the Monte Carlo program, the number of tracks through the nucleus can be obtained (equation 11.2).

In the microdosimetry model, the different particles released by the same capture reaction are treated along one track. If the reaction takes place outside the cell nucleus, only one particle can reach the cell nucleus because the directions of the particles are opposite. The number of particles going through the nucleus is proportional to the reacting number of reacting nuclides in the suspension. In this section only a macroscopic boron concentration of 15 ppm is considered, the results of the other concentrations are obtained by multiplying the results for 15 ppm with a factor 2, for a concentration of 30 ppm, and with a factor 3 for the 45 ppm concentration.

In table 12.1, the numbers of particles crossing the nucleus are given for the five irradiation positions on the beam-line centre (see figure 6.1). The first column indicates the microscopic concentration distribution. Due to the large intercellular space in cell suspensions, the microscopic boron concentration is for all distributions equal to 15 ppm, which is the macroscopic boron concentration. The boron and nitrogen capture reactions have a large reaction rate for neutrons with a low energy. The number of interactions is the highest for the thermal neutron peak, which is close to the second

Table 12.1: Number of tracks through the nucleus for the different reactions and positions (h^{-1})

distribution	pos. 1	pos. 2	pos. 3	pos. 4	pos. 5
boron					
homogeneous	4.69	4.90	2.95	1.44	0.632
cyto + int	3.21	3.36	2.02	0.984	0.433
int	1.49	1.56	0.938	0.457	0.201
nitrogen					
homogeneous	1.86	1.94	1.17	0.569	0.250
cell + int	0.991	1.04	0.623	0.304	0.134
cell	0.964	1.01	0.607	0.296	0.130
proton recoil					
$E_p > 0$ eV	1841	1591	902	428	186
$E_p > 1$ eV	383	118	28.5	6.71	1.79
$E_p > 5$ eV	290	83.1	19.3	4.58	1.31

^{a)} Microscopic concentration distributions as described in section 12.1.3

irradiation position, leading to the highest amount of tracks through the nucleus. The probability that a neutron interacts with a proton is, over a wide range, independent of the neutron energy. Therefore, not the energy of the neutrons but the number of neutrons is important in determining the number of tracks through the cell nucleus. The number of neutrons, and by that the number of tracks through the nucleus, decreases with increasing depth in the phantom.

The number of hits in the nucleus from the proton recoil reaction is many times higher than the number of hits from the capture reactions. Comparing the boron reaction with the proton recoil reaction, the large difference comes mainly from the much higher concentration of the hydrogen atoms: the boron concentration is approximately a factor of 7000 lower. The flu-

ence weighted cross section is approximately 600 times lower for the proton recoil reaction than for the boron reaction. Also the differences in the mean track length of the particles released by the reactions have an influence on the number of tracks (see section 12.3.2). The effect of introducing a low threshold for the recoiling protons is large. Many protons will interact with the thermal neutrons but their track length and their energy is lower than the trial threshold (1 eV and 5 eV respectively). The nitrogen concentration is much higher than the boron concentration, but the nitrogen reaction has a lower mean cross section (for position 1 the cross section is approx. 0.98 barn). A lower mean track length of the particles leads to a lower number of tracks through the cell nucleus.

The different microscopic concentration distributions have a large effect on the number of tracks through the cell nucleus (see table 12.1). In the case of the boron reaction, the number of boron atoms in the whole cell suspension is the same for the three different situations. If there are no boron atoms in the cell nucleus, the number of tracks through the cell decreases by 30%, and if there are only boron atoms outside the cell, this decrease is a factor of 3. The larger distance between the boron atoms and the cell nucleus gives a lower probability that the particles released by the boron reaction will reach the cell nucleus. The nitrogen concentration inside the cells is in all cases equal to 1.7 wt.%. If the concentration outside the cell is equal to the concentration inside the cell, the number of tracks through the cell is highest. A small concentration outside the cell or no atoms in the intercellular space gives a similar number of particles going through the cell nucleus.

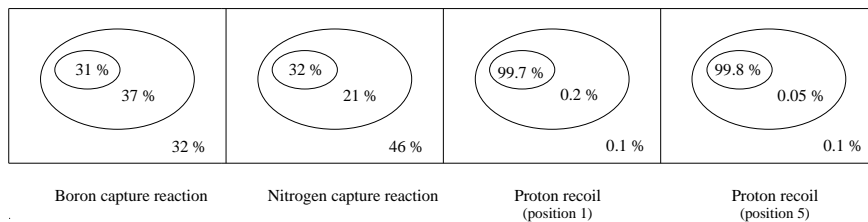


Figure 12.1: Origin of the particles that cross the nucleus, assuming a homogeneous distribution of the reacting nuclides (in percentages)

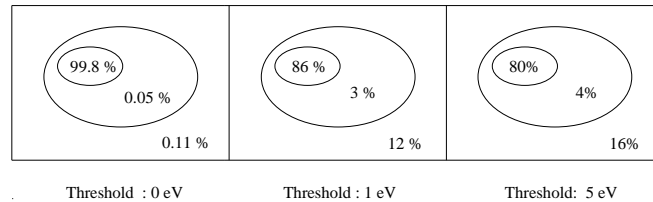


Figure 12.2: Origin in percentages of the recoiling protons that cross the nucleus for different lower boundaries (position 5)

In figure 12.1, the compartment of origin of the particles reaching the cell nucleus is shown as a percentage of the total number of tracks reaching the nucleus, assuming a homogeneous concentration distribution. These percentages are for the capture reaction independent of the position in the phantom, because the particle tracks are independent of the neutron spectra. The percentages for the proton recoil change slightly for the different positions, the results of the first and last irradiation position on the beam centre-line are shown. Using no threshold for the initial proton energy, the origin of the recoiling protons is mainly the nucleus, only a few particles from interactions outside the nucleus can reach the nucleus. Using a threshold of 1 or 5 eV the contributions of (very) low energy protons in the nucleus are reduced (see figure 12.2), resulting in a higher contribution of the other compartments. The capture reactions have a more equal distribution of origin of the tracks.

12.3.2 Mean track length in nucleus

The track length in the nucleus for the capture reactions is defined as the sum of the tracks of both particles from the same reaction within the nucleus. For the boron and nitrogen capture reaction, the mean track length in the nucleus is independent of the spectral characteristics. Different microscopic concentration distributions cause different mean track lengths. For the concentration distributions described in section 12.1.3, the mean track lengths, as calculated with equation 11.4, are given in table 12.2. The tracks of recoiling protons depend on the neutron spectrum. Consequently, the mean track length in the nucleus changes for each position in the

phantom. The mean lengths for the five positions on the beam centre-line are also shown in table 12.2.

Table 12.2: Mean track lengths [μm] in nucleus for different concentration distributions (boron and nitrogen) and irradiation positions (proton recoil).

boron	homog	cyto + int	int		
	3.73	2.97	2.39		
nitrogen	homog	cell + int	cell		
	3.42	3.59	3.60		
proton recoil	pos. 1	pos. 2	pos. 3	pos. 4	pos. 5
$E_p > 0 \text{ eV}$	0.012	0.0053	0.0042	0.0049	0.00071
$E_p > 1 \text{ eV}$	0.058	0.072	0.13	0.31	0.74
$E_p > 5 \text{ eV}$	0.065	0.084	0.16	0.38	0.87

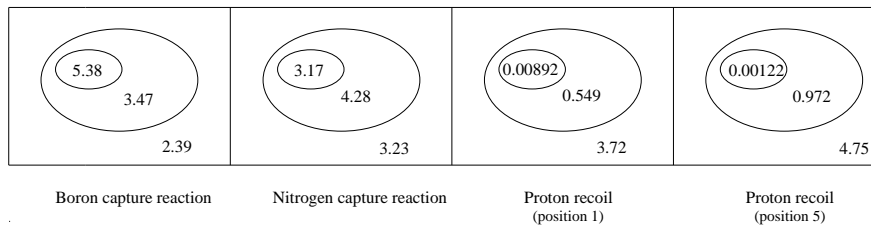


Figure 12.3: Mean track length [μm] in the nucleus from particles originating in the nucleus, cytoplasm or intercellular space.

In table 12.2, the mean track length for a certain concentration distribution is given. The mean track length in the nucleus per compartment of origin is considered in figure 12.3. Both particles released by the boron reaction have track lengths of the same order of magnitude. Therefore reactions in the nucleus always have a high probability of a large track length in the nucleus, resulting in a high mean track length for this compartment. Looking at interactions farther from the cell nucleus, the mean track length decreases. The particles are emitted back-to-back, hence only one particle

can cross the nucleus and contribute to the track length in the nucleus.

In contrast to the boron reaction, the particles released by the nitrogen reaction have track lengths of different order ($10.9 \mu\text{m}$ for the proton and $0.3 \mu\text{m}$ for the carbon ion). The mean track length comes mainly from the released protons. Due to the short track length of the carbon, only protons released from events in the cytoplasm or intercellular space can reach the nucleus, resulting in a higher mean track length for these compartments of origin.

The track lengths of most recoiling protons are very small due to the thermal spectrum at the irradiation positions. These low track lengths cause a very low mean track length for protons started in the nucleus. The mean track length changes with a changed spectrum. At depth the spectra becomes more thermal, reducing the mean track length. As the distance between the nucleus and the other compartments is relatively large, only protons with high energy can reach the cell nucleus, resulting in a higher track length for these compartments.

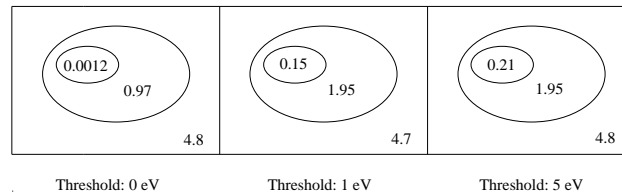


Figure 12.4: Mean track length [μm] in the nucleus from the recoiling protons originating in the nucleus, cytoplasm or intercellular space, using different lower boundaries for the proton recoil reaction (position 5).

Using a threshold of 1 eV or 5 eV for the proton energies, the mean track lengths for the different compartments at position 5 are given in figure 12.4. Using a threshold, the mean track length in the nucleus from interactions in the nucleus itself increases considerably, because the large number of protons with a small track length is neglected. The change in the mean track length of interactions in the cytoplasm is smaller. Fewer protons with a short track length reach the cell nucleus, which increases the mean track

length. The difference between a threshold of 1 eV and a threshold of 5 eV is negligible. The mean track length from events in the intercellular space remains unchanged, because the protons with a low track length have no probability of reaching the cell nucleus and are in all cases negligible for the mean track length in the nucleus.

12.3.3 Microscopic dose

If the lineal energy transfer of the particles along their tracks are constant then the microscopic dose would be proportional to the product of the number of hits and the mean track length. In reality, the lineal energy transfer varies as a function of the track length, causing slight differences in the microscopic dose. The dose distribution on a microscopic scale per compartment of origin is calculated by the Monte Carlo program. Using equation 11.3, the microscopic dose distribution can be calculated. In table 12.3, the microscopic dose rates delivered to the nucleus for the different reactions at positions 1 to 5 are given.

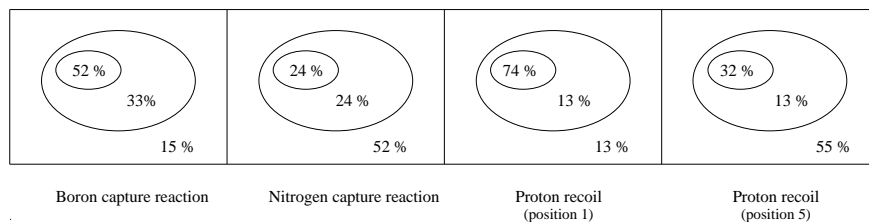


Figure 12.5: Contribution to the total dose in the nucleus from the different reactions and compartments of origin, considering a homogeneous distribution. Only the proton recoil contribution changes with different positions

The number of hits, as well as the mean track length, decreases if the boron atoms are situated outside the nucleus or outside the cell for the same macroscopic concentration distribution. This effect is enhanced in the microscopic dose. The boron and nitrogen doses are the highest at the thermal fluence rate peak. The nitrogen dose is a factor of 10 lower than the boron dose, because of a lower number of particles reaching the cell

Table 12.3: Microscopic dose rate delivered to the nucleus [Gy/h]

reaction	pos. 1	pos. 2	pos. 3	pos. 4	pos. 5
boron					
homog	2.33	2.43	1.47	0.713	0.314
int + cyto	2.07	2.16	1.30	0.633	0.278
int	0.715	0.748	0.450	0.219	0.0964
nitrogen					
homog	0.240	0.251	0.151	0.0735	0.0323
cell + int	0.119	0.124	0.0747	0.0364	0.0160
cell	0.115	0.120	0.0724	0.0353	0.0155
proton recoil ^a					
homogeneous	0.611	0.234	0.0973	0.0464	0.0248

^a) Effect of threshold of recoiling protons on the calculated dose is negligible

nucleus as is given in table 12.1 and the lower amount of energy deposited by the particles from the nitrogen reaction. The mean track length is almost equal for both particles. The influence of a low amount of the nitrogen atoms in the intercellular space is negligible, as it was for the number of tracks though the nucleus and the mean track length. The contribution of the proton recoil dose to the total dose is not negligible. The high number of tracks though the nucleus compensates the short mean track length of the recoiling proton. Using a threshold for the energy of the recoiling protons has a negligible effect on the total energy deposition in the nucleus. The energies of these protons are too low to have any contribution to the total dose. Moving further into the phantom, the importance of the proton recoil contributions decreases faster than the contribution from the capture reactions. Per reaction, the contribution to the total dose in the nucleus of that reaction is shown in figure 12.3.3.

12.3.4 Validation of the model with macroscopic dose

Except for comparison with other microdosimetry models and for generating several cross references in the results to assure consistency in the model, it is difficult to validate the calculated microdosimetry quantities. One possible check of the calculated microscopic dose (for homogeneously distributed atoms) is the comparison of the calculated dose with the macroscopic dose.

Assuming that all the energy released by each capture event is deposited in the tissue and that the density of tissue is equal to 1 g/cm^3 , the total dose rate for a homogeneous boron distribution is given by the multiplication of the released energy per event by the number of events. The homogeneous dose rate for the capture reactions is equal to

$$\dot{D} = 5.77 \cdot 10^{-37} C E N_a \sigma \phi / M \quad [\text{Gy/h}], \quad (12.1)$$

where E is the released energy per event [MeV], C is the concentration of the isotope considered [ppm], N_a Avogadro number is, σ the microscopic cross section [barn], ϕ the neutron fluence rate [$\text{cm}^{-2}\text{s}^{-1}$] and M the molar mass. The dose rate for homogeneously distributed hydrogen atoms is equal to

$$\dot{D} = 5.77 \cdot 10^{-33} C N_a \phi K / M \quad [\text{Gy/h}], \quad (12.2)$$

where K stands for the macroscopic KERMA factors (which for this exercise are taken from the BUGLE80 library [Roussin, 1980]). The dose rates calculated with these equations ("direct") and the dose calculated with the microdosimetry model ("model") are given in table 12.4.

A good agreement between the directly determined (physical) dose rates and the calculated dose rate is obtained. The physical (macroscopic) dose rates cannot directly be compared with biological effects, because different types of irradiation cause different biological effects. In general RBE factors are used to predict the biological effect. The healthy-tissue RBE for recoil protons can be many times higher than the RBE for boron and therefore proton recoil can contribute more to the biological dose than the $^{10}\text{B}(n,\alpha)$ reaction or photons. Due to the difficulties in the determination of RBE

Table 12.4: *Macroscopic dose rates [Gy/h] of the different sources of energy deposition*

position	$^{10}\text{B}(n,\alpha)^7\text{Li}$		$^{14}\text{N}(n,p)^{14}\text{C}$		proton recoil	
	model	direct	model	direct	model	direct
1	2.33	2.39	0.240	0.251	0.611	0.616
2	2.43	2.50	0.251	0.262	0.234	0.237
3	1.47	1.51	0.151	0.158	0.0973	0.0988
4	0.713	0.733	0.0735	0.0769	0.0464	0.0473
5	0.314	0.323	0.0323	0.0338	0.0248	0.0253

factors, more accurate predictions of biological effects can be obtained by microdosimetric calculations.

12.3.5 Calculated relative surviving fractions compared with measurements

The number of tracks through the nucleus, the mean track length and the microscopic dose in the nucleus form an indication of the relative course of the surviving fraction. The logarithm of the surviving fraction is proportional to the relative change in these quantities. In table 12.5, the quantities are compared with measured surviving fractions. For calculations, a homogeneous boron concentration of 15 ppm is used and the nitrogen concentration outside the cell is set to 0.05 wt.%. The normalisation is done with respect to position 2, the thermal fluence rate peak.

The number of tracks, the total track length and the microscopic dose calculated for the boron reaction, gives (in this case) a good prediction of the relative course of the surviving fraction except for positions 1 and 5. In this position the contribution of the proton recoil is too important to neglect. Simply adding the dose distributions from the different reactions leads to a bad prediction of the surviving fraction. In this comparison a

Table 12.5: Comparison of measured cell surviving fractions (SF) with calculated microdosimetry quantities (irradiation time is 30 minutes, boron concentration is 15 ppm)

position	SF	$-\ln(\text{SF})$	number of boron tracks	total track length B [μm]	D_B^a in nucleus [Gy]
Absolute					
1	0.216	1.53	2.35	8.74	2.33
2	0.274	1.29	2.45	9.14	2.43
3	0.460	0.777	1.48	5.50	1.47
4	0.677	0.390	0.720	2.68	0.713
5	0.771	0.11	0.316	1.18	0.314
Normalised					
1	-	1.2	0.96	0.96	0.96
2	-	1	1	1	1
3	-	0.60	0.60	0.60	0.60
4	-	0.30	0.29	0.29	0.29
5	-	0.085	0.13	0.13	0.13

^{a)} microscopic boron dose

boron concentration of 15 ppm is used, a higher boron concentration leads to a better agreement.

12.4 Distributions of energy depositions (D2)

In the second block of the deterministic model the distributions of energy depositions are calculated based on the results of the Monte Carlo model and the number of tracks through the cell nucleus, as calculated in deterministic block D1. In this section, the distribution of energy imparted, as well as the distribution of lineal energy, are shown for the single event and the multiple event model. The differences between the specific energy distribution and the energy imparted distribution are negligible, because the volume and the shape of the nucleus in this experiment are almost constant.

The distributions of the boron and nitrogen reactions are independent of the neutron spectrum. The different microscopic concentration distributions, as described in chapter 12.1.3, are considered. For the proton recoil, the distributions are given for the five positions on the beam centre-line. The distributions for the single event are given in the figures 12.6 to 12.8. The lineal distribution shows the energy dependence of the neutron energy of the proton recoil contribution. In figure 12.11 the influence of different thresholds are considered. The difference between no threshold and a threshold is considerable. The high amount of low energy protons causes a high number of low energy depositions. Because the distributions are normalised to 1, this effect is shown by a lower frequency at higher energy depositions than in case a threshold is used. The differences between a threshold of 1 or 5 eV is negligible.

The distributions for the multiple events model depend on the microscopic dose distributions, the macroscopic concentration, the irradiation time and the position for all reactions. After all, the distributions are dependent on the Poisson distribution of hits in the nucleus, which numbers are dependent on the neutron spectra. In the figures 12.10 and 12.11, the multiple event distributions for different macroscopic boron concentrations at position 1 are shown. For the nitrogen and proton recoil reactions the distributions are given for the five positions at the beam centre-line. A higher boron concentration gives a higher mean number of tracks through the nucleus. The multiple event distribution for higher concentration is therefore shifted

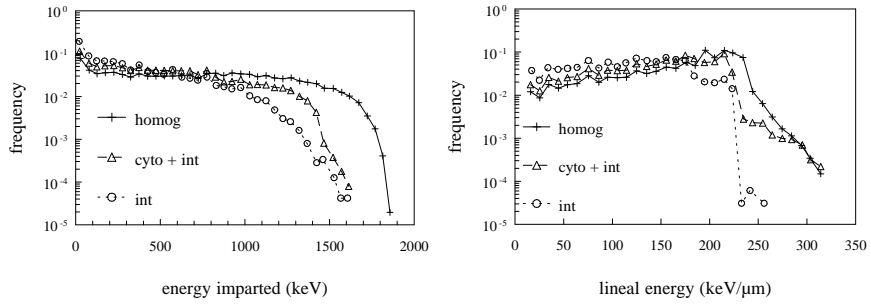


Figure 12.6: Energy spectra of the boron reaction for different concentration distributions (Single event model)

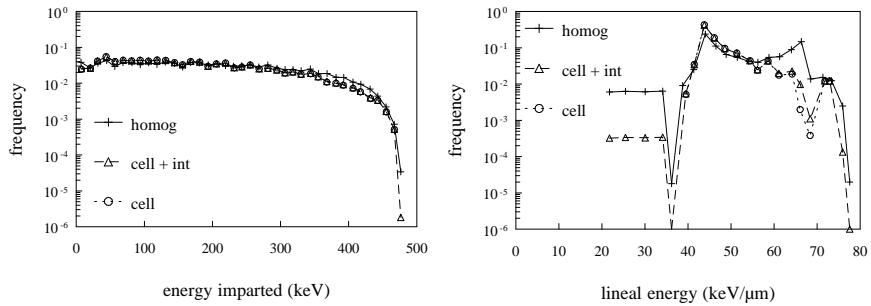


Figure 12.7: Energy spectra of the nitrogen reaction for different concentration distributions (Single event model)

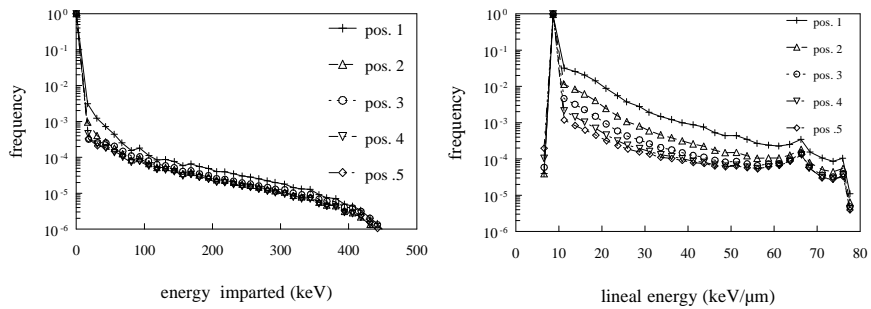


Figure 12.8: Energy spectra of the proton recoil reaction for different positions (Single event model, no threshold)

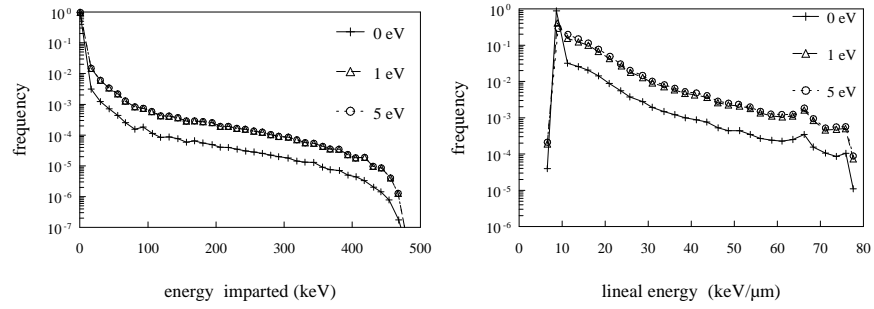


Figure 12.9: Energy spectra of the proton recoil reaction for different thresholds (Single event model, position 1)

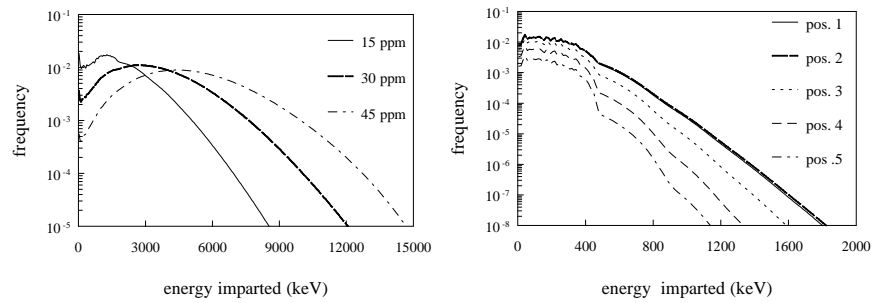


Figure 12.10: Multiple event energy spectra of the boron reaction for different macroscopic boron concentrations (position 1) and of the nitrogen reaction for different irradiation positions (irradiation time 30 minutes)

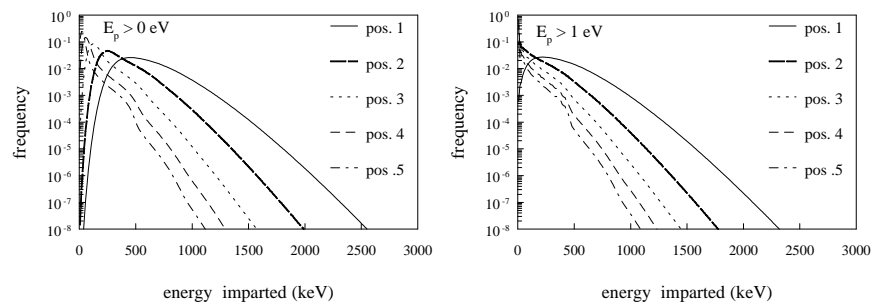


Figure 12.11: Multiple event energy spectra of the proton recoil reaction for different irradiation positions using different thresholds (irradiation time 30 minutes)

to higher values of the energy imparted. The same is shown in the distributions of the proton recoil. At position 1 more tracks are going through the nucleus than in position 5.

The mean values of the distributions of energy depositions give an indication of the effectiveness of the different reactions based on their accompanying microscopic concentration distribution. A high mean value gives a high probability that a cell is killed by one particle. Reactions or distributions with a low mean value require many hits before a cell is killed. In table 12.6, the mean values of the single event distributions are shown. The mean values of the multiple event model are equal to the product of the average values from the single event model and the number of hits. A homogeneous distribution of boron atoms is very effective in killing cells compared with the other reactions and distributions. The proton recoil reactions are not very effective. But as shown in table 12.1, the recoil of the protons occurs many times more than the boron capture reaction, which compensates the low effectiveness. However, most of the protons have an energy lower than 1 eV. By introducing a threshold for the recoiling protons, the effect of the proton recoil reaction increases considerably.

Several relationships exist between the results of the first two deterministic blocks of the microdosimetry model. Some are mentioned below. The mean energy imparted $\bar{\epsilon}$ [keV], specific energy \bar{z} [J/kg] and lineal energy \bar{l} [keV/ μm] are related:

$$\bar{\epsilon} \simeq \frac{\bar{z} \cdot V_{\text{nuc}}}{0.16} \simeq \bar{l} \cdot \bar{T}, \quad (12.3)$$

where \bar{T} is the mean track length of the particles in the nucleus [μm]. These quantities are subsequently related to the microscopic dose in the nucleus D_{nuc} , by multiplying these numbers with the numbers of tracks through the nucleus N_{nuc} :

$$D_{\text{nuc}} \simeq \bar{z} \cdot N_{\text{nuc}}. \quad (12.4)$$

Table 12.6: Mean values of the imparted, specific and lineal energy distribution in the nucleus for different neutron spectra (proton recoil) and concentration distributions (boron and nitrogen capture reaction). Single event model

reaction	mean energy imparted [keV]	mean specific energy [J/kg]	mean lineal energy [keV/ μm]
boron			
homog	711	0.495	168
cyto + int ^a	501	0.349	145
int	350	0.243	116
nitrogen			
homog	187	0.130	53.4
cell + int	171	0.119	48.2
cell	170	0.118	47.9
proton recoil (no threshold)			
pos. 1	0.477	$3.31 \cdot 10^{-4}$	9.84
pos. 2	0.211	$1.47 \cdot 10^{-4}$	9.01
pos. 3	0.155	$1.08 \cdot 10^{-4}$	8.80
pos. 4	0.156	$1.08 \cdot 10^{-4}$	8.73
pos. 5	0.191	$1.33 \cdot 10^{-4}$	8.71
proton recoil (threshold 1 eV)			
pos. 1	2.30	$1.60 \cdot 10^{-4}$	14.4
pos. 2	2.86	$1.99 \cdot 10^{-4}$	13.8
pos. 3	4.92	$3.43 \cdot 10^{-4}$	14.1
pos. 4	9.95	$6.93 \cdot 10^{-4}$	15.4
pos. 5	19.9	$1.38 \cdot 10^{-3}$	17.9
proton recoil (threshold 5 eV)			
pos. 1	2.58	$1.79 \cdot 10^{-3}$	15.3
pos. 2	3.35	$2.33 \cdot 10^{-3}$	14.9
pos. 3	5.94	$4.13 \cdot 10^{-3}$	15.5
pos. 4	12.1	$8.91 \cdot 10^{-3}$	17.1
pos. 5	23.4	$1.63 \cdot 10^{-2}$	19.6

^a) see section 12.1.3

12.5 Determination of the effectiveness function (D3)

The effectiveness function is calculated for the single event model and the multiple event model. The measured surviving fractions after an irradiation time of 30 minutes are used. All boron concentrations and positions are taken into account in the model. The minimisation problems are carried out for the energy imparted and the lineal energy distributions using the single event model. The obtained curves are shown in figure 12.12. Similar, the effectiveness function for the multiple event model is calculated using the energy imparted distribution. The result of this minimisation problem is given in figure 12.13. The calculated effectiveness functions are only valid for the V79 cells; other cells will react differently during irradiations, resulting in a different effectiveness function.

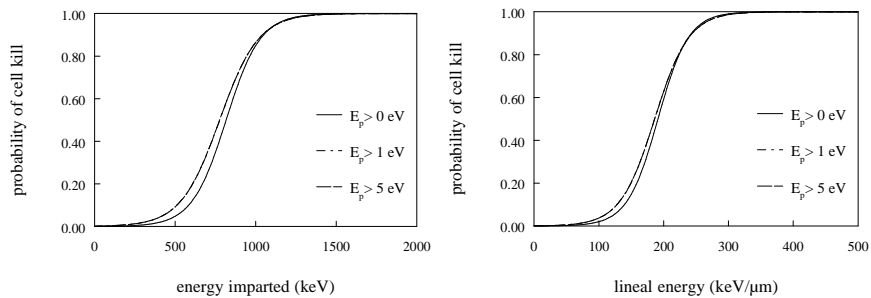


Figure 12.12: *Effectiveness function for single event model obtained by the least squares fit between measured and calculated surviving fractions using different thresholds for the proton recoil energy (curves for 1 and 5 eV can hardly be discriminated).*

The effectiveness function, as described in equation 11.11, is determined as a minimisation problem. This optimisation problem is mainly based on the integral over the distribution of energy deposition times the effectiveness function. In this experiment, the distributions of energy deposition for the different reactions cover different parts of the energy deposition range. In section 12.4, the means of the distributions are calculated (table 12.6). The boron reaction is mainly determined by high energy deposition. The mean energy imparted in the nucleus is 711 keV per event. For the nitrogen

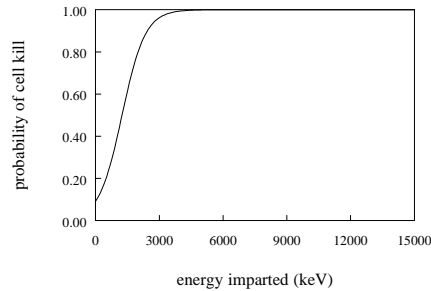


Figure 12.13: *Effectiveness function for the multiple event model obtained by the least squares fit between measured and calculated surviving fractions using a threshold of 1 eV for the proton recoil energy.*

reaction, the mean energy imparted in the nucleus is 171 keV, while the recoiling protons have a mean energy imparted between 2.30 and 19.9 keV (using a threshold of 1 eV). The constant a of the effectiveness function, indicating the energy deposition with an effect of cell kill of 50%, is mainly determined by the high energy depositions from the boron reaction. The slope of the function (indicated by the constant b of the effectiveness function) is determined by the large amount of low energy depositions from the proton recoil interactions. When other thresholds for the energy of the recoiling protons, only a minimal effect is obtained. The influence of the nitrogen on the effectiveness function is negligible.

12.6 Surviving fractions (D4)

Using the effectiveness function for the single event or multiple event model as calculated in section 12.5, the surviving fractions can be calculated. In this section, the surviving fractions measured after 30 minutes of irradiation are first recalculated for both models. These values are used for the optimisation and give no independent control over the functions. Therefore, four other situations are also considered: 0 and 15 ppm boron using one hour

irradiation time, and 30 and 45 ppm boron with an irradiation time of 15 minutes.

In figure 12.14, the results for both models using the energy imparted or lineal distributions are shown. The differences between the energy imparted distribution and the lineal distribution are large, but when weighted with the effectiveness function, almost the same surviving fractions are calculated. Also the results from the multiple event model are almost identical with the results from the single event model. Considering the uncertainties in the measurements and the uncertainties in the input parameters of the microdosimetry model (mainly the spectral characteristics and the concentration distribution of the boron and nitrogen atoms), the agreement between measurements and calculations is very good.

The contribution of the different reactions to the total surviving fraction for the irradiation position on the beam centre-line becomes visible in table 12.7. In case of a boron concentration of 15 ppm, most damage is

Table 12.7: Comparison of the effect of the different reactions on the surviving fractions, for the 5 irradiation positions on the central beam axis (Single event model using the energy imparted distribution and a threshold of 1 eV)

position	SF _{boron} ^a	SF _{nitrogen} ^b	SF _{recoil} ^c	SF _γ	SF _{tot}	SF _{meas}
1	0.35	1.00	0.72	0.80	0.20	0.22 ± 0.07
2	0.33	1.00	0.90	0.78	0.23	0.27 ± 0.06
3	0.51	1.00	0.97	0.80	0.40	0.46 ± 0.09
4	0.72	1.00	0.99	0.83	0.60	0.68 ± 0.13
5	0.87	1.00	1.00	0.86	0.74	0.77 ± 0.14

^a) 15 ppm homogeneously distributed

^b) 1.7 wt.% in the cell, 0.05 wt.% in the intercellular space

^c) 11 wt.% homogeneously distributed

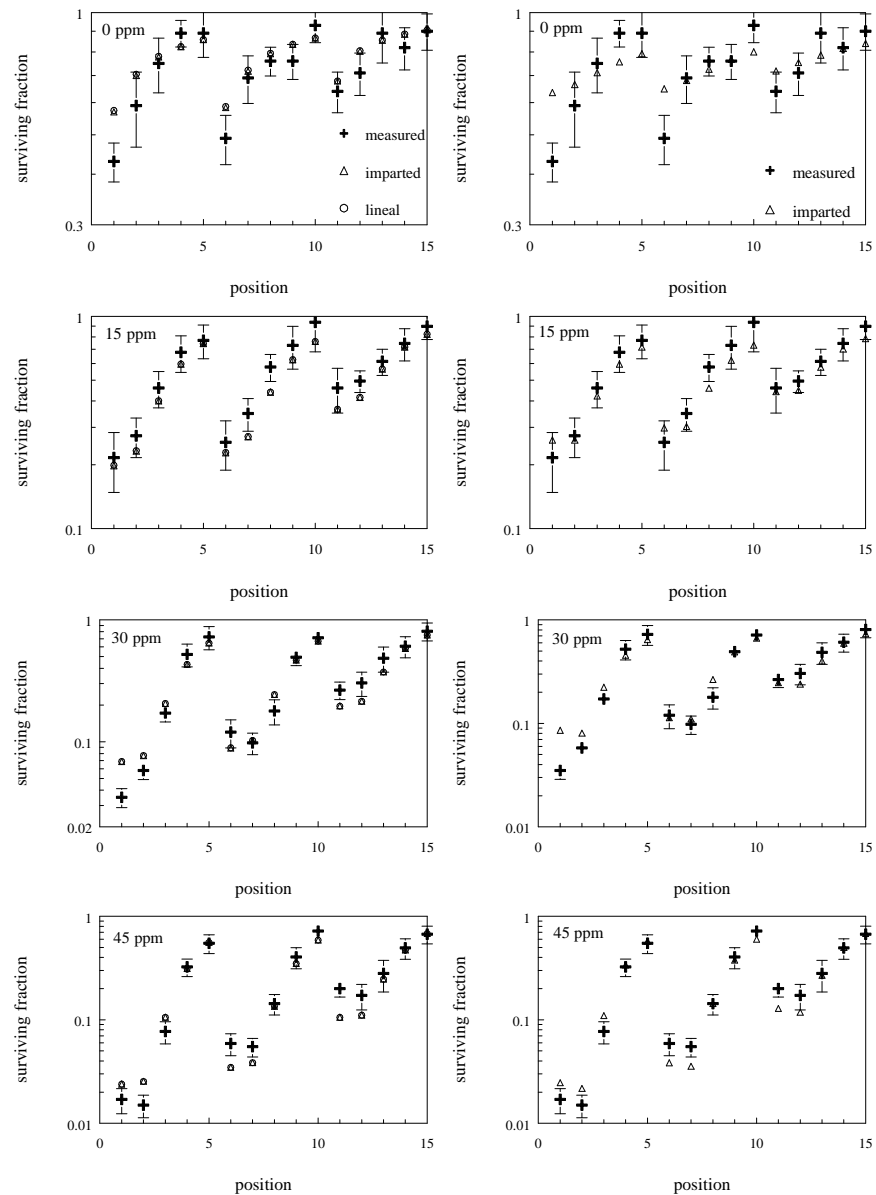


Figure 12.14: Comparisons between measured and calculated surviving fractions for different irradiation times and boron concentrations. Left the single event model and right the multiple event model (differences between energy imparted and lineal energy negligible).

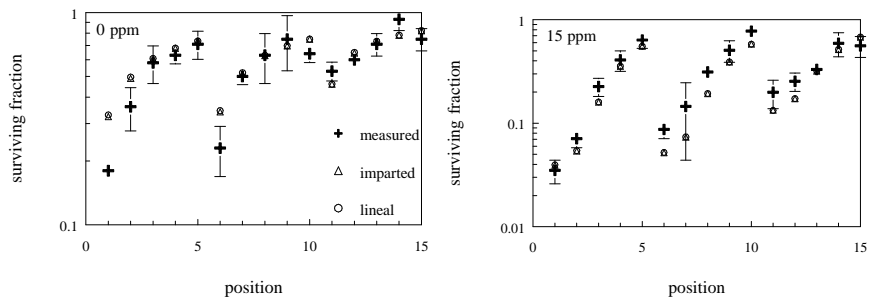


Figure 12.15: Comparisons between measured and calculated surviving fractions for different irradiation times and boron concentrations. The depicted fractions (0 and 15 ppm) were obtained after an irradiation of 60 minutes (single event model)

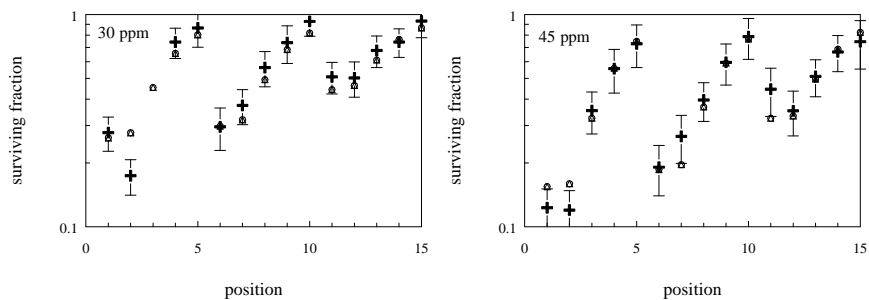


Figure 12.16: Comparisons between measured and calculated surviving fractions for different irradiation times and boron concentrations. The depicted fractions (30 and 45 ppm) were obtained after an irradiation of 15 minutes (single event model)

caused by the boron reaction. If no boron is present, the proton recoil reaction and the photons are the main contributors to the damage in the cell. The nitrogen reaction has hardly any effect in this experimental situation.

12.7 Calculations of the RBE values (D5)

12.7.1 Relative RBE values

In table 12.8, the RBE for the boron capture reaction is determined for two different boron distributions relative to the RBE of the homogeneous distribution. The energy imparted distribution gives a slightly different result than the lineal energy distribution. The trend is that if the atoms are located further away from the nucleus, the effect on the nucleus will decrease and so the RBE. The optimisation of the effectiveness function depends slightly on the chosen threshold for the recoiling protons.

In table 12.9, the influence of the intercellular concentration of nitrogen is considered, maintaining a concentration of 1.7 wt.% in the cell. By increasing the number of nitrogen atoms outside the cell, the effectiveness per reaction will decrease (as shown in table 12.6), and with a decreasing effectiveness also the RBE will decrease. The effect of the threshold influences the effectiveness function mainly for low energy depositions. The nitrogen reaction generates many energy depositions in the cell nucleus

Table 12.8: *Relative RBE values for different distributions of boron atoms (macroscopic concentration is 15 ppm)*

distribution	homog	int+cyto	int
energy imparted			
$E_p > 0$ eV	1	0.38	0.091
$E_p > 1$ eV	1	0.40	0.10
$E_p > 5$ eV	1	0.40	0.10
lineal energy			
$E_p > 0$ eV	1	0.45	0.10
$E_p > 1$ eV	1	0.47	0.12
$E_p > 5$ eV	1	0.47	0.12

with a low energy deposition, and is for that reason more independent of this threshold than the boron reaction.

Table 12.9: *Relative RBE values for different concentration of nitrogen atoms in the intercellular space (concentration in cell is 1.7 wt.%). Calculations are relative to the RBE of the boron reaction in case of a homogeneous distribution*

concentration intercellular space	0.025 wt.%	0.05 wt.%	0.075 wt.%	0.1 wt.%
energy imparted				
$E_p > 0$ eV	3.0	1.6	0.65	0.34
$E_p > 1$ eV	3.1	1.6	1.1	0.83
$E_p > 5$ eV	3.0	1.6	1.1	0.81
lineal energy				
$E_p > 0$ eV	1.9	0.97	0.40	0.21
$E_p > 1$ eV	1.7	0.88	0.60	0.46
$E_p > 5$ eV	1.7	0.90	0.61	0.47

In this experiment, the nitrogen concentration outside the cells is unknown. Using published RBE values for the V79 cells, this concentration can be predicted. In the literature, the proportion between the RBE of nitrogen and the RBE of boron (homogeneously distributed) is equal to 1.1 [Gabel, 1984]. Hence, the nitrogen concentration in the suspension during the irradiation must be approximately 0.075 wt.%, if a threshold for the proton recoil reaction is used, otherwise the concentration is lower, namely 0.06 wt.%.

The RBE for the proton recoil varies with the neutron energy, and therefore with the position in a phantom. In table 12.10, the RBE values relative to the RBE of a homogeneous distribution of boron atoms are given. The effect of the threshold for the energies of the recoiling protons is not negligible. However, the differences between 1 and 5 eV are within the uncertainties of the calculations. While the RBE increases with depth if no threshold is used, the RBE decreases in case of a threshold. Based on experimental

Table 12.10: *Relative calculated RBE values of the proton recoil for different positions in the phantom (concentration is 11 wt.%). Calculations are relative to the RBE of the boron reaction in case of a homogeneous distribution*

	pos. 1	pos. 2	pos. 3	pos. 4	pos. 5
energy imparted					
$E_p > 0$ eV	1.6	3.6	4.9	4.9	4.0
$E_p > 1$ eV	1.6	1.1	0.62	0.31	0.16
$E_p > 5$ eV	1.7	1.1	0.64	0.33	0.18
lineal energy					
$E_p > 0$ eV	1.5	3.5	4.7	4.7	3.8
$E_p > 1$ eV	1.5	1.1	0.67	0.33	0.17
$E_p > 5$ eV	1.7	1.3	0.74	0.37	0.19

knowledge [Alpen, 1992], the RBE in an epithermal beam decreases with depth. The two different distributions of energy deposition, the energy imparted and the lineal energy, give the same results. The high RBE for recoiling protons at the first irradiation position is a result of the very high number of tracks through the nucleus.

12.7.2 Absolute RBE values

The optimisation problem for the RBE for boron, results in a calculated RBE value between 2.2 and 2.3 for all distributions of energy depositions and all thresholds for the recoiling protons. Using the above relative relations between the different reactions, distributions or positions, the remaining RBE's can be calculated (see table 12.11). The nitrogen RBE is not calculated because of its unknown concentration in the intercellular space. The proton recoil RBE's change considerably using a threshold or not. The differences between a threshold of 1 or 5 eV are negligible.

Table 12.11: Calculated RBE values for the different reactions

threshold	literature	calculated					
		energy imparted			lineal energy		
		0 eV	1 eV	5 eV	0 eV	1 eV	5 eV
$^{10}\text{B}(n,\alpha)^7\text{Li}$	2.4	2.2	2.2	2.2	2.3	2.3	2.3
$^{14}\text{N}(n,p)^{14}\text{C}$	2.7	- ^a	-	-	-	-	-
proton recoil							
pos. 1	3.0	2.5	3.5	3.7	3.5	3.7	3.7
pos. 2	3.0	5.5	2.3	2.4	7.9	2.6	2.8
pos. 3	3.0	7.6	1.4	1.4	11	1.5	1.7
pos. 4	3.0	7.6	0.69	0.72	11	0.75	0.83
pos. 5	3.0	6.2	0.36	0.39	8.9	0.39	0.43

^a) not calculated because of uncertainties in nitrogen concentration in intercellular space

Chapter 13

Sensitivity analysis for the radiobiological experiment

13.1 Introduction

Some experimental parameters of the analysed radiobiological experiment have a large uncertainty, which can influence the results of the model considerably. In this chapter, the effect of these uncertainties is considered within a sensitivity study. This study is divided into three sections. In the first section, the influence of the input parameters of the Monte Carlo model is considered. The second and third ones deal with respectively the neutron beam characteristics; and the measured photon doses. In the last section, the effect of several assumptions on the effectiveness function is analysed.

The sensitivity analysis is performed using the Single Event model and the imparted energy distribution as an unperturbed situation. Protons with an energy lower than 1 eV are assumed to have no influence on the cells and are discarded.

13.2 Sensitivity analysis of the Monte Carlo calculations

The number of interactions simulated in the Monte Carlo program has influence on the statistical accuracy of the Monte Carlo calculations. A too little number of events causes large statistical uncertainties in the calculated results. In the analysis of the radiobiological experiment, described in chapter 12, 1,000,000 particles are simulated for the capture reactions and 100,000 for the proton recoil interactions within each energy group, leading to a total number of 4,700,000 simulated interactions. Calculations [Vroegindeweyj, 1994] have shown that for this experiment, the distributions of energy depositions converge within 5% after 100,000 interactions if the range of energy depositions is divided into 40 groups or less, while the other results have a statistical uncertainty smaller than 5% after 50,000 simulated interactions.

Some assumptions are made about the shape of the cell and the positions of the nucleus in the cell. Two different options for the position of the nucleus in the cell are possible in the model: the nucleus is fixed in the centre of the cell or the position of the nucleus is randomly distributed through the whole cell. If the atoms are randomly distributed, the positions of the nucleus have no effect on the results. A maximum effect is obtained if the atoms are only in the intercellular space. The maximum effect for the boron reaction is 25%. In the analysis performed in the previous chapter, a random distribution is considered.

The shape of the V79 cells in suspensions is assumed to be an ellipsoid with a maximum variation of 10% in the cell radii. The effect of this variation is small and can be neglected [Vroegindeweyj, 1994]. On the other hand if a completely different shape is used, the results can change considerably. The effect will be maximal for inhomogeneous atom distributions; using a homogeneous distribution, most of the effect disappears because a mean value over a large number of situations is considered.

The stopping power tables generated with TRIM are based on a stopping medium of water. The use of other materials (for example brain, blood

and muscle) lead to no significant changes in the results, because of the almost similar densities and composition. However, materials which are significantly different can have a large influence, but these materials are not relevant to BNCT.

13.3 Neutron energy spectrum

The calculations in the previous chapter are based on the presently best known neutron beam characteristics. As shown in the phantom calculations (chapter 6), the intensity of the fast neutron beam is most probably underestimated in the neutron beam spectrum derived from the MCNP calculations [Watkins, 1995]. In this section the influence of a changing spectrum is determined by repeating the calculations of chapter 12 with an adjusted spectrum. Based on the sensitivity study in chapter 6, the fast part of the spectrum (above the 1 MeV) is adjusted by a factor 5.4.

Changes in the spectrum will not affect the mean track length through the cell nucleus of the particles released by the capture reactions: an adjustment of the fast fluence rate influences the number of events negligibly, and consequently the effect on the number of particles going through the cell nucleus and the microscopic dose in the nucleus is negligible.

In contrast, the effect on the proton recoil reaction is large. In tables 13.1 and 13.2, the quantities for the unperturbed and the adjusted spectra are given for the proton recoil reaction. Using a higher intensity for the fast fluence rate, the mean penetration of the neutrons increases, leading to a higher number of recoiling protons at depth. Also, the mean track length of the protons in the nucleus and the microscopic dose in the nucleus increases.

Most of the energy deposition in the nucleus comes from the boron capture reaction. In this experiment, the influence from the proton recoil is secondary. Changing the intensity of the fast neutron fluence rate, the boron contribution does not change considerably, and therefore the change in the effectiveness function is small. In figure 13.1, the calculated effectiveness function is shown together with the unperturbed effectiveness function. The small changes in the effectiveness function also imply a small effect on the

Table 13.1: Mean track lengths [μm] in the nucleus, the frequency of hits [h^{-1}] and the microscopic dose rate in the nucleus [Gy/h] for the proton recoil reaction at different positions in the phantom

position	mean track length [μm]		tracks through the nucleus [h^{-1}]	
	unperturbed	adjusted	unperturbed	adjusted
1	0.058	0.093	383	385
2	0.072	0.16	118	121
3	0.13	0.39	28.5	31.0
4	0.31	0.97	6.71	8.62
5	0.74	1.91	1.79	3.17

Table 13.2: The microscopic dose rate in the nucleus [Gy/h] for the proton recoil reaction at different positions in the phantom

position	dose rate in the nucleus [Gy/h]	
	unperturbed	adjusted
1	0.611	0.866
2	0.234	0.432
3	0.0973	0.239
4	0.0464	0.146
5	0.0248	0.0937

calculated surviving fractions for the adjusted spectrum. The differences between the perturbed and unperturbed situation change are within 1%.

The RBE values (table 13.3) are calculated by the ratio between the number of tracks through the nucleus and the macroscopic dose multiplied by the integral of the effectiveness function folded with the distributions of

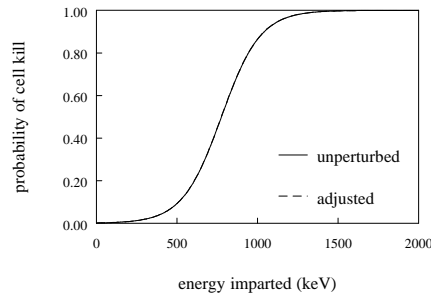


Figure 13.1: Effectiveness functions for a single event obtained by the least squares fit between measured and calculated surviving fractions based on different spectral characteristics (curves are on top of each other).

Table 13.3: RBE values^a for different spectral characteristics

interaction	unperturbed	adjusted
boron ^b	2.2	2.2
nitrogen ^c	3.5	3.5
proton recoil ^d		
pos. 1	3.5	3.4
pos. 2	2.3	1.4
pos. 3	1.4	0.67
pos. 4	0.69	0.33
pos. 5	0.36	0.22

^a) threshold for the proton energy is 1 eV

^b) boron concentration: 15 ppm homogeneously

^c) nitrogen concentration: 1.7 wt.% in the cell, 0.05wt.% in the intercellular space

^d) hydrogen concentration: 11 wt.% homogeneously

energy imparted (see equation 11.26). The effectiveness function does not change significantly for the high energy depositions if the neutron energy spectrum is adjusted. Consequently, the RBE for the boron and nitrogen

reaction barely changes. For low energy depositions in the cell nucleus, this change in the effectiveness function is larger, leading to a larger effect in the RBE for the proton recoil. A higher intensity of the fast neutrons causes a steeper decrease of the RBE with depth.

13.4 Influence of uncertainties in the photon dose

The data calculated with the Monte Carlo programs of blocks MC1 and MC2, as well as the normalisation in blocks D1 and D2, are independent of the photon dose, but changes in the photon dose influence the effectiveness function and the parameters calculated with this function. Two different uncertainties of the photon dose can be distinguished: uncertainties in the photon dose and uncertainties in the conversion of these doses into surviving fractions.

13.4.1 Uncertainties in the measured photon doses

The photon doses are measured in a cubic phantom on the beam centre-line. The obtained values are converted into dose rates in the Bremen phantom resulting in uncertainties up to 15%. To investigate the effect of these uncertainties on the effectiveness function, three different cases are considered. In the first case the effect of an overestimation of the dose rates is considered by decreasing the photon dose with 20% (indicated with $D_\gamma * 0.8$). In the second case an overestimation of the incident photon beam is considered by decreasing the photon dose rates for all positions with 0.2 Gy/h (indicated with $D_\gamma - 0.2$). In the third case, the relation between the dose rates on the beam centre-line and the other positions is considered by keeping the values on the beam centre line unchanged and decreasing the photon dose 2 cm from the centre beam line with 10% and 4 cm from the centre beam line with 20% (indicated with 100,90,80%).

The differences between the calculated effectiveness functions for different perturbations in the photon doses are small. As for the proton recoil contribution, the effect of the photons is secondary compared to the boron reaction. Consequently, the differences between the unperturbed and per-

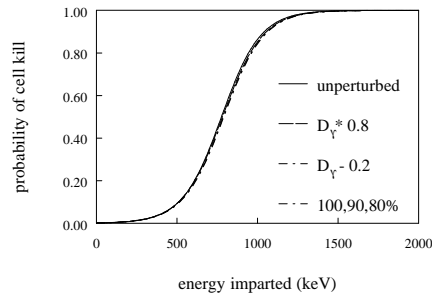


Figure 13.2: Effectiveness function for single event obtained by the least squares fit between measured and calculated surviving fractions, for perturbation in the photon dose.

Table 13.4: RBE values for different adjustments of the photon dose into the surviving fractions

interaction	unperturbed	$D\gamma * 80\%$	$D\gamma - 0.2$	100,90,80%
boron	2.2	2.3	2.3	2.2
nitrogen	3.5	3.7	3.7	3.6
proton recoil				
pos. 1	3.5	2.9	2.9	2.8
pos. 2	2.3	2.4	2.3	2.3
pos. 3	1.4	1.4	1.4	1.3
pos. 4	0.69	0.70	0.69	0.67
pos. 5	0.36	0.37	0.37	0.36

turbed calculated surviving fractions are small. The decrease of the photon dose is compensated by a higher contribution of the proton recoil reaction. For all positions the effect on the surviving fractions is smaller than 3%. The unperturbed and perturbed calculated RBE values are given in table 13.4.

The differences in the RBE's are negligible, except for the RBE for proton recoil at position 1, which decreases 20%.

13.4.2 Uncertainties in converting doses into surviving fractions

In chapter 12, a linear-quadratic model is used to calculate the surviving fractions from photons (equation 11.12), using the constants α and β derived from radiobiological experiments [Huiskamp, 1992]. The influence of uncertainties in the determination of the constants α and β is considered by decreasing these constants with 20%. Also a linear model is considered to convert the photon dose rates into surviving fractions:

$$SF_{\gamma} = e^{-D\gamma/D_0}, \quad (13.1)$$

where D_0 is experimentally determined by a standard photon experiment. In figure 13.3 the effectiveness functions for the perturbed situations are given. As the effectiveness function is mainly determined by the boron reaction, the changes in the effectiveness functions are small when the conversion of the photon dose into surviving fractions is perturbed. The perturbation in calculated surviving fractions is also small, the maximum change is 5%.

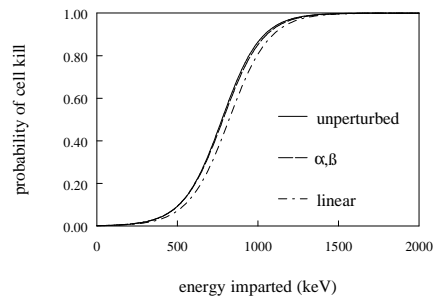


Figure 13.3: *Effectiveness function for the single event model obtained by the least squares fit between measured and calculated surviving fractions for different conversions of the photon dose to surviving fractions.*

The effectiveness function for high energy deposition hardly changes and consequently, the differences in the RBE values for the boron reactions

Table 13.5: RBE values for the proton recoil reaction for different conversions of the photon dose into the surviving fractions

interaction	unperturbed	α and β (-20%)	linear
boron	2.2	2.3	2.3
nitrogen	3.5	3.5	3.1
proton recoil			
pos. 1	3.5	1.8	2.4
pos. 2	2.3	1.5	2.0
pos. 3	1.4	0.85	1.1
pos. 4	0.69	0.43	0.58
pos. 5	0.36	0.23	0.31

are negligible. The effect on the RBE for proton recoil is significant. Changes in the conversion of photon dose lead to a different slope of the effectiveness function. The values of the effectiveness function for the low energy depositions change, and thereby the RBE for the proton recoil.

13.5 Determination of the effectiveness function

13.5.1 Other minimisation procedures

In chapter 12, the minimisation for the Single Event model is performed for differences between the measured and calculated logarithm of the surviving fractions (indicated with LN). The effect of choosing this optimisation problem is investigated by defining three other problems. In the first problem, the difference between the measured and calculated surviving fractions

(indicated with SF) is minimised:

$$\min_{a,b} \left| \sum_x \sum_C e^{-\int_z \{ \sum_r N_r(x,C) \cdot f_{1,r}(z,x,C) \} EF(z) dz} - SF(x,C)/SF_\gamma(x) \right|^2. \quad (13.2)$$

Instead of looking at absolute differences between measured and calculated surviving fractions, the relative differences can be considered (indicated with SF_{ref}, leading to a second minimisation problem:

$$\min_{a,b} \left| \sum_x \sum_C \frac{e^{-\int_z \{ \sum_r N_r(x,C) \cdot f_{1,r}(z,x,C) \} EF(z) dz} - SF(x,C)/SF_\gamma(x)}{SF(x,C)/SF_\gamma(x)} \right|^2. \quad (13.3)$$

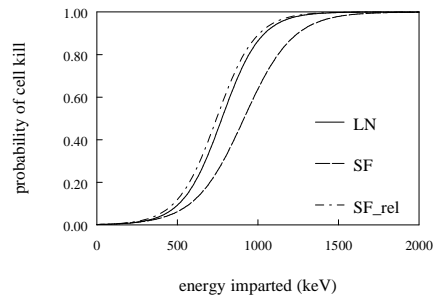


Figure 13.4: Effectiveness function for a single event obtained by the least squares fit between measured and calculated surviving fractions using different optimisation procedures.

The calculated effectiveness functions are drawn in figure 13.4. Different minimisation problems lead to different effectiveness functions, and based on this, to different calculated surviving fractions (figure 13.5) and RBE values (table 13.6). Again, the proton recoil dose is the most sensitive quantity. The differences in sensitivity are mainly caused by the fact that in the minimisation problems, the high energy depositions of the capture reaction have more influence than the low energy depositions of the recoiling protons in the cell nucleus.

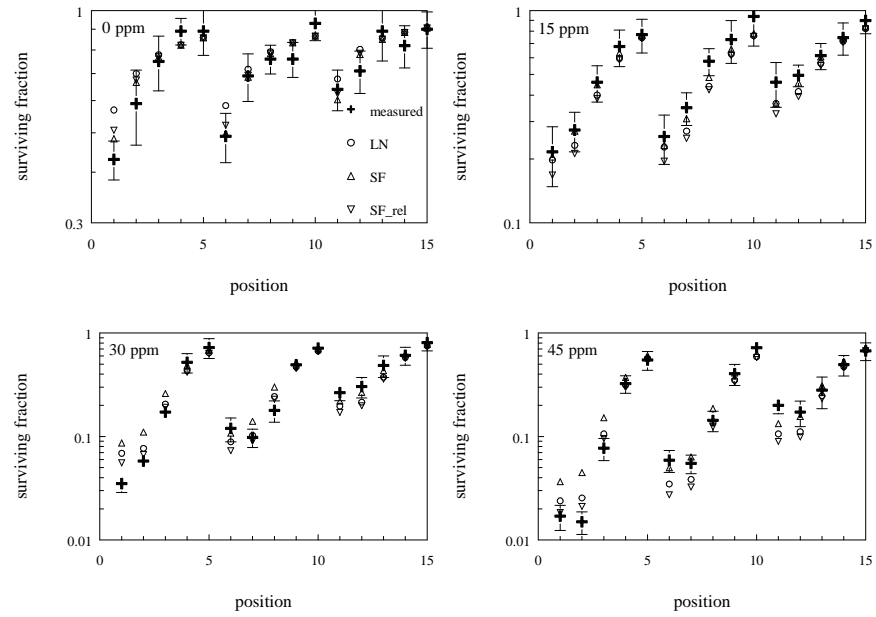


Figure 13.5: Calculated surviving fractions for different optimisation problems (single event model, irradiation time 30 minutes)

13.5.2 Weighting with uncertainties of measurements

Due to the experimental conditions, the uncertainties in the measurements change for different positions and boron concentrations. The influence of the uncertainties in the measurements is considered by dividing the difference between the calculated and measured logarithm of the surviving fraction by the uncertainties in the measurements, or the standard deviation σ :

$$\min_{a,b} \left| \sum_x \sum_C \frac{1}{\sigma^2} \left(\int_z \left\{ \sum_r N_r(x, C) \cdot f_{1,r}(z, x, C) \right\} \text{EF}(z) dz \right. \right. \\ \left. \left. + \ln(\text{SF}(x, C)) - \ln(\text{SF}_\gamma(x)) \right|^2. \quad (13.4)$$

The effect on the various calculated quantities is small, except for the RBE for the proton recoil reaction and the nitrogen capture reaction. The calculated effectiveness function is compared with the unperturbed effectiveness

Table 13.6: RBE values for the proton recoil reaction for different optimisation problems

position	logarithm of surviving fractions	absolute surviving fractions	relative surviving fractions
boron	2.2	2.1	2.2
nitrogen	3.5	4.0	4.4
proton recoil			
1	3.5	4.5	3.2
2	2.3	3.6	2.6
3	1.4	2.1	1.5
4	0.69	1.1	0.77
5	0.36	0.55	0.41

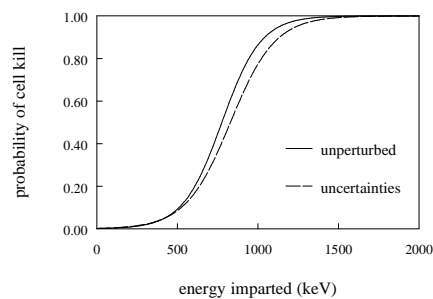


Figure 13.6: Effectiveness function for single event obtained by the least squares fit between measured and calculated surviving fractions.

function in figure 13.6. The surviving fraction changes only within 5% using the new calculated effectiveness function, and also the RBE for the boron reaction is not changed. The RBE for the recoiling protons and the protons from captures in nitrogen are increased.

Table 13.7: *RBE values in case of minimalistic problem weighted with the uncertainties in the measurements.*

interaction	unperturbed	uncertainties
boron	2.2	2.1
nitrogen	3.5	4.2
proton recoil		
pos. 1	3.5	4.1
pos. 2	2.3	3.3
pos. 3	1.4	1.95
pos. 4	0.69	0.96
pos. 5	0.36	0.51

13.5.3 Influence of the selection of a subset of concentrations or data points

In the optimisation of chapter 12, the data for all different boron concentrations and all different irradiation positions are for an irradiation time of 30 minutes. Looking only to a subset of these data, the effectiveness function can change. Instead of looking to all boron concentrations, only the data for no boron and 45 ppm boron are used in the optimisation. The irradiation positions are subdivided into three groups: position 1 to 5 (beam centre line), position 6 to 10 (2 cm from centre line) and position 11 to 15 (4 cm from centre line). The different effectiveness functions are given in figure 13.7.

The surviving fractions (figure 13.8) and the RBE for the boron capture reaction (table 13.7) are not sensitive to the choice of data. The RBE for the proton recoil is sensitive to the selection of a subset while the RBE for protons from captures in nitrogen does not exhibit any change.

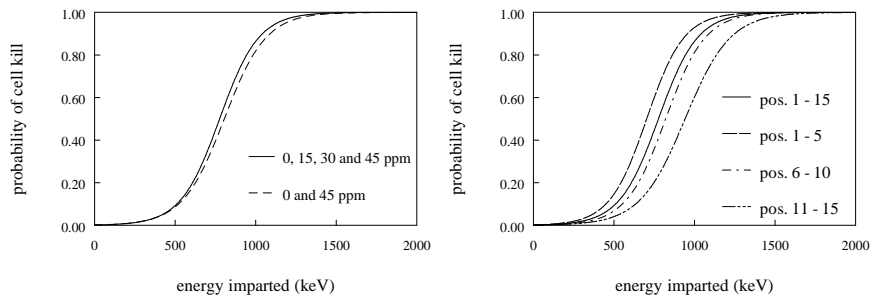


Figure 13.7: Effectiveness function for single event obtained by the least squares fit between measured and calculated surviving fractions using different subsets of data points.

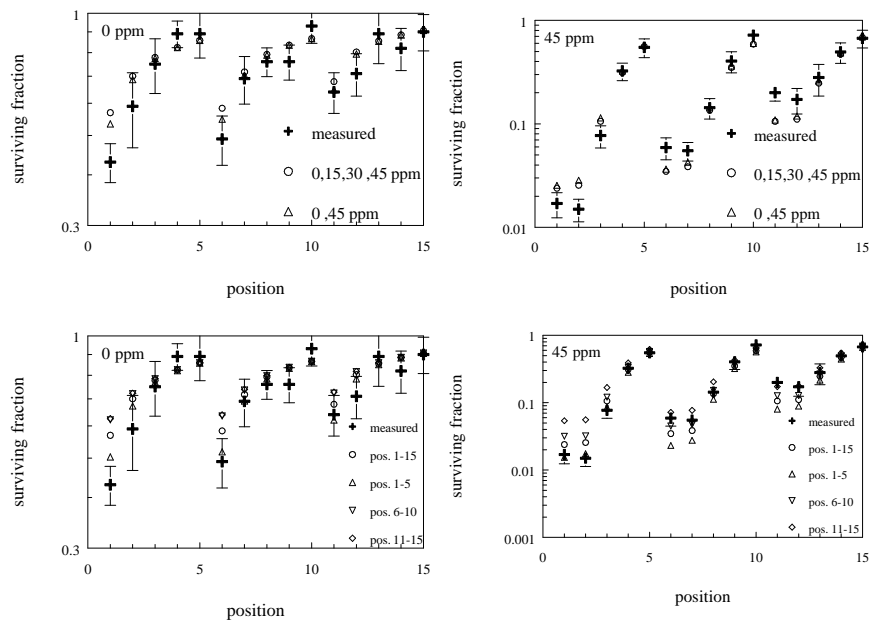


Figure 13.8: Calculated surviving fractions for different subsets of data points (single event model, irradiation time 30 minutes)

13.6 Conclusions

The calculated surviving fractions, effectiveness function and RBE for the boron reaction are not sensitive to small changes in the input parameters.

Table 13.8: RBE values for the proton recoil reaction for different subsets of data points

interaction	unperturbed	0 and 45 ppm
boron	2.2	2.1
nitrogen	3.5	3.7
proton recoil		
pos. 1	3.5	3.1
pos. 2	2.3	2.5
pos. 3	1.4	1.5
pos. 4	0.69	0.73
pos. 5	0.36	0.39

The large number of low-energy recoiling protons enlarges the small uncertainties in the effectiveness function for small energy depositions, resulting in a higher sensitivity in the RBE's for proton recoil for the input parameters. In all perturbed situations, a similar tendency is obtained concerning the RBE for proton recoil; the absolute values change considerably.

The results from the sensitivity analysis can be used to tailor new radiobiological experiments in such a way that the experiment will yield a maximum of information. A new set of experiments, especially performed to understand the effect of the RBE factors for low energy deposition, has to be designed. Using different incident neutron beams will give a better understanding of the behaviour of the recoiling protons. Three beams with different spectra are available in Petten for such a new experiment: the thermal facility and the 1 MeV fission neutron facility at the LFR and the epithermal facility at the HFR will give totally different spectra to test this postulate.

Table 13.9: *RBE values for the proton recoil reaction for different subsets of data points*

interaction	unperturbed	pos. 1-5	pos. 6-10	pos. 11-15
boron	2.2	2.3	2.1	2.1
nitrogen	3.5	4.9	2.6	2.3
proton recoil				
pos. 1	3.5	4.6	2.7	2.9
pos. 2	2.3	3.0	1.8	2.0
pos. 3	1.4	1.7	1.0	1.1
pos. 4	0.69	0.88	0.52	0.58
pos. 5	0.36	0.47	0.28	0.30

Chapter 14

Conclusions about the microdosimetry model

Microdosimetry is an important instrument to obtain a fundamental understanding of the principles of BNCT. To date, several microdosimetry models exist which can simulate the transport of particles released by the boron and nitrogen capture reaction. None of these models, however, can simulate the recoiling protons. A new microdosimetry model has been developed which can calculate all the important high-LET irradiation for BNCT, viz. particles from the boron and nitrogen capture reaction, as well as the proton recoil. Another disadvantage of the existing models is that little effort is put into the conversion from microdosimetric values to biological parameters such as surviving fractions or RBE factors. In the model developed here, a conversion to biological quantities has been made based on suggestions of the effectiveness function described by Gabel [Gabel, 1987] and Bond [Bond, 1985].

The different possibilities of the model may be explained by a large radiobiological experiment performed at the HB11 facility in Petten. At fifteen

different positions, vials with V79 cells containing different amounts of boron atoms were irradiated. The boron atoms given as boron acid, have been homogeneously distributed throughout the whole cell. The cells and nuclei are modelled as ellipsoids with a random variation of 10% in the radii. The consequence of this assumption is, in this case, small because of a homogeneous boron and hydrogen concentration. Only the nitrogen atoms are inhomogeneously distributed. The nitrogen concentration in the intercellular space is not known, but the energy deposition of this reaction is unimportant in this experiment. The V79 cells are grown on a medium containing a certain amount of nitrogen compounds. Before the cells were irradiated, they were washed to remove the growth medium. In theory, the nitrogen concentration in the intercellular space is equal to zero, but not in practice. If the published RBE values for the boron and nitrogen capture reaction for V79 cells is correct, the nitrogen concentration in the intercellular space can be predicted by the calculations. In this experiment a concentration of 0.02 wt.% in the intercellular space is found, which is 1% of the nitrogen concentration in the cell. In the analysis of the experiment a concentration of 0.05 wt.% is used. However, because of the small contribution to the total energy deposition of the nitrogen reaction, this overestimation of the concentration in the intercellular space is negligible.

The mean track lengths through the nucleus are comparable for the boron and nitrogen capture reactions. However, the energy deposition of the nitrogen reaction is significantly lower than for the boron reaction or the proton recoil, caused by a low number of tracks through the nucleus and a low stopping power. For the boron reaction, most of the energy deposition comes from particles starting in the cell nucleus itself. For the nitrogen reaction, the contribution from particles starting in the nucleus or in the cytoplasm is equal, the contribution of the intercellular space is in the case of a 0.05 wt.% concentration negligible.

Many neutrons interact with the hydrogen nuclei present in the cell suspensions. The major part of these recoiling protons have an energy and a track length that are so small that they have hardly any influence on the cells. The most important contribution comes from the few recoiling protons with a high energy, mostly originating outside the cell nucleus. The mean track

length through the cell nucleus and the mean energy imparted in the cell nucleus is strongly dependent on the position in the phantom.

If boron is present in the cell suspensions, most of the energy deposition comes from the boron reaction. Consequently, the number of tracks through the nucleus, the total track length in the nucleus and the energy deposition in the nucleus from the boron reaction, indicate the surviving fraction relative to a standard condition. The logarithm of the surviving fraction is almost proportional to these quantities. If no boron is present in the cell suspensions, the major part of the energy deposition comes from the photons and the recoiling protons. The influence of the nitrogen is negligible under this condition.

The effectiveness function, which allows the conversion of microscopic energy depositions to biological quantities, is determined by a minimisation problem defined by the square of the differences between the logarithm of the measured and calculated surviving fractions. In the analysed experiment, because most of the damage to the cells comes from the boron reaction and the energy deposited in the nucleus per boron event is large, the effectiveness function is well determined for large energy depositions. Smaller energy depositions are of minor importance and for that reason, the effectiveness function for small energy depositions is hard to determine. In the sensitivity studies, it is demonstrated that the effectiveness function is not sensitive to the large uncertainties in some of the input data. However, the small changes in the values of this function for low energy depositions can cause large effects in the proton recoil results due to the high number of interactions. For the single event model, the effectiveness function is calculated for the energy imparted distribution and for the lineal energy distributions. As the volume of the cell nucleus is rather constant, the distribution of the energy imparted and the specific energy are almost equal. In the case of the distribution of energy imparted, the multiple events model is also used. In the calculations of the effectiveness function, all fifteen irradiation positions and also all four boron concentrations are used, but only the data for an irradiation time of thirty minutes. The effectiveness function changes for every cell line. The obtained functions are only valid for the V79 cells.

The surviving fraction is calculated using the effectiveness functions. The main contribution to the cell kill comes from the boron reaction. The photon dose and the proton recoil cause significant damage to the cells while the nitrogen reaction hardly causes any damage in the cells. The differences in calculated cell surviving fractions using a single event model or a multiple events model are negligible. The same is true for the differences between the effectiveness function for the different distributions of energy deposition. The calculated values are compared with measured ones for three different irradiation times, including also a comparison with measurements that are not used in the optimisation problem when determining the effectiveness function. A good agreement exists between the measured and calculated values.

The calculated surviving fractions are not sensitive to most of the input parameters, such as the intensity of the fast neutron beam and the photon dose, since most of the effect is caused by the boron reactions with thermal neutrons. Choosing another optimisation problem or using only a subset of the data points can cause significant differences in the calculated effectiveness function. The latter points to inaccuracies in the input data. A better definition of the neutron beam and the photon dose can lead to a better agreement between the different subsets.

Another biological quantity calculated with the program is the RBE. The RBE for the boron capture reaction is not sensitive to the input parameters and is comparable with the measured value of 2.3. The RBE for the proton recoil reaction, however, is extremely sensitive to errors in the input parameters. Small uncertainties in the values of the effectiveness function for low energy depositions are strongly increased by the large number of interactions. Within this experiment, it is not possible to precisely calculate the RBE values for proton recoil. Use of a better defined neutron source to obtain the effectiveness function could solve this problem. Also an experiment with no boron additions and clearly distinguished spectra to avoid mathematical problems solving the minimisation problems, makes it possible to calculate the RBE for proton recoil.

A minimisation problem is described to calculate the boron concentration distribution based on measurements. Currently, no experimental data is available, hence the possibilities of this part of the model could not be demonstrated. Based on the nonsensitivity of the microscopic data to the boron reaction, this can be a valuable tool in the discussions about the boron distributions for the existing boron compounds BSH and BPA, or for new compounds that will be developed in the future.

The microdosimetry model is a useful tool to evaluate the effects of BNCT on a cellular scale [Vroegindewij, 1996]. Besides its use for BNCT, the model can also be used for the evaluation of other kinds of radiotherapy. For example, radionuclide labelled monoclonal antibodies, where energetic α -particles can be used to irradiate the malignant tissue. Until now the model is limited to the transport of heavy particles. The program can easily be extended to treat also the transport of β -particles in tissue.

References

- Ajzenberg-Selove, F. (1975), *Nuclear Physics*, A248.
- Alpen, E.L. (1992), 'Proton Induced Biological Damage Study', *Neutron Technology*.
- Amols, H.I., and Reinstein, L.E. (1992), 'Stochastic Considerations in BNCT; Microdosimetry and Cell Survival,' in *Proceedings International Workshop on Macro and Microdosimetry and Treatment Planning for Neutron Capture Therapy*, Cambridge, USA.
- Barth, R.F., Soloway, A.H., and Fairchild, R.G. (1990), 'Boron Neutron Capture Therapy of Cancer,' *Cancer Research*, Vol. 50, 1061-1070.
- Biavati, M.H., and Biavati, B.J. (1963), 'Computer Applications,' in *Annual Report of Research Project*, Report NYO-10451, Radiobiological Research Laboratory, Columbia University.
- Biersack, J.P., Ziegler, J.F., and Littmark, U. (1970), 'The stopping and Range of Ions in Solids,' Pergamon Press, New York.
- Bond, V.P., Varma, M.N., Sondhaus, C.A., and Feinendegen, L.E. (1985), 'An Alternative to Absorbed Dose, Quality and RBE at low exposure,' *Radiat. Res.*, Vol. 104, S52-S57.
- Charlton, D.E., and Sephton, R. (1991), 'A Relationship Between Microdosimetric Spectra and Cell Survival for High-LET Irradiation,' *Int. J. Radiat. Biol.*, Vol. 59, 447-457.
- Davis, M.A., and Little, J.B. (1970), 'Relative Biological Effectiveness of the $^{10}\text{B}(n,\alpha)^7\text{Li}$ Reaction in HeLa Cells,' *Radiat. Res.*, Vol. 43, 534-535.

- Fukuda, H., Kobayashi, T., Hiratsuka, J., Karashima, H., Honda, C., Yamamura, K., Ichihashi, M., Kanda, K., and Mishima, Y. (1987), 'RBE of a thermal neutron beam and the $^{10}\text{B}(n,\alpha)^7\text{Li}$ reaction on cultured B-16 melanoma Cells,' *International Journal of Radiation Biology*, Vol. 51, 161-175.
- Gabel, D., Fairchild, R.G., Larsson, B.S., and Borner, H.G. (1984), 'The Relative Biological Effectiveness in V79 Chinese hamster cells of the neutron capture reactions in boron and nitrogen,' *Radiat. Res.*, Vol. 98, 307-316.
- Gabel, D., Foster, S., and Fairchild, R.G. (1987), 'The Monte Carlo Simulation of the Biological Effect of the $^{10}\text{B}(n,\alpha)^7\text{Li}$ Reaction in Cells and Tissues and its Implication for Boron Neutron Capture Therapy,' *Radiat. Res.*, Vol. 111, 14-25.
- Hall, E.J., Novak, J.K., Kellerer, A.M., Rossi, H.H., Marino, S., and Goodman, L.J. (1975), 'RBE as a Function of Neutron Energy. Experimental Observations,' *Radiat. Res.*, Vol. 64, 245-255.
- Hartman, T., and Carlsson, J. (1994), 'Radiation dose heterogeneity in receptor and antigen mediated Boron Neutron Capture Therapy,' *Radioth. Onc.*, Vol. 31, 61-75.
- Hiratsuka, J., Fukuda, H., Kobayashi, T., Karashima, H., Yoshino, K., Imajo, Y., and Mishima, Y. (1991), 'The relative biological effectiveness of ^{10}B -neutron capture therapy for early skin reaction in the hamster,' *Radiat. Res.*, Vol. 128, 186-191.
- ICRU report No. 36 (1983), 'Microdosimetry,' ICRU, Bethesda.
- Huiskamp, R., Begg, A.C., Gregoire, V.G.A., Verrijck, R., Gabel, D., Siefert, A., and Moss, R.L. (1992), 'Radiobiology studies at Petten: Status on cell culture, mice and dog experiments,' in *Progress in Neutron Capture Therapy for Cancer*, Editors B.J. Allen *et al*, Plenum Press, New York.
- Huiskamp, R. (1995), private communication, Netherlands Energy Research Foundation (ECN), Petten, The Netherlands.
- Kellerer, A.M. (1970), 'Analysis of Patterns of Energy Deposition. A Survey of Theoretical Relations in Microdosimetry,' *Second Symposium on Microdosimetry*, Editor: H.G. Ebert, Report Vol. EUR 4453.
- Kitao, K. (1975), 'A Method for Calculating the Absorbed Dose near the Interface from the $^{10}\text{B}(n,\alpha)^7\text{Li}$ Reaction,' *Radiat. Res.*, Vol. 61, 304-315.
- Kobayashi, T., and Kanda, K. (1982), 'Analytical Calculation of Boron-10 Dosage in Cell Nucleus for the Boron Neutron Capture Reaction,' *Radiat. Res.*, Vol. 91, 77-94.

Moss, R.L. (1992), 'Current overview on the approach of clinical trials at Petten,' in *Boron Neutron Capture Therapy*, Editors: D. Gabel and R. Moss, 33-46, Plenum Press, New York.

The NAG Fortran Library Manual, Mark 16 (1993), Oxford, United Kingdom.

Northcliffe, L.C., and Schilling, R.F. (1970), 'Range and Stopping-Power Tables for Heavy Ions,' *Nuclear data tables*, Vol. A7, 233-463.

Raaijmakers, C.P.J. (1995), private communication, Dutch Cancer Institute, Amsterdam, the Netherlands.

Rassow, J., Pöller, F., Meissner, P. (1993), 'Physical and Tumour Biological Aspects and Calculation Model of Dosage in Boron Neutron Capture Therapy (BNCT),' *Stralenterapie und Onkologie*, Vol. 169, 7-17.

Rhoades, W.A., and Childs, R.L. (1986), 'An Undated Version of the DOT 4 one and two Dimensional Neutron/Photon Transport,' *Report: LA-7396-M, Revision 2.*, Los Alamos, September.

Roussin, R.W. (1980), 'BUGLE-80: coupled 47 neutron, 20 gamma ray, P3, cross section library for LWR shielding calculations,' *Oak ridge report DLC75*, Oak Ridge National Laboratory, June.

Slatkin, D.N. (1991), 'A History of Boron Neutron Capture Therapy of Brain Tumours,' *Brain*, Vol. 114, 1609-1629.

Solares, G.R., and Zamenhof, R.G. (1992), 'A New Approach to the Microdosimetry of Neutron Capture Therapy,' *Trans. Am. Nucl. Soc.*, Vol. 65, 153-155.

Varma, M.N., Bond, V.P., and Matthews, G. (1985), 'Hit-size Effectiveness Theory Applied to High Doses of Low LET Radiation for Pink Mutations,' in *Tradescantia. Radiation Protection Dosimetry*, Vol. 13, 307-309.

Verrijck, R., Huiskamp, R., Begg, A.C., Wheeler, F.J., and Watkins, P.R.D. (1994), 'A Comprehensive PC-Based Computer Model for Microdosimetry of BNCT,' *Int. J. of Radiat. Biol.*, Vol. 65, 241-253.

Vroegindewij, C. (1994) 'Micro Dosimetry Model. An extended version,' *ECN report: ECN-I-94-008*, Petten, the Netherlands.

Vroegindewij, C. (1996), Wheeler, F.J., Stecher-Rasmussen, F., Huiskamp, R., Gabel, D., 'Microdosimetry Model for BNCT Analysis,' in *7th Symposium on NCT*, Kobe, 1994, in press.

Vroegindewey, C. (1997), Wheeler, F.J., Stecher-Rasmussen, F., Huiskamp, R., 'A description of the proton recoil reaction by a microdosimetry model,' submitted.

Vroegindewey, C. (1997), Wheeler, F.J., Stecher-Rasmussen, F., Huiskamp, R., 'Estimation of the effectiveness function and surviving fractions using a microdosimetry model,' submitted.

Watkins, P.R.D. (1995), private communication, Joint Research Centre, Petten, The Netherlands.

Wheeler, F.J., Griebenow, M.L., Wessol, D.E., Nigg, D.W., and Anderl, R.A. (1990), 'A Stochastic Model for High-LET Response for Boron Neutron Capture Therapy (BNCT),' in *Clinical Aspects of Neutron Capture Therapy*, Editors: R.G. Fairchild, V.P. Bond and A.D. Woodhead, 165-178. Plenum Press, New York.

Wuu, C.S., Amols, H.I., Kiauga, P., Reinstein, L.E., and Saraf, S. (1992), 'Microdosimetry for Boron Neutron Capture Therapy,' *Radiat. Res.*, Vol. 130, 355-359.

Nomenclature

List of symbols

C_c	isotopic concentration in compartment c	ppm
D	dose	Gy
D_i	absorbed dose in compartment i	Gy
$D_{i,c}$	dose in compartment i per capture from particles originating in compartment c	Gy
E_n	neutron energy	eV
EF	effectiveness function	
EF _S	effectiveness function, single event model	
EF _M	effectiveness function, multiple events model	
EF _W	effectiveness function, weighted multiple events model	
$f(z)$	distribution of specific energy	
$f_1(z)$	distribution of specific energy, single event model	
$f_M(z)$	distribution of specific energy, multiple events model	
$f_W(z)$	distribution of specific energy, weighted multiple events model	
F_i	normalisation factor	
I_c	number of interactions in compartment c	
N_a	Avogadro's constant, $6.022 \cdot 10^{23} \text{ mol}^{-1}$	
N_i	number of particles reaching the cell nucleus	
$L_{i,c}$	mean track length in compartment i from particle out of compartment c	μm
M	molar weight of isotope	amu
P_i	poisson probability that i particles reach the cell nucleus	

$P_{i,c}$	probability that a particle from an event in compartment c will reach compartment i	
V_c	volume of compartment c	μm^3
SF	surviving fraction	
SF $_{\gamma}$	photon surviving fraction	
SF $_S$	surviving fraction, single event model	
SF $_M$	surviving fraction, multiple events model	
SF $_W$	surviving fraction, weighted multiple events model	
t	irradiation time	s
y	lineal energy	keV/ μm
z	specific energy	J/kg
α	constants to determine cell surviving fractions	Gy $^{-1}$
β	constants to determine cell surviving fractions	Gy $^{-2}$
ϵ	energy imparted	keV
ρ	density	g cm $^{-3}$
σ_g	absorption microscopic cross section for energy group g for the capture reactions or the scattering cross section for group g for the proton recoil reaction	barn
τ	scatter angle	
ϕ_g	fluence rate for energy group g	cm $^{-2}$ s $^{-1}$

List of abbreviations

BNCT	Boron Neutron Capture Therapy
DORT	two-Dimensional discrete ORdinates Transport code
HFR	High Flux Reactor
ICRU	International Commission on Radiation Units and measurements
KERMA	Kinetic Energy Released in MATter
LET	Lineal Energy Transfer
MCNP	Monte Carlo Neutron and Photon transport code system
RBE	Relative Biological Effectiveness
TRIM-88	TRansport In Matter version 1988

General conclusion and recommendations

In the present thesis, computer models are developed which simulate the history of neutrons along their entire path in the BNCT-chain from the creation of the first fission neutron in the nuclear fuel of a reactor core to the deposition of energy in the cell nuclei of malignant cells and healthy cells of a cancer patient. The purpose of this study is to create a system of models which can predict the biological effects of BNCT treatments by controlling the numerous parameters involved in this extensive chain.

The theoretical models consider different geometrical levels. Nevertheless, there is a strong correlation between the different parts. Part I, reactor calculations, deals with the transport of neutrons through the reactor from their origin to the point where they leave the reactor. The dimensions of the reactor and the beam channel geometry are the order of several metres. The phantom calculations, described in part II, start where the reactor calculations end. The neutron beam from the reactor forms the input for the transport calculations of the neutrons within a phantom. The neutron transport in this part is considered over several tens of centimetres. The microdosimetry model, as shown in part III, uses the neutron spectra calculated in Part II, as input to calculate the transport of heavy particles on a cellular scale. The dimensions of the considered cells are several tens of micrometres.

In all parts, a combination of two different calculation techniques is used,

namely the Monte Carlo techniques versus deterministic methods. The advantages of codes based on the Monte Carlo techniques are the easy implementation of difficult geometries or physical parameters. A disadvantage is the computation time that can be enormous, despite the large variety in available variance reduction techniques. Also the statistical uncertainties in the results make the code difficult to use for problems in which different situations are considered. The codes based on deterministic techniques can reduce the computation time considerably, but because of the inflexible way of representing the geometry or physical arguments gross assumptions are needed. To make optimal use of both techniques, a combination is used in all three parts of this thesis.

In chapter 2, a thermal facility is developed suitable for biological experiments. The materials and positions of the facility are chosen based on practical arguments. The facility is placed on the irradiation trolley of the LFR, to minimise the needed reconstruction work. The neutron spectrum at the beginning of the irradiation trolley has very high fast neutron and photon components. An additional moderator made of graphite blocks is placed on the trolley for further thermalisation of the neutron beam. After the graphite a boron coated lead shield is placed to reduce the photon component. Around the irradiation position the lead shield is replaced by a bismuth shield, having a smaller cross section for thermal neutrons. The dimensions of the moderator and the position of the bismuth window in the lead shield are the only unknowns in the calculations. After the construction of the facility, the calculations are compared with measurements. In this study, the Monte Carlo program MCNP is used. By fixing the number of materials, only a limited number of calculations has to be performed, making the needed computation time per calculation less important. The results are only calculated at the irradiation positions, allowing the use of variance reductions in the calculations. Finally, the entire reactor has been modelled in detail, enabling a comparison between measurements and calculations.

The calculations are compared with measurement using neutron activation detectors (foils). All calculated activations are slightly higher than the measured ones. The maximum difference between the calculations and

measurements is 25%, which is very reasonable for calculations of such dimensions. From this comparison, it can be deduced that the MCNP code can predict the neutron spectrum quite well. Only some preliminary photon measurements are performed indicating that the calculated and measured dose rates are of the same order. The facility is being used for different biological experiments and for calibration of neutron detectors since April 1994.

In the further development of the facility at the LFR, other materials and geometrical constructions must also be considered. The large number of different situations to be modelled, makes Monte Carlo calculations less appropriate, due to the long computation times. Deterministic codes, however, can be relatively easily be adapted to calculate effects of geometrical changes within a few minutes. In chapter 3, the Generalized Perturbation Theory is developed and implemented in the transport code DORT and the sensitivity uncertainty analysis code SUSU.

A clear difference in the use of Monte Carlo and deterministic techniques is also demonstrated for the phantom calculations as described in part II. Phantoms are often used to characterise neutron beams. Most phantoms have a simple geometry. The phantom used in part II is cylindrical, because of the simple geometry both calculational techniques represent the phantom very well. In the phantom, at fifteen different positions, the neutron spectra and the initiated photon dose are calculated. Due to the distribution of the positions at which the results are calculated, most of the variance reduction techniques in the Monte Carlo code cannot be used. The time needed to get reasonable results using the MCNP code is in the order of a week using a DEC-Alpha 3500 computer (150 MHz). The computation time needed by the deterministic code DORT depends strongly on the chosen cross section library. Due to the way DORT handles upscatter groups the calculation time increases exponentially with the number of upscatter groups. Small changes in the iteration algorithm of DORT can reduce this problem considerably. Using a library without upscatter groups, the needed computation time falls below 30 minutes.

As in part I, the calculations of part II are compared with measured quant-

ies. Based on this comparison, and earlier ones, conclusions can be drawn that the beam characterisation of HB11 is still inadequate. The intensity of the fast neutrons is underestimated in the (calculated) neutron beam compared with the measured data. Also the photon beam is not well characterised. At this moment only a limited amount of measured and calculated data about the photon beam is available. In order to make a good analysis of the experiments possible, a better characterisation of the beam is needed.

In the microdosimetry model, as described in part III, the Monte Carlo calculations are tied in with the deterministic techniques. The transport of the particles on a cellular scale is performed using Monte Carlo techniques. In contrast to the deterministic techniques, the Monte Carlo technique makes it possible to easily implement different cell geometries (diameters and positions), origins of interactions or directions and track length of the particles. A disadvantage is the large computation time needed for the Monte Carlo calculations. Much effort has been put into the reduction of the computation time using biased Monte Carlo techniques. Also the normalisation of the calculations takes place outside the Monte Carlo program, making quick comparison of different neutron spectra or boron concentrations possible. Except for the transport calculations, all programs within the microdosimetry model are based on deterministic calculations.

Only a small part of the results of the microdosimetry model can be compared with measurements or literature. The data from the Monte Carlo program and the first three deterministic blocks of the model can only be validated indirectly. The calculated surviving fractions are directly compared with measurements. Because not all measured surviving fractions are used in the calculation of the effectiveness function, these data points can be used to get an independent validation of the effectiveness function. The agreement between measured and calculated surviving fractions is good (within the statistical uncertainties of the measurements). Also the calculated RBE values are compared with values from the literature. For the boron reaction a calculated value of 2.2 is found while the literature gives a value of 2.3. The proton recoil RBE is more difficult to compare because normally the RBE for proton recoil is considered constant. In reality this RBE varies with the neutron energy. The effect of a constant RBE leads

to an overestimation of the proton recoil contribution at depth. However, in case of BNCT the assumption of a constant RBE has only a small effect on the results in cells where boron atoms are present, due to the fact that already with small concentrations of boron (from around 5 ppm), this reaction is the major contribution to the cell damage. For clinical applications, this means that the effect in healthy tissue, situated deeply in the head, will be overestimated. If a neutron beam with a higher fast neutron intensity is used, for example in fast neutron therapy, is used the effect of a constant RBE for proton recoil is much larger.

For the further development of the microdosimetry model, new radiobiological experiments must be performed. The uncertainties in the data of the proton recoil reaction can be solved by using different neutron beams. In Petten, a unique combination of a thermal and fast (1 MeV) facility at the LFR and an epithermal facility at the HFR are available, which forms an excellent possibility for further development of the model. Also the boron concentration distributions can be investigated on a cellular scale using microdosimetry. For this purpose experiments with different boron compounds must be performed. The microdosimetry model is intensely used to analyse cell suspensions, but only preliminary calculations have been performed with the tissue and capillary models. After upgrading and testing the programs for these models, the model can be used to predict the effect of BNCT during clinical irradiations. Finally, the model consists of a large amount of small programs. To make these programs useful to others, an interface around the program must be constructed. A direct coupling between the microdosimetry model and the treatment planning software is recommended if the effect of BNCT in clinical situations is considered.

Summary

Theoretical models have been developed on three different levels: the development and design of a thermal facility, characterisation of the neutron and photon beam in a phantom, and the development of a microdosimetry model to analyse the effects of BNCT on a cellular scale.

Part 1: Reactor Calculations

In chapter 2, a design study of the thermal facility is performed, resulting in the construction of the thermal facility at the Low Flux Reactor (LFR) in Petten. After the construction of the facility, neutron activation detectors (foils) were used to validate the calculations. This comparison shows a good agreement, between calculated and measured results. The difference between calculations and measurements are within 25%, which is very acceptable, keeping in mind the uncertainties in the cross sections, the assumptions made in the geometry of the reactor and the complication of the power calibration at (low) reactor power. After the realisation of the facility, it has been regularly used for different radiobiological experiments and for the characterisation of ionisation chambers.

For further development of the thermal facility at the LFR, more calculations will be needed. To reduce the computer time, a technique called Generalised Perturbation Theory has been developed in chapter 3. This technique is implemented in the transport code DORT and in the sensitivity code SUSD. Effects of changes in the geometry or materials can now be analysed within minutes, reducing the computer time considerably.

Part II: Phantom calculations

Calculations have been performed to determine the neutron spectra and photon dose at different irradiation positions. These calculations are based on an earlier calculated characterisation of the HB11 beam by Watkins. The calculations are compared with two different types of measurements: activation foils and ionisation chambers. The calculated and measured activations are in good agreement (within 10%). The incident photon dose rates cannot be calculated because currently no characterisation of the photon component in the beam is available. The assumption of an incident dose rate of 1 Gy/h is very reasonable. Using this assumption the maximum differences between the (total) measured and calculated photon dose rate is 16%. The calculated proton recoil dose rates are much lower than the measured dose rates caused by an underestimation of the fast neutron intensity in the beam characterisation. A sensitivity study shows that an increase of the fast neutron intensity, especially above 1 MeV, would lead to a much better agreement between measurements and calculations. In relative calculations uncertainties in the beam anisotropy have negligible influence on the calculated spectra at depth.

Part III: Microdosimetry model

A tool has been designed to obtain a better understanding of the effects of BNCT on a cellular scale. This tool, a microdosimetry model, has been developed to include all reactions important for BNCT. The model is capable of calculating a large variety of quantities. Most important are the effectiveness function, the surviving fractions, RBE values and boron concentration distributions. In chapter 12, the model has been used to analyse an extensive set of biological experiments performed at the HB11 beam. A very good agreement exists between the measured and calculated surviving fractions (within the uncertainties of the measurements). The influence of several input parameters on the results of the microdosimetry model is considered in chapter 13. The surviving fractions are mainly determined by the boron capture reaction. Therefore the calculated surviving fractions are insensitive to the input parameters, apart from the boron concentration distribution. On the other hand, the calculated quantities for the proton

recoil reaction are sensitive to many input parameters. To calculate these quantities a new experiment must be performed in which the boron reaction is less dominant.

Corine Vroegindeweyj

Samenvatting

Boron Neutron Capture Therapy

"Boron Neutron Capture Therapy"(BNCT) is een kankertherapie die in ontwikkeling is. Deze therapie brengt twee componenten die elk slechts geringe schade aanbrengen aan het weefsel. De eerste component is een stabiel borium isotoop (^{10}B). Door middel van een daarvoor geschikte bori-umdrager worden de borium-atomen geconcentreerd in de tumorcellen. De tweede component bestaat uit thermische neutronen: dit zijn neutronen met een lage energie. BNCT is gebaseerd op de nucleaire reactie tussen beide componenten. Een borium-atoom vangt een neutron in, en vormt aldus een aangeslagen ^{11}B atoom. Dit atoom vervalt naar zijn grondtoestand van een ^7Li atoom onder uitzending van een α -deeltje. De totale energie die hierbij vrijkomt is 2.79 MeV. Deze α -deeltjes en Li-atomen hebben een weglengte die ongeveer gelijk is aan de diameter van een cel. Omdat deze weglengte zo klein is wordt er alleen schade aangebracht in de cellen waar het borium zich bevindt.

Naarmate men dieper in het weefsel komt neemt het aantal thermische neutronen snel af. Daarom is het moeilijk om voldoende neutronen in dieper gelegen tumoren te brengen. Om dit probleem te verhelpen worden epithermische neutronen gebruikt: dit zijn neutronen met een hogere energie dan thermische neutronen. Deze epithermische neutronen verliezen hun energie door botsingen met het weefsel, waardoor in de tumoren toch voldoende thermische neutronen aankomen. Tot nu toe kunnen adequate neutronenbundels alleen worden gerealiseerd door onderzoeksreactoren.

In 1987 is het Energieonderzoek Centrum Nederland (ECN) in een Europees samenwerkingsverband begonnen met het bestuderen van de mogelijkheden om patiënten met een hersentumor te bestralen bij de Hoge Flux Reactor (HFR) in Petten. Als ondersteuning van dit project, worden er verschillende onderzoeken verricht om de therapie beter te begrijpen en die verder te ontwikkelen.

Dit proefschrift beschrijft theoretische modellen op drie verschillende gebieden:

- de ontwikkeling en het ontwerp van een thermische faciliteit,
- de karakterisering van de neutronen- en fotonenbundel in een fantoom,
- de ontwikkeling van een microdosimetrie-model om de effecten van BNCT op cellulaire schaal te analyseren.

De ontwikkeling van de thermisch faciliteit

Een belangrijke manier om meer inzicht in BNCT te krijgen is door radiobiologisch onderzoek. Een groot deel van dit onderzoek wordt uitgevoerd met thermische neutronen. Voordat aan dit promotieonderzoek werd begonnen waren er alleen thermische bundels voor radiobiologisch onderzoek beschikbaar in de VS, Japan en Zweden. Besloten werd om een nieuwe thermische bundel te ontwikkelen in Petten. In hoofdstuk 2 van dit proefschrift is de ontwikkeling van een thermische faciliteit bij de tweede onderzoeksreactor in Petten, de Lage Flux Reactor (LFR), ontwikkeld hetgeen een waardevolle aanvulling is op de reeds bestaande (klinische) epithermische bundel bij de HFR.

Voor de verdere ontwikkelingen van de thermische faciliteit zullen vele berekeningen moeten worden uitgevoerd. Als de berekeningen worden uitgevoerd op een zelfde manier als in hoofdstuk 2 van dit proefschrift, ligt de rekentijd per berekening in de orde van enkele dagen. Om deze rekentijd te verminderen is een methode ontwikkeld en hoofdstuk 3 van dit proefschrift beschreven waarmee het effect van veranderingen in de constructie van de reactor of de keuze van materialen binnen enkele minuten kan worden verkregen. Deze techniek is geïmplementeerd in twee reeds bestaande computer programma's.

Fantoom berekeningen

Naast deze experimenten bij de thermische bundel is er ook radiobiologisch onderzoek verricht bij de epithermische bundel in de HFR. In een cilindrisch fantoom, een perspex omhulsel gevuld met water, kunnen op verschillende plaatsen biologische objecten geplaatst worden. Door dit fantoom in de epithermische bundel te plaatsen kan het effect van een bundel op diverse posities worden bestudeerd. Om het effect op deze biologische objecten goed te kunnen analyseren is de concentratie van de neutronen en hun energie op de bestralingsposities uitgerekend. Deze berekeningen zijn uitgevoerd in deel II van dit proefschrift. In dit deel is alleen het fantoom gemodelleerd. De beschrijving van de eigenschappen van de epithermische bundel gebeurt aan de hand van model gemaakt door anderen. Door de complexiteit van dit model zijn er enkele onzekerheden in de eigenschappen van de bundel. De effecten van deze onzekerheden worden bestudeerd in een gevoeligheidsanalyse: een studie waarin het effect van veranderingen van een bepaalde invoerparameter op de resultaten wordt bestudeerd.

Microdosimetrie model

De boriumatomen verdelen zich niet homogeen in het weefsel. Omdat de deeltjes die vrijkomen bij de boriumreactie een korte dracht hebben, heeft de inhomogene verdeling van de atomen een grote invloed op het effect van de therapie. Een wiskundige aanpak is de enige manier om het complexe geheel van reacties in BNCT te kunnen ontrafelen. Tot nu toe bestaan er alleen programma's die een gedeelte van de effecten die voorkomen bij de BNCT behandeling kunnen beschrijven. Een nieuw model is ontwikkeld waarin alle voor BNCT belangrijke effecten zijn gemodelleerd. In deel III van dit proefschrift wordt dit model beschreven. Het model is gebruikt om een radiobiologisch experiment, uitgevoerd bij de epithermische bundel van de HFR, te analyseren. Ook hierbij is een gevoeligheidsanalyse uitgevoerd.

Corine Vroegindeweyj

Acknowledgement

The work presented in this thesis would not have been possible without the fruitful contribution of many people.

Finn Stecher-Rasmussen introduced me into the field of BNCT and supported me throughout the whole project. The Netherlands Energy Research Foundation, ECN, in Petten offered me the opportunity to perform this work. During this period many others at ECN contributed to this thesis. Adri Paardekooper and Willem Voorbraak have performed the foil measurements at the LFR and the HFR (chapters 2 and 6). Willem Voorbraak, Willi Freudenreich and Han de Haas have stimulated the research by their interest and comments. The members of the Reactor physics group, especially Alfred Hogenbirk, have supported me with the use of the transport codes. René Huiskamp, Helene Phillippo and the rest of the Department of Radiobiology helped me with their criticism, the explanation of biological phenomena and by performing the cell experiments at the HFR (chapter 12). Arie Lamerée and the rest of the LFR crew provided their support generously. Gerard van Nes, Marcel Bernards and many others from the unit Facilities solved many computer related problems. Henk Klippel has read the manuscript. And at least as important, I thank all colleagues of the Fermi building, for the pleasant atmosphere they have created during these years and in particular Dik Ketema, who has been a very pleasant office mate during these years.

A number of people outside ECN have also collaborated on this work. Prof. Hermans, Prof. van Dam and Prof. Gabel are gratefully acknowledged for many interesting discussions. Floyd Wheeler has been a con-

tinuous inspiration and a reliable beacon in every matter concerning BNCT. Ray Moss used his long BNCT experience to make many valuable suggestions concerning the proper use of the English language. Niels Raaijmakers and Eric Nottelman performed the measurements with the ionisation chambers (chapter 6).

I am very grateful to ECN for the possibilities they offered me to visit BNCT-colleagues at other institutes. I would like to thank all people who were involved in this. I am extremely obliged to Ginny and Floyd Wheeler, with whom I stayed during the weeks I worked at INEL; to Floyd Wheeler and Dave Nigg for their time and interest during my stay in Idaho; to Robert Zamenhof, Guido Solares and all the others who showed me the progress of the BNCT project in Boston; to Jeffrey Coderre, Jacek Capala and the rest of the team in Brookhaven for sharing their experiences with me during one of the first patient treatments in the USA; and finally, the group in Essen for teaching me more about conventional ways of cancer treatment.

And last, but not least, to Frank, thanks for your never ending patience and support.

Curriculum Vitae

Corine Vroegindeweyj was born on October 6, 1969, in Heukelum, The Netherlands. When she finished high-school (Gymnasium) in 1987, she went to Delft to study technical mathematics at the Delft University of Technology, where she graduated in April 1992. Her graduation work was performed at the Energy Research Foundation (ECN) in Petten, The Netherlands. After a temporary post of several months, she started in January 1993 with her Ph.D.-research also at ECN resulting in this thesis. In 1997, she began her present employment at the Joint Research Centre (JRC) of the European Commission in Petten, where she is involved in BNCT treatment planning.